Multi-component surface-wave analysis for tunnel detection in the Sonoran Desert, AZ

By

Sarah Laura Catherine Morton Rupert

B.S., University of Connecticut, 2011
M.S., University of Connecticut, 2014
Ph.D., University of Kansas, 2021

Submitted to the graduate degree program in the Department of Geology and the Graduate Faculty of the University of Kansas in partial fulfillment of the requirements for the degree of Master of Science.

_____

Chairperson: Dr. George Tsoflias

_____

Dr. Robert L. Parsons

_____

Dr. Jennifer Roberts

Date Defended: February 1, 2022

The thesis committee for Sarah Laura Catherine Morton Rupert
certifies that this is the approved version of the following thesis:

Multi-component surface-wave analysis for tunnel detection in the Sonoran Desert, AZ

_____

Chairperson: Dr. George Tsoflias

Date Approved: February 1, 2022

Abstract

Subsurface void detection using seismic imaging is a challenging task that has been the subject of extensive research. In this thesis, I employ the novel multi-component backscatter analysis surface waves (BASW) methodology to detect a tunnel 1 m diameter and 10 m deep in the Sonoran Desert, AZ. Vertical (V, Rayleigh wave), longitudinal (H1, Rayleigh wave), and transverse (H2, Love wave) surface-wave components were acquired and processed using multichannel analysis of surface waves (MASW) as input for backscatter analysis. BASW sections from all three data sets provided evidence of the tunnel and represented the first successful three-component BASW analysis. Backscatter from the tunnel was significantly enhanced while scatters from geologic heterogeneities were reduced by multiplying the H1 and H2 BASW sections. The location of the tunnel was identified with high confidence based on a joint interpretation of these different work flows. With the clarity of the tunnel signature observed on the multiplied H1-H2 BASW section and verification of that interpretation from numerical modeling, future tunnel detection studies using surface-wave methods would benefit from the combined use of the horizontal components. Joint interpretation of multiple results indicated that perturbations in the surface-wave wavefield can be indicative of a 1 m diameter and 10 m deep tunnel.

Acknowledgments

This thesis project would have not been possible without the technical and financial support provided by Dr. Rick Miller of the Kansas Geological Survey at the University of Kansas. I also thank Dr. Steve Sloan and the U.S. Army Corps of Engineers, Engineering Research and Development Center for sponsoring this research project, which was part of a larger field investigation conducted at the Yuma Proving Ground in 2016.

Additional guidance with survey design, data processing, and analysis were provided by Dr. Julian Ivanov and Shelby Peterie. I am also grateful to my M.S. committee members, Dr. Georgios Tsoflias, Dr. Robert Parsons, and Dr. Jennifer Roberts for agreeing to serve on my committee, support my work, and swiftly helped me reach the finish line.

I would be remiss to not thank Brett Wedel, Brett Bennett, Joe Anderson, and Jeremy Scobee who are largely responsible for data acquisition and re-acquisition of the data required for this project that became this M.S. thesis.

Table of Contents

List of Figures

List of Tables

Chapter 1: Introduction

Tunnel detection and imaging has been a challenging area of research in near-surface geophysics and engineering communities for more than fifty years (Greenfield et al., 1976; Belesky and Hardy, 1986; Grandjean and Leparoux, 2004; Gelis et al., 2005; Sloan et al., 2015). Several non-invasive geophysical methods have been applied to this problem including ground penetrating radar (Al-Shayea et al., 1994; Chen and Scullion, 2008), electrical resistivity (Sastry, 2014), seismic body-wave (Sloan et al., 2015; Lellouch and Reshef, 2017; Peterie et al., 2020), and seismic surface-wave techniques (Phillips et al., 2000; Sloan et al., 2010; Sloan et al., 2013; Schwenk et al., 2016; Ivanov et al., 2017). Most of these investigations conclude that complex near-surface geologic environments and void structures prevent the development of a simple and rapid method for obtaining a clear tunnel signature. Geologic complexities, such as unconsolidated soils with lithologic variability, fractures, or boulders, can appear as anomalies with characteristics consistent with subsurface voids and inhibit unique interpretation of tunnels. For the purpose of clandestine tunnel detection, it is imperative that geologic heterogeneities and man-made features be discernable from tunnels.

Complexities, such as unconsolidated soils with abrupt lithologic changes, fractures, or boulders are naturally occurring geologic heterogeneities and can present as seismic velocity variations or signal disruptions with seismic signal characteristics consistent with anthropogenic anomalies; this can subsequently inhibit the unique interpretation of tunnels (Moran and Greenfield, 1993; Grandjean and Leparoux, 2004). Signal-to-noise ratio (SNR) of a data set can also contribute to the misidentification of a tunnel signature because these geologic complexities may exhibit a SNR higher than the tunnel making the tunnel more difficult to distinguish from

the natural environment (Sloan et al., 2010). When the seismic signature of the target of interest (i.e., the tunnel) has relatively low SNR, it is challenging to distinguish the target from the background material (i.e., natural geologic environment). The amplitude of these seismic signals also deteriorates as the diameter of the tunnel decreases and with increasing depth (Zeng et al., 2009; Sloan, 2015), which further decreases the detectability of the tunnel. For the purpose of tunnel detection, it is imperative that geologic heterogeneities and other man-made features be discernable from tunnels.

Some seismic methods have proven successful imaging voids as small as 1-2 meters in diameter either directly or indirectly (Nasseri-Moghaddam et al., 2005; Sloan et al., 2015; Schwenk et al., 2016). Disturbances or changes in the material surrounding the void rather than the cavity itself are the indirect signatures observed most often (Belesky and Hardy, 1986; Ivanov et al., 2013). Proven and reliable non-invasive seismic methods for capturing tunnel signatures primarily include diffraction imaging (Belfer et al., 1998; Xia et al., 2007; Shao et al., 2016; Peterie et al., 2020), backscatter analysis of surface waves (BASW) (Ivanov et al., 2003; Sloan et al., 2010; Sloan et al., 2015; Schwenk et al., 2016; Sherman et al., 2018), surface-wave attenuation (Nasseri-Moghaddam et al., 2005; Putnam et al., 2008; Buckley and Lane, 2012), and refraction tomography (Turpening, 1976; Hickey et al., 2009; Riddle et al. 2010). Seismic methods have been favorable for most applications because data acquisition can be performed over large volumes with minimal ground footprint (Steeples, 2001). This concept has been enhanced with the development of towed arrays and land streamer technology which allow seismic surveys to be performed rapidly and continuously (Miller et al., 2003; Inazaki et al., 2005; Sloan et al., 2011; Buckley and Lane, 2012; Schwenk et al., 2016) while maintaining data quality consistent with fixed array methods (Suarez and Stewart, 2008).

The conventional multichannel analysis of surface waves (MASW) method has been successfully used for void detection (Sloan et al., 2013); however, anomalous features turn out to be geologic more often than clandestine, which has led to greater uncertainty with this method. Surface waves are sensitive to subtle changes in dynamic small-strain material properties, but long wavelengths and large sampling volumes smear the resulting 2D shear-wave velocity (Vs) sections and restrict lateral resolution (Zhang et al., 2004; Xia et al., 2004; Ivanov et al., 2006; Mi et al., 2017). This inherent limitation of surface waves has generally restricted applications of the MASW method to larger-scale (i.e., several tens of meters) void detection investigations, such as those resulting from salt dissolution (Sloan et al., 2009; Ivanov et al., 2013; Morton et al., 2020) or other abandoned, underground mines (Billington et al., 2006; Xu and Butt, 2006; Ivanov et al., 2016; Crook et al., 2017). Variations in shear-wave velocity (Vs) are indicative of changes in stress because Vs is directly related to shear modulus (μ) and thus material stiffness (**Equation 1**). In this equation, density is represented by ρ.

$$V_s = \sqrt{\frac{\mu}{\rho}} \qquad \textbf{Equation 1}$$

However, longer wavelengths and large sampling volumes smear the resulting pseudo-2D Vs profiles as well as restrict lateral resolution (Zhang et al., 2004; Xia et al., 2004; Ivanov et al., 2006; Boiero and Socco, 2011; Mi et al., 2017). This inherent limitation of the surface-wave method has generally restricted applications of the MASW method to larger-scale (i.e., several tens of meters) void detection investigations, such as those resulting from salt dissolution (Sloan et al., 2009; Ivanov et al., 2013; Morton et al., 2020) or abandoned, underground mines (Billington et al., 2006; Ivanov et al., 2016).

Surface waves form from the interference of reflected body waves, P and vertically polarized SV waves, and propagate along the earth's surface. They consist of both vertical (Rayleigh waves) and horizontal (Love waves) particle motions (Aki and Richards, 1980) (**Figure 1**). In seismic surveys vertical ground (particle) motion is easier to generate and record (Xia et al., 2012a) due to more direct energy transfer of a vertical source impact compared to horizontal source coupling (Häusler et al., 2018). This acquisition challenge generating high-amplitude, long-wavelength horizontal particle motion signal with a horizontally oriented source is principally why investigations using either Love waves or the horizontal component of Rayleigh waves are less common (Eslick et al., 2008). Horizontal or multi-component seismic surveys can be more time-consuming to collect and process often making them less feasible for many investigations. Multi-component sensors (e.g., nodal sensors) and multi-component sources are being developed (Häusler et al., 2018); however, use of these technologies are limited and more difficult to implement in areas that require rapid acquisition procedures due to security concerns (Steeples, 2001).

Sensitivity analyses performed by Ikeda et al. (2015) showed potential for improving Vs estimations by incorporating the horizontal Rayleigh-wave component into the conventional inversion scheme; the conventional inversion scheme uses dispersion information from the vertical component of the Rayleigh wave. Boaga et al. (2013) noted that horizontal component Rayleigh waves exhibit a greater sensitivity to higher-mode surface waves allowing better separation between fundamental- and higher-mode energy in the phase velocity-frequency domain (e.g., dispersion curve image). A velocity profile will possess a higher overall velocity trend when a higher mode is misidentified as the fundamental mode, thus providing an inaccurate representation of the investigated area (Zhang and Chan, 2003; O'Neill and Matsuoka,

2005). Inclusion of horizontal components may be crucial for effectively detecting clandestine tunnels and other challenging targets with surface-wave methods.

This research is a component of a comprehensive seismic study at a tunnel test site in the Arizona Sonoran Desert. Other advancements in the search for improved tunnel detection methods resulting from this study include SH-wave diffraction imaging (Peterie et al., 2020), 2D and 3D full waveform inversion (Wang et al., 2019, and Smith et al., 2019, respectively), and parallel-line beamsteering (Livers et al., 2015; Livers, 2016). This paper extends work presented in Morton et al. (2016) and Morton et al. (2017) where vertical (V), longitudinal (H1), and transverse (H2) data were processed using MASW and BASW. Re-processing of data from these previous works using a shorter receiver line (spread) improved the vertical and horizontal resolution of inverted sections and refocused investigation depths to the upper 15 m of the subsurface. Seismic signatures associated with the tunnel were observed on this study that were analogous to previous work resulting in varying degrees of confidence in each of the data sets and approach. More notably, multicomponent backscatter analysis was performed to determine the feasibility of using horizontal component surface-wave data for improved detection of a tunnel; only vertical component backscatter analysis is found in the current literature. Joint interpretation of multiple numerical and field data sets processed with MASW and BASW (including the multi-component, multi-method approach uniquely developed in this study) is employed in order to improve accuracy and confidence in detecting and locating a tunnel at a test site in the Sonoran Desert.

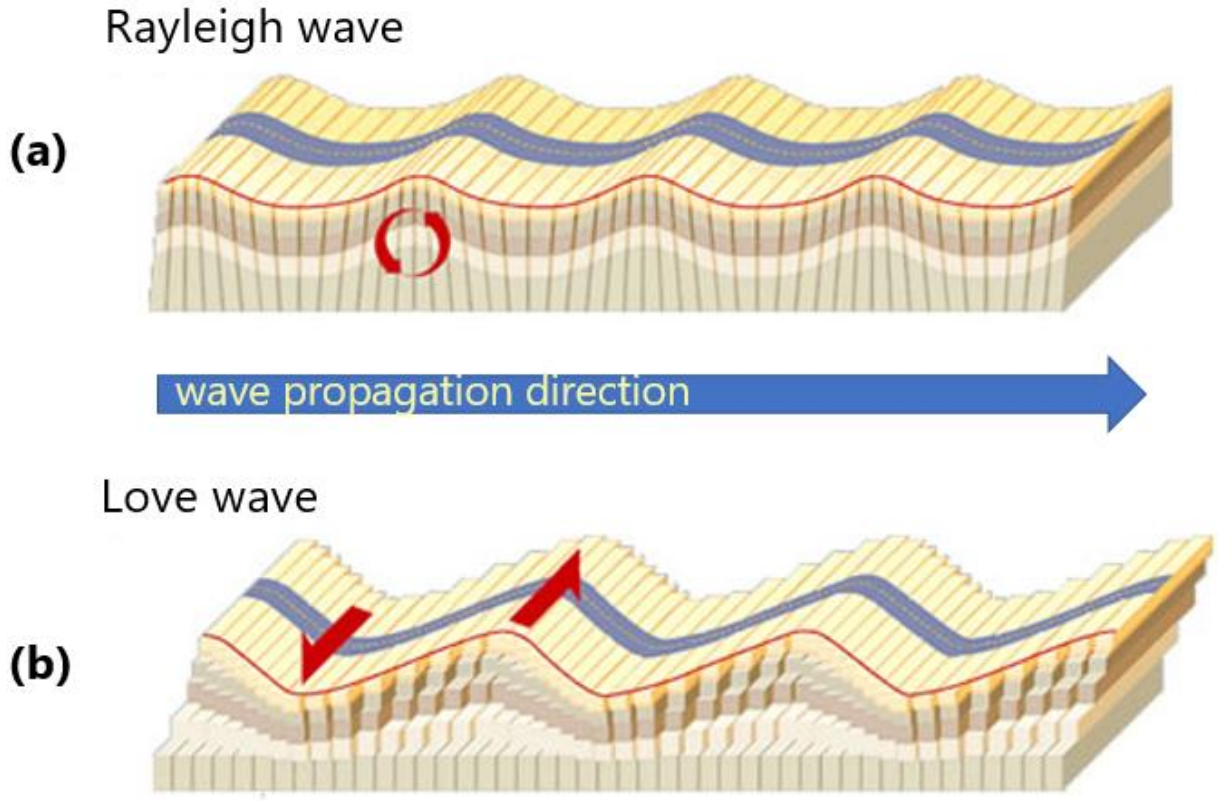

Figure 1. Rayleigh waves propagate with a retrograde elliptical particle motion confined to a vertical plane (b) Love waves are confined to a horizontal plane on the earth's surface and particle motion is perpendicular to the direction of wave propagation (modified from SMS Tsunami Warning, 2018).

Chapter 2: Geologic Setting and Test Site

This study area consists of Holocene to Pleistocene-aged La Posa alluvial plain within the Basin and Range Province where the upper 100 m consists of sand, silt, and gravel (Millet and Barnett, 1970; Sherrod and Tosdal, 1991; McDonald et al., 2009; Miller et al., 2010). Based on nearby borings (Miller et al., 2010), the subsurface materials are primarily characterized by SM (USCS) classification, or silty sands or sand-silt mixtures. For this study, the upper 100 m are summarized in three layers: unlithified silts and sands from approximately 0-7 m depth, gravel and some boulders from 7-28 m depth, and silts and sands below 28 m depth (Schwenk, 2013); no groundwater exists within the upper 90 m. Gravel materials likely originated from Jurassic granitic intrusions of the surrounding overthrust mountain ranges (Ferguson et al., 1994) including the Dome Rock Mountains, North and South Trigo Peaks, and McCoy Mountain Formation

Figure 2) (Sherrod and Tosdal, 1991; Boettcher et al., 2002; Schwenk, 2013). The Late Cretaceous Mule Mountains thrust system contributed to the overthrust mountain ranges (Sherrod and Tosdal, 1991). Along the Mule Mountain system are east to northeast striking tear faults with right-lateral strike-slip offsets that extend for several kilometers (Tosdal and Sherrod, 1985; Sherrod and Tosdal, 1991).

A tunnel 96 m long, 1.2 m wide by 1.5 m tall and approximately at 10 m depth, with wood shoring (**Figure 3**) was hand dug at the Yuma Proving Grounds (YPG) (**Figure 4**) in the Sonora Desert of southwestern Arizona (Sloan et al., 2015). Design parameters of this test tunnel were based on previously discovered clandestine tunnels and included the electrical wiring and ventilation pipe fixed to the top. The tunnel can be accessed from the surface through

a 3 m-wide circular vertical concrete shaft. Given the minimal cultural noise, flat topography, and uniform soil conditions, this site provided an exemplary environment for testing detection methods (Rickards, 2011; Rickards et al., 2011; Sloan et al., 2012).

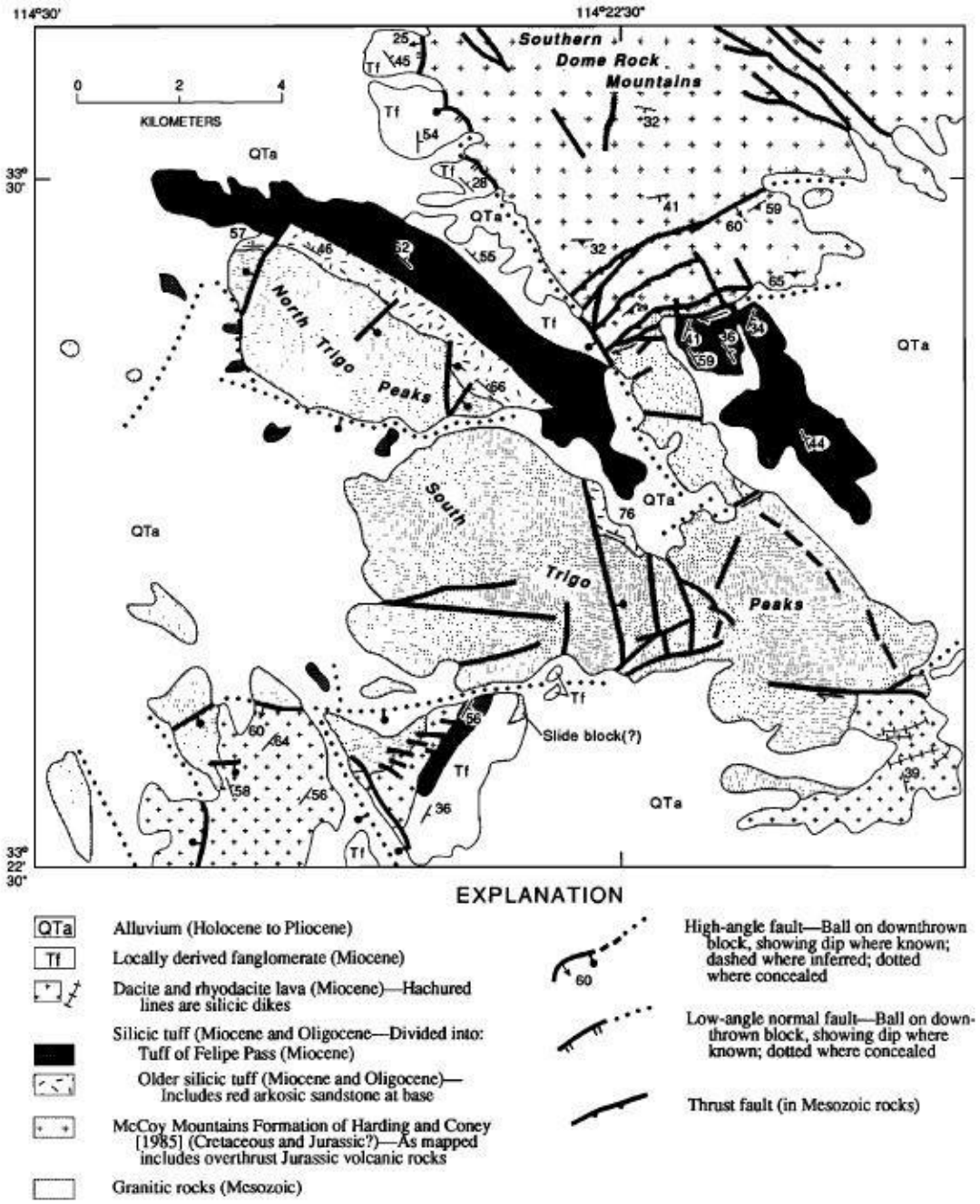

Figure 2. Geologic map of the mountain ranges surrounding the tunnel test site (Sherrod and Tosdal, 1991).

Figure 3. Photograph taken inside a tunnel with wood shoring similar to the tunnel used for testing in this study (Sloan et al., 2012).

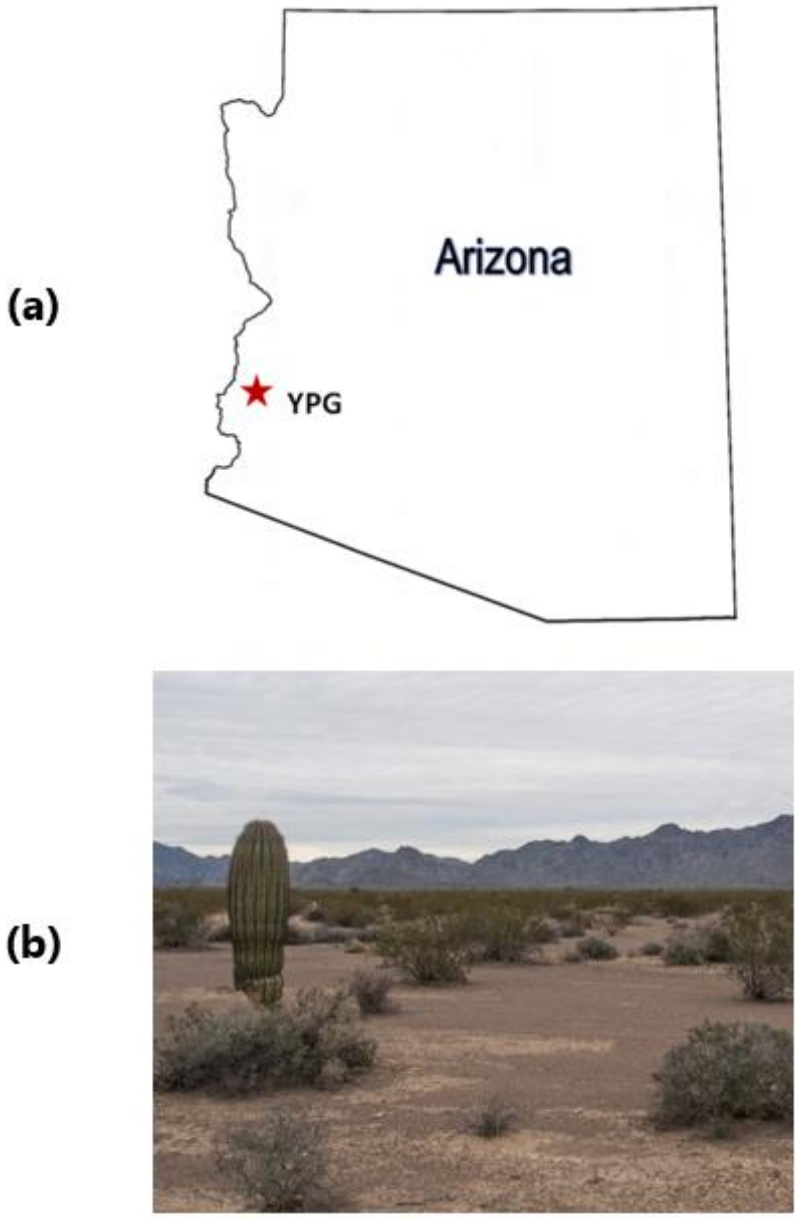

Figure 4. (a) Approximate location of Yuma Proving Grounds in southwestern Arizona (Livers, 2016) and (b) photograph of local environment.

Chapter 3: Data Acquisition and Processing Methods

Multi-component active surface-wave data were collected using matched and co-located 4.5 Hz vertical and horizontal geophones along a fixed, linear array (**Figure 5**). The seismic line (spread) was perpendicular to and centered over the known tunnel located at station 1036 (**Figure 6**). A 30 kg accelerated weight-drop (**Figure 7**) and a 6.8 kg (15-lb.) sledgehammer and shear block source (**Figure 8**) were used to produce vertical (V), longitudinal (H1), and transverse (H2) wave motion; force of the accelerated weight-drop was approximately 2700 N ±5% energy. The fixed spread consisted of 111 receiver locations (stations) separated by 1 m with three vertical and six horizontal (three longitudinal, three transverse) source impacts recorded at each receiver station; three source impacts to each side of the shear block source for six shots total per receiver station. Data were processed using multichannel analysis of surface waves (MASW) first to obtain dispersion curves representative of the subsurface velocity structure (Park et al., 1999). These dispersion curves provided the necessary input surface-wave information for additional backscatter analysis.

An optimal spread length was selected and data sequentially extracted from the full fixed spread (i.e., geophones remain in same location) to simulate a roll-along survey for each of the three surface-wave data sets: (1) the Rayleigh-wave vertical component excited by the weight drop source (vertical [V] data set); (2) the Rayleigh-wave longitudinal (inline) component excited by a shear block in longitudinal orientation (H1 data set); and (3) the Love-wave or transverse (crossline) component excited by a shear block in transverse orientation (H2 data set). A summary of each data set and the data processing performed are listed in **Table 2**. Although horizontal-component data acquisition is more difficult to obtain good source coupling than

vertical-component data acquisition, raw seismic signals (**Figure 9**) recorded during each survey exhibited adequate surface-wave signal amplitudes and wavelengths for surface-wave analysis. SurfSeis^{TM} was used to obtain pseudo-2D MASW Vs sections of inverted Rayleigh waves and Love waves using the MASW method.

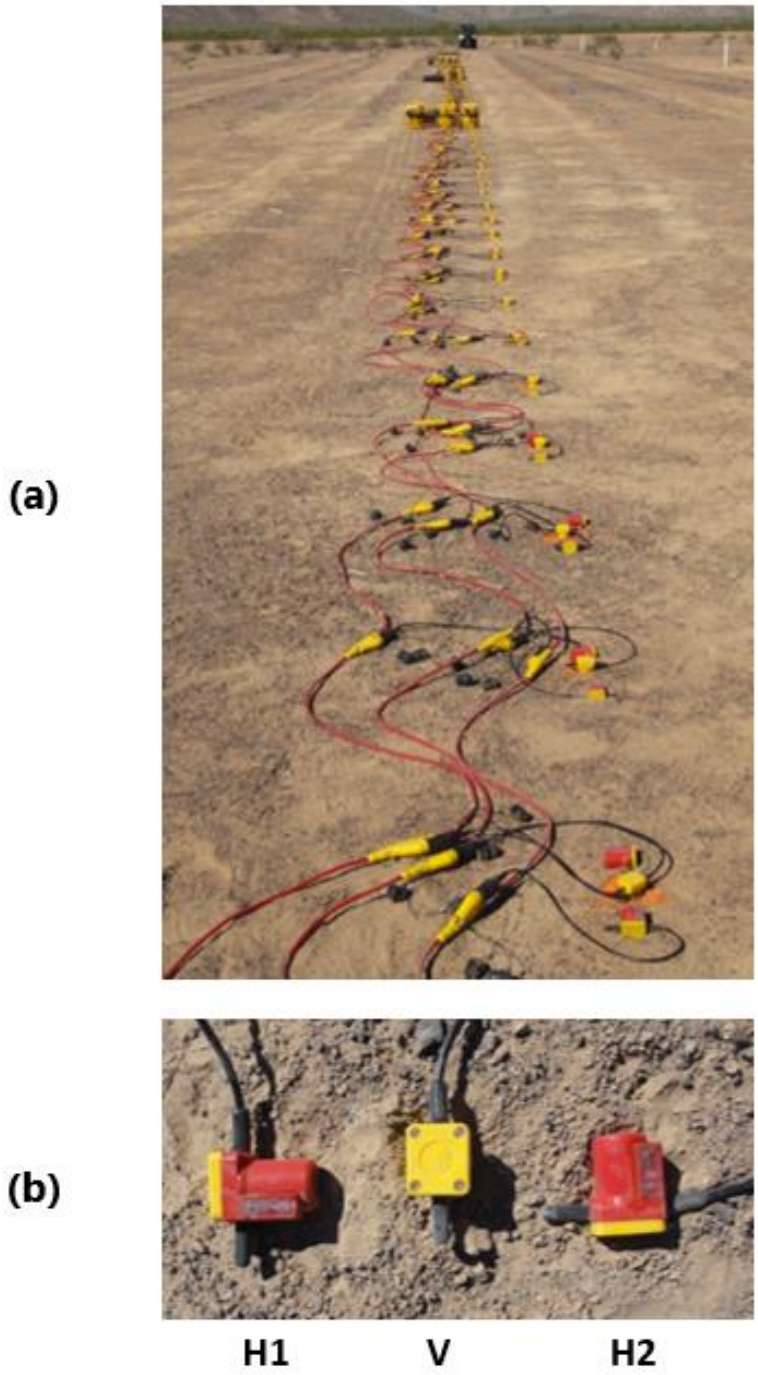

Figure 5. (a) Photograph of the fixed linear seismic array. (b) Three 4.5 Hz geophones were co-located at each station including H1 longitudinal, V vertical, and H2 transverse components (shown from left to right).

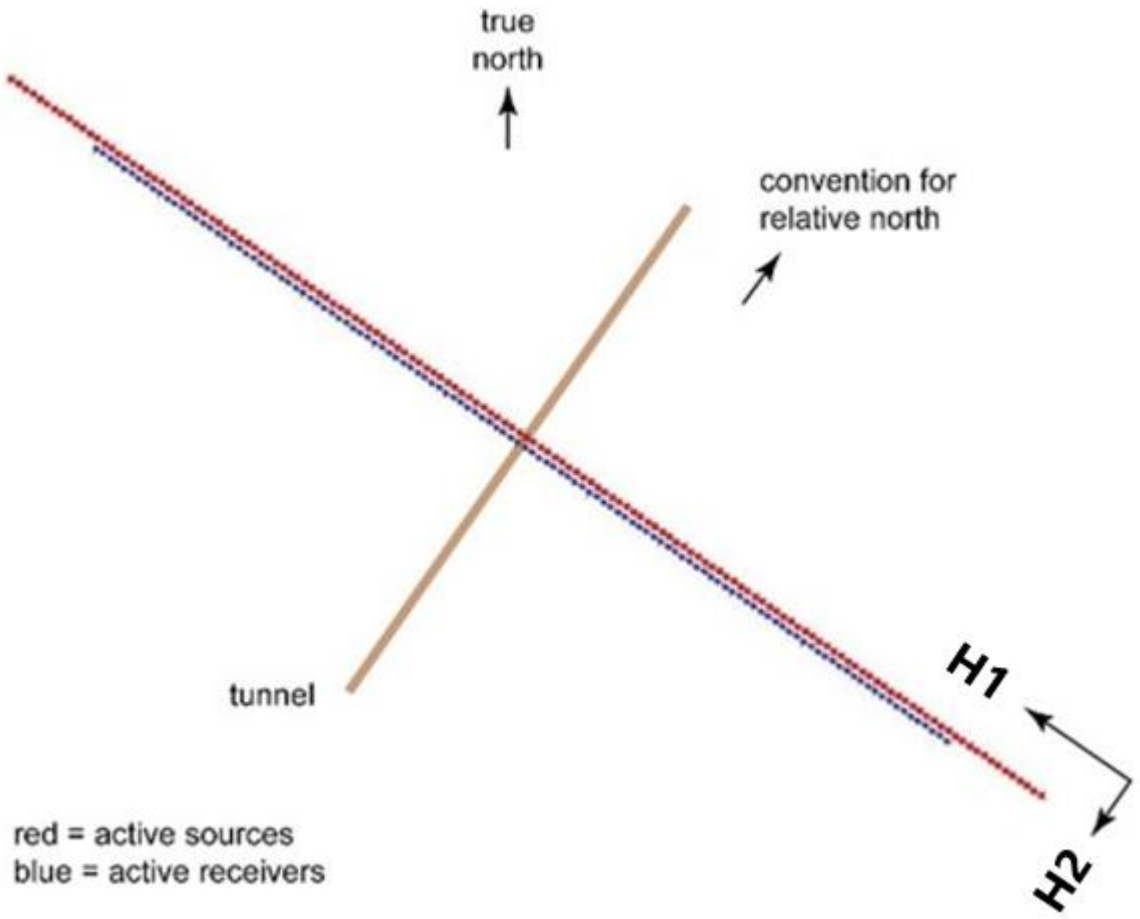

Figure 6. Field survey schematic.

Figure 7. Photograph of the accelerated weight drop source mounted to the front of a modified Bobcat. Photo courtesy of Kansas Geological Survey.

(a)

(b)

Figure 8. Photographs of the shear block oriented for (a) H1 for longitudinal (inline) source energy and (b) H2 for transverse (cross-line) source energy data acquisition. Photos courtesy of Kansas Geological Survey.

Table 1. Field acquisition parameters.

Geophone frequency (Hz)	4.5
Seismic array length (m)	110
Geophone spacing (m)	1
Source spacing (m)	1
Recording length (s)	3
Sampling interval (ms)	1

Table 2. Surface-wave data sets.

Receiver Component	**Source Orientation**		**Source Type**
Vertical	Vertical		Weight drop
H1	Longitudinal (H1)	Inline	Shear block and sledgehammer
H2	Transverse (H2)	Crossline	Shear block and sledgehammer

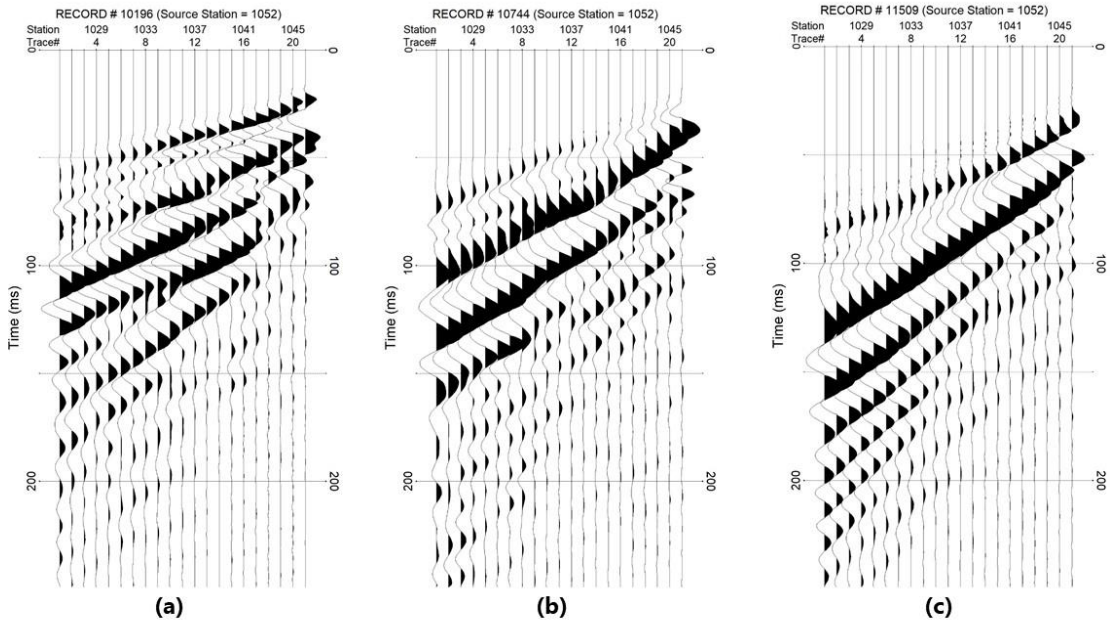

Figure 9. Raw shot gathers of (a) vertical, (b) H1, and (c) H2 data sets.

3.1. Multichannel analysis of surface waves (MASW)

Seismic data were processed using the MASW method (Song et al., 1989; Park et al., 1998; Xia et al., 1999) to generate and pick dispersion curves used to infer subsurface elastic properties such as shear-wave velocity and material layer thickness. Rayleigh-wave dispersion curves are estimated using Knopoff's method (Schwab and Knopoff, 1972) where Rayleigh wave phase velocity (c_{Rj}) is determined using a nonlinear, implicit relationship (**Equation 2**) that is a function of shear-wave velocity ($\boldsymbol{v}_s$), p-wave velocity ($\boldsymbol{v}_p$), density ($\boldsymbol{\rho}$), and layer thickness ($\boldsymbol{h}$) for a given frequency (f_j); vs, vp, ρ, and h are all vectors.

$$F\left(f_j, c_{Rj}, \boldsymbol{v}_s, \boldsymbol{v}_p, \boldsymbol{\rho}, \boldsymbol{h}\right) = 0 \qquad \textbf{Equation 2}$$

where j = 1, 2, …., m

A dispersion image (**Figure 10**) is used to interpret (pick) a dispersion curve which represents the propagation velocity (i.e., phase velocity) at which each frequency of the surface wave propagates in the presence of a vertical velocity gradient. Conventionally, only the fundamental mode dispersion curve is picked and inverted to produce velocity profiles because they provide reliable estimates of shear-wave velocities ± 15% (Xia et al., 1999, 2000, 2002a). The fundamental mode has the lowest phase velocity for a given frequency which is typically the dominant mode of a propagating surface wave; phase velocities higher than the fundamental mode are referred to as higher modes. Higher modes or harmonics of the surface wave can interfere or be misidentified as the fundamental mode trend if these modes travel at similar velocities (Zhang and Chan, 2003). An accurate estimate of inverted velocity and layer thickness require picked dispersion curves be appropriately assigned as the first order (i.e., fundamental mode), second order (i.e., higher mode 1), third order (i.e., higher mode 2), etc.

In cases where the fundamental mode and higher modes exhibit adequate separation in propagation characteristics (**Figure 11**), trends from all modes can be selected and simultaneously inverted to increase stability during the inversion process (Xia et al., 2003; Xu et al., 2006; Song et al., 2007). Instabilities result when estimated data are unable to fit the measured data (i.e., picked dispersion curve) within the designated error criterion; these instabilities often lead to high root-mean-square (RMS) error and Vs sections that are not geologically valid. Since higher modes are noted for higher sensitivity to certain inversion model parameters than fundamental modes (Socco and Strobbia, 2003), including more than one mode in the inversion procedure has proven to provide more accurate Vs section(s) (Maraschini et al., 2010) and enhance vertical resolution of the inverted model (Xia et al., 2003; Song et al., 2007).

Rayleigh waves (i.e., vertical, longitudinal components) and Love waves (i.e., transverse component) were recorded and individually processed using the MASW method (Song et al., 1989; Park et al., 1998; Xia et al., 1999; Xia et al., 2012a). The MASW method (**Figure 12**) can be separated into three key steps: (1) acquire seismic data, (2) transform time-domain data to phase velocity-frequency domain to identify dispersion curves, and (3) invert selected dispersion curves to produce a 1D shear-wave velocity-depth model. These 1D models can be combined spatially to produce a pseudo-2D MASW Vs section (Miller et al., 1999) of the subsurface; pseudo-2D MASW Vs sections are henceforth referred to as MASW Vs sections. This display format allows inferences about the geologic environment and local velocity heterogeneities with potential geologic significance.

The resolution of inverted surface-wave data depends on the resolution of dispersion curves (Zhang et al., 2004). MASW data, in particular, requires specific survey geometry to allow surface waves to fully develop during data acquisition (Park et la., 1999; Xia et al., 2004;

Zhang et al., 2004). Dispersion-curve resolution, derived from MASW data, depends on three parameters; (1) closest source-to-receiver spacing, often referred to as source offset, (2) receiver spacing within the receiver spread, and (3) total spread length (Park et al., 2001). These factors affect how easily phase velocity is discriminated from other phase velocities for a given frequency (Park et al., 1998; Zhang et al., 2004), which subsequently affects the horizontal resolution of inverted MASW data (Xia et al., 2004). For a given spread length, *X*, increasing the number of receivers can yield higher-resolution dispersion-curve images (Park et al., 2001). For example, a 30 m spread with 30 receivers (i.e., 1 m receiver spacing) should result in higher-resolution dispersion curves than a 30 m spread with only 15 receivers (2 m receiver spacing). Vertical resolution of inverted MASW data is controlled by the lowest available frequency of a given data set as well as the number and thickness of layers used in the inversion algorithm (Rix and Leipski, 1999). Therefore, it's critical that an optimal geophone spread is extracted from each seismic record to limit the damaging effects of these higher modes and minimize smearing in the final inversion result.

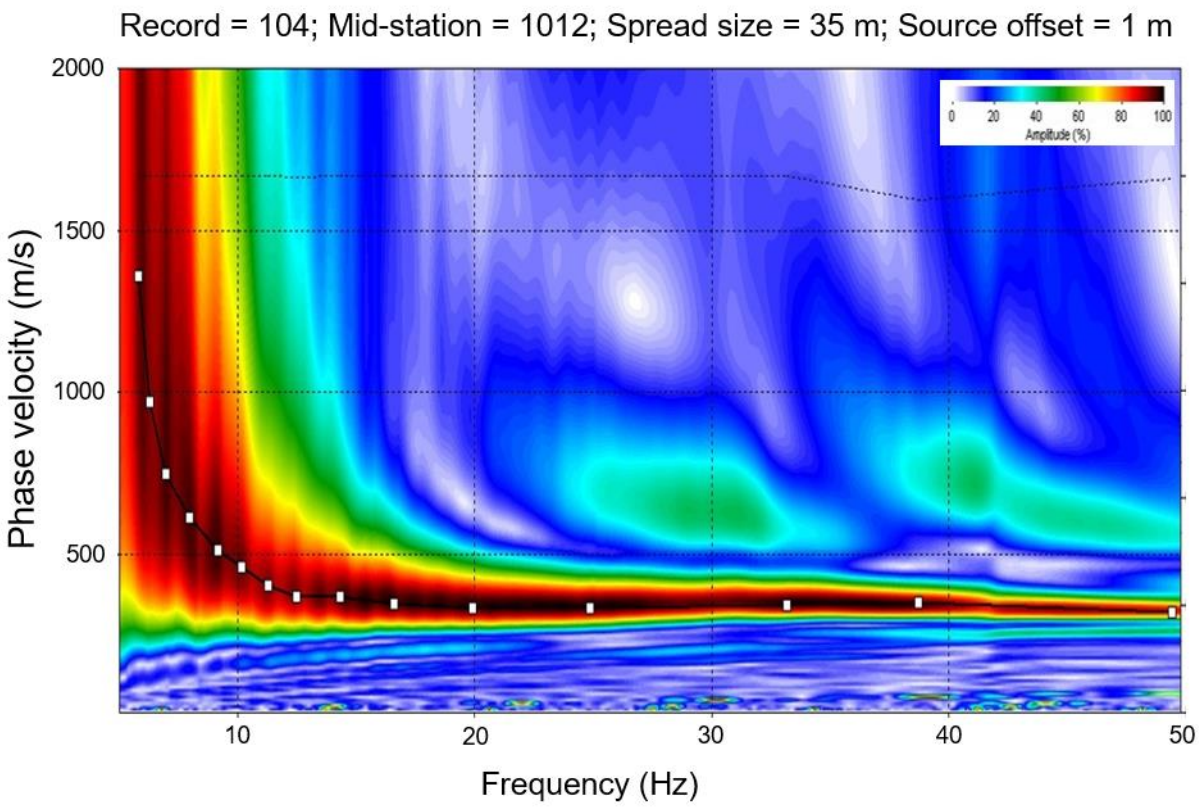

Figure 10. Example dispersion image with a picked fundamental mode curve; modified from Morton (2014).

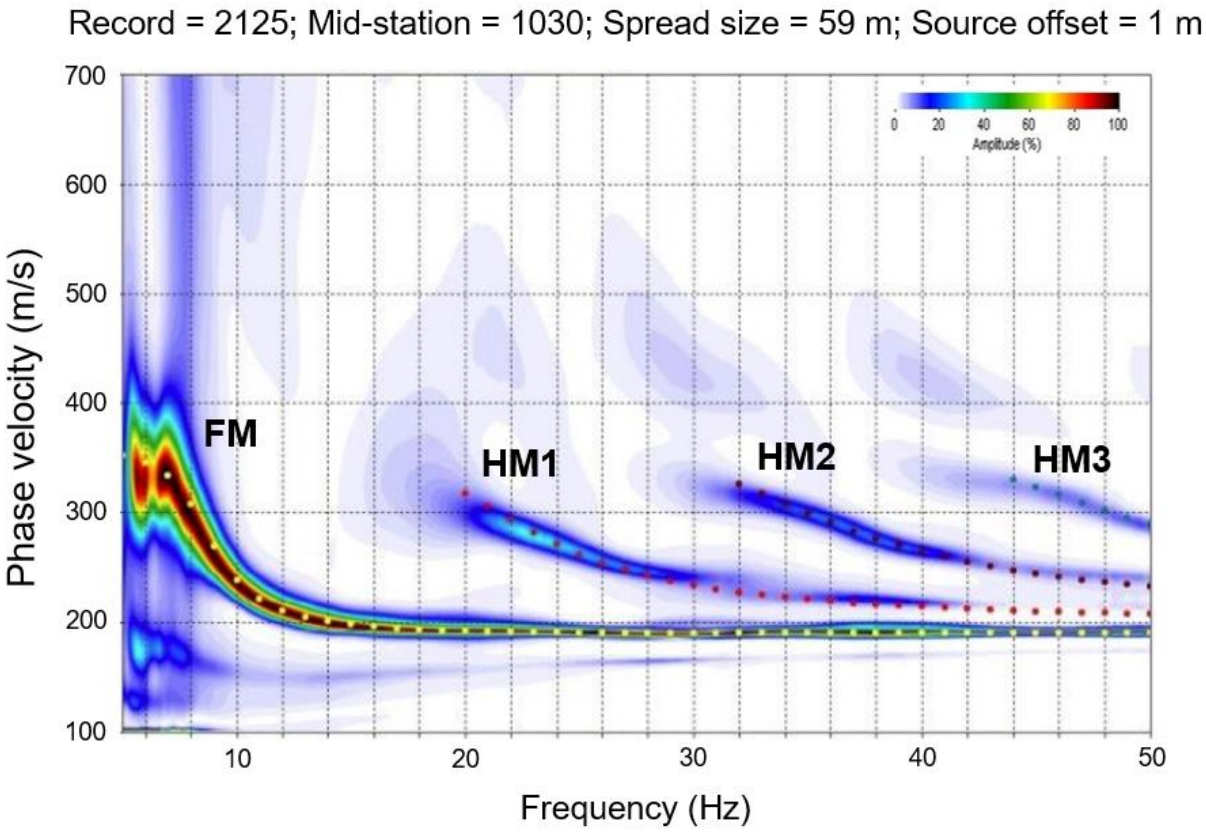

Figure 11. Example dispersion curve trends for a fundamental mode and three higher modes; modified image courtesy of the Kansas Geological Survey.

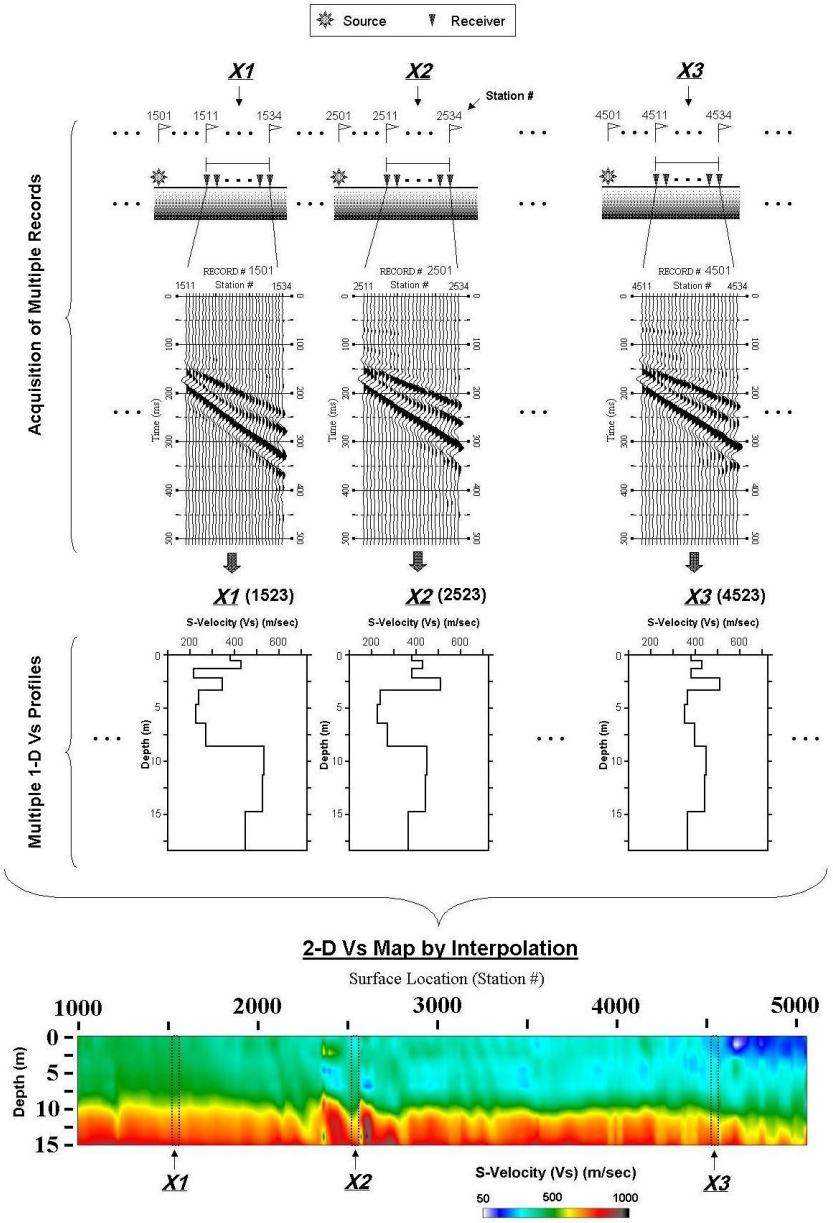

Figure 12. Three-step summary of the MASW method; image courtesy of Kansas Geological Survey.

3.1.1. Initial processing efforts

Processing of 2016 surface-wave data began with the extraction of unique 65 m-long geophone spreads with a 1 m offset source from the fixed 110 m-long receiver spread to simulate a roll-along spread for each surface-wave data set. Spread geometry is based on previous surface-wave testing by Schwenk (2013) also conducted at the tunnel test site. This earlier work in 2009 provided shear-wave velocity estimates (**Figure 13**) to aid in establishing baseline velocity conditions at the Yuma Proving Grounds. The 2016 work is aimed to resolve a small 1 m wide by 1.5 m tall tunnel at approximately 10 m depth. Therefore, the spread geometry must be taken into consideration to produce results where the resolvable limits of the recorded surface-wave data are appropriate for imaging the target of interest. In the initial analysis of the 2016 data, coherent dispersion-curve trends were selected from approximately 5-65 Hz (**Figure 14**) and inverted to estimate the final MASW Vs section from each data set.

Vertical source dispersion data suffered from significant higher mode interference above 25 Hz that inhibited the fundamental mode energy as shown in **Figure 14a**. This higher-mode Rayleigh-wave energy became more dominant as the midpoint of the spread approached the tunnel, but no distinct feature in the fundamental mode dispersion curves or inversion results related to the tunnel could be made. Similar higher-mode interference affected the fundamental mode above approximately 30 Hz in the 2009 data set (**Figure 15a**). Schwenk (2013) applied a linear mute (Ivanov et al., 2005) to seismic shot gathers to increase fundamental-mode signal at higher frequencies. As a result of muting, fundamental-mode phase velocities were enhanced above 30 Hz, increasing signal bandwidth to at least 50 Hz (**Figure 15b**). However, Ivanov et al. (2005) and Schwenk (2013) both noted decreased fundamental-mode coherency at low frequencies after muting which adversely affected confidence when attempting to interpret the

full fundamental-mode trend (e.g., below 20 Hz in the Schwenk (2013) data set). An alternative fundamental-mode enhancement tool is the dispersion curve frequency-wavenumber (DCFK) filter which uses a user-defined bow-slice shape as the filter cutting zone within the frequency domain (Park et al., 2002; Morton et al., 2015), rather than the conventional *f-k* (i.e., pie-slice) filter which uses two linear slopes in the shape of a fan in the *f-k* domain (**Figure 16**). This thin, curved filtering zone uses the criterion in **Equation 3** to filter phase velocity C_ω at frequency ω.

$$C_\omega = \frac{\omega}{k_x} \qquad \textbf{Equation 3}$$

As a result, this filter successfully enhanced fundamental-mode energy between 20-60 Hz thus providing the necessary dispersion-curve selection for the inversion scheme (**Figure 17**).

The vertical data set yielded a MASW Vs section (**Figure 18a**) that supported the previously defined geologic conditions (Schwenk, 2013) at this site with a high velocity (500-600 m/s) layer from 10-15 m over under-lying lower velocity (200-400 m/s) materials. However, no evidence of the tunnel was observed below station 1036, the known tunnel location. Remarkably, the H1 MASW Vs section (**Figure 18b**) revealed a disturbance in the high velocity layer between 10-15 m displayed as an arch-shaped velocity anomaly below stations 1030-1040. The H2 MASW Vs section in **Figure 18c** surprisingly did not produce a result that was indicative of the known conditions, nor was a tunnel signature observed. After reviewing the dispersion curve images, the H1 and H2 cases yielded continuous, high-amplitude fundamental mode trends with minimal to no influence by higher mode energy (**Figure 14**).

In general, longer spreads reduce lateral resolution (Ivanov et al., 2008) because spread length dictates the size of the sampled volume. That sampled volume is averaged together during inversion for each 1D Vs profile which subsequently smears small heterogeneities when longer spread lengths are used. A brute estimate of surface wave data resolution can be determined

using dispersion curve values and **Equation 4** where v is the measured phase velocity (m/s), λ is the surface wave wavelength (m), and f is frequency (Hz).

$$\lambda = \frac{v}{f} \qquad \textbf{Equation 4}$$

The shortest and longest available wavelengths of the recorded data are determined using the picked phase velocities that correspond to the highest and lowest frequency values, respectively. Minimum and maximum depth (z) of investigation is equal to half ($z = \lambda/2$) the shortest and longest wavelength values (Xia et al., 1999; Zeng et al., 2009). Based on the vertical component data with a 65 m spread, the sampling limits of the data in its current form were approximately 1.95 m (z_{min}= 251.6/64.3 = 3.9/2 = 1.95 m) and 38.85 m (z_{max} = 404/5.2 = 77.7/2 = 38.85 m). For a 10-layer inversion model and an assumed equal layer thickness, the thickness of each inverted layer (z_i) is approximately 3.7 m (38.85-1.95 = 36.9/10 = 3.7 m) which is larger than the dimensions of the tunnel. Consequently, the tunnel was outside the detectable limit of the dataset with a 65 m spread and 1 m source offset due to smearing within the large sampling volume.

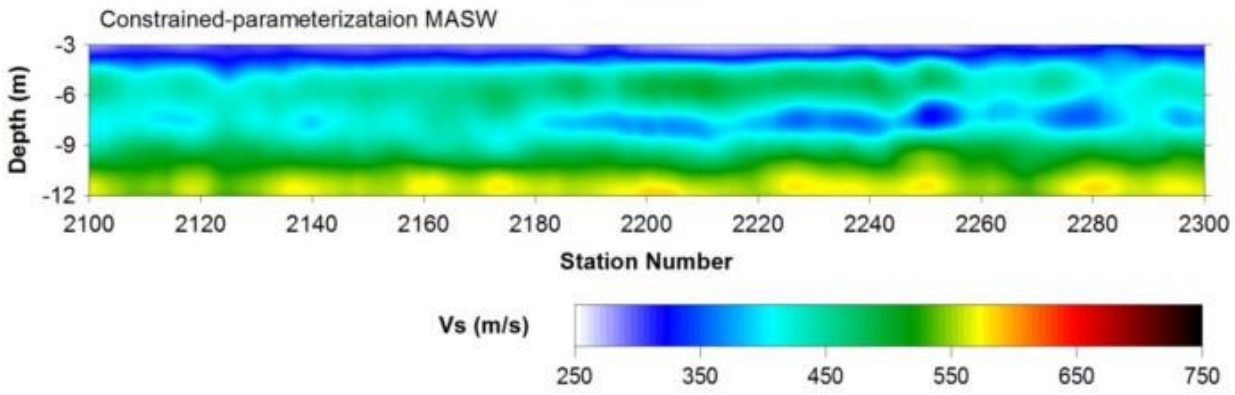

Figure 13. MASW Vs section from 2009 data set collected at the Yuma Proving Grounds by Schwenk (2013) using a 65 m spread, 1 m source offset.

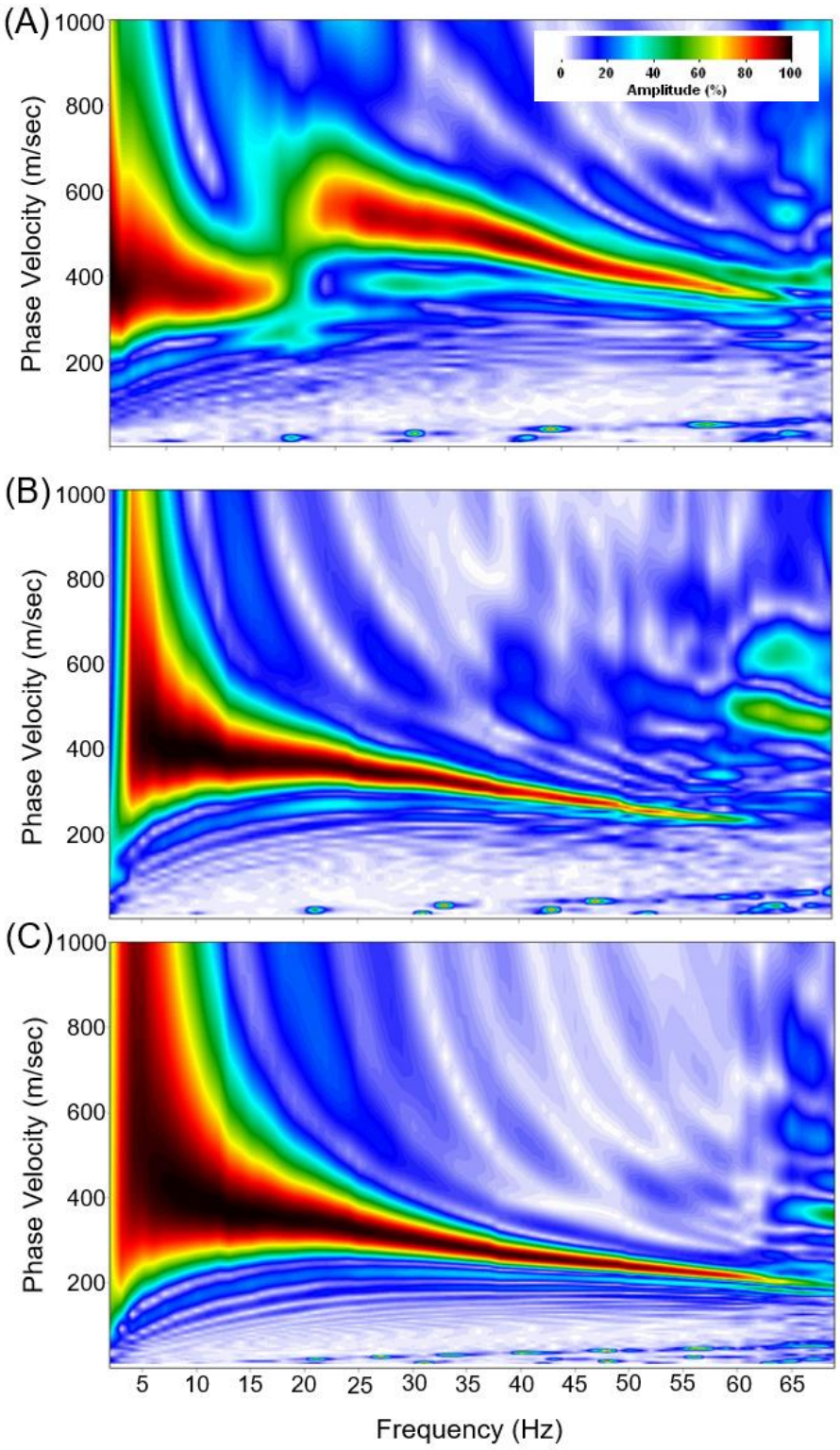

Figure 14. Raw dispersion curves from the 65 m spread corresponding to the (a) vertical, (b) H1, and (c) H2 data sets; modified from Morton et al. (2017).

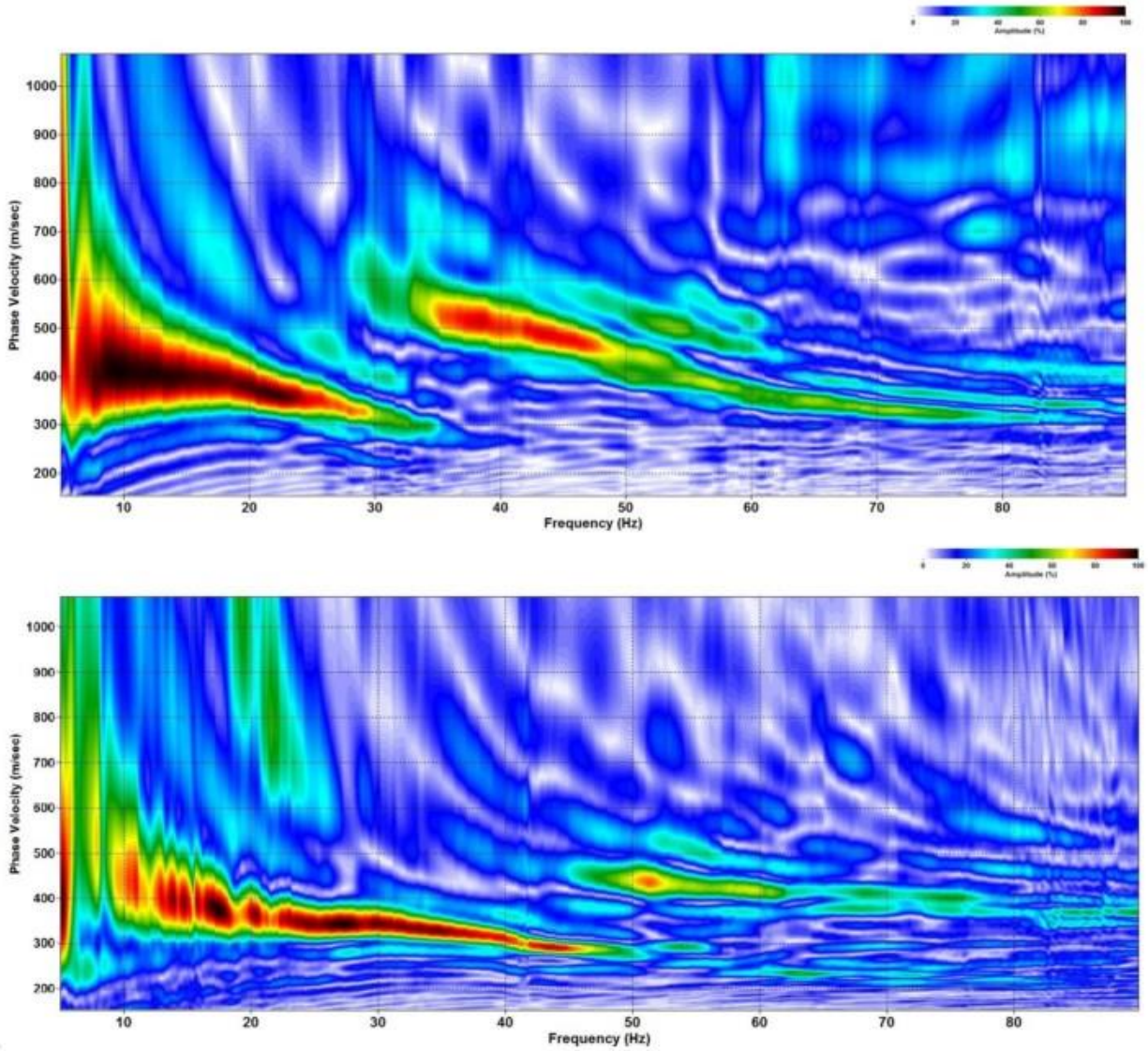

Figure 15. (Top) Unmuted dispersion-curve image with dominant higher-mode contamination above 30 Hz. (Bottom) Muted dispersion-curve image with reduced higher mode and enhanced fundamental mode (from Schwenk, 2013).

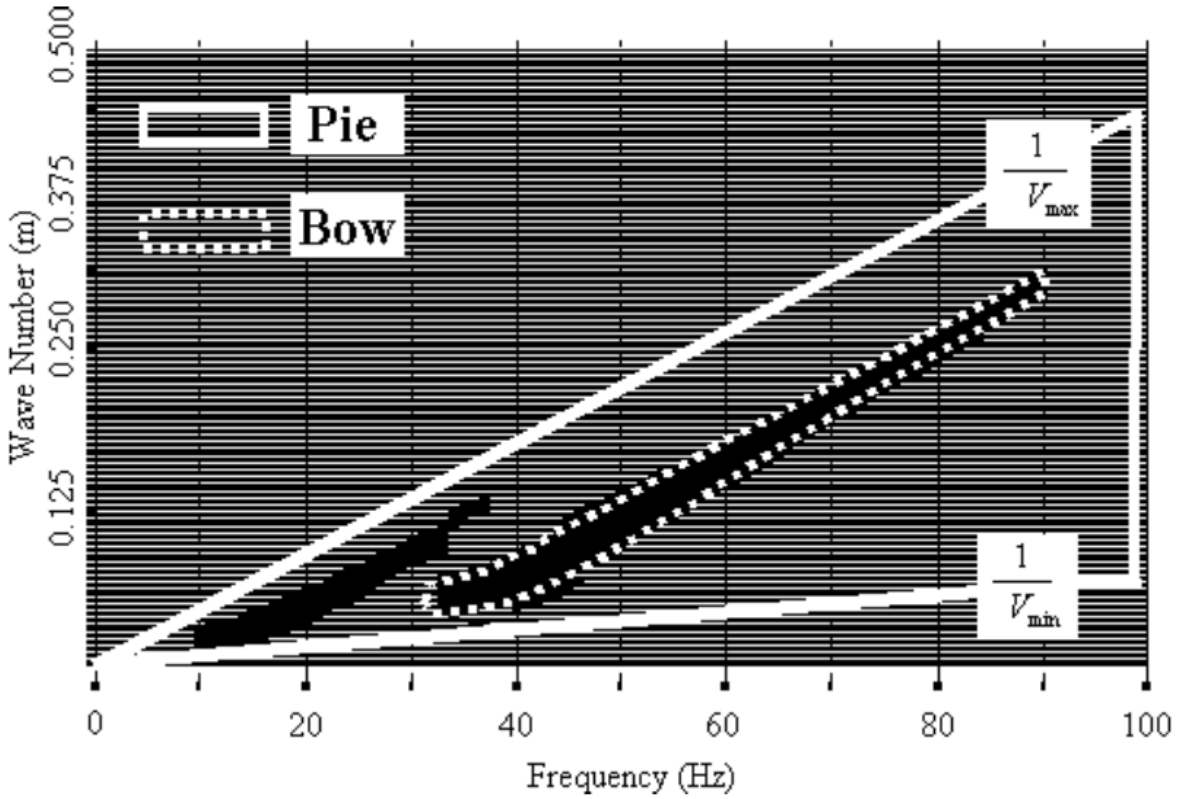

Figure 16. Frequency-wave number amplitude spectrum of a seismic shot gather. Area outlined with solid white lines indicates cutting zone designated using the conventional pie-slice filter. Area outlined with dashed white lines indicates thin, curved cutting zone designated using DCFK filter. Figure from Park et al., (2002).

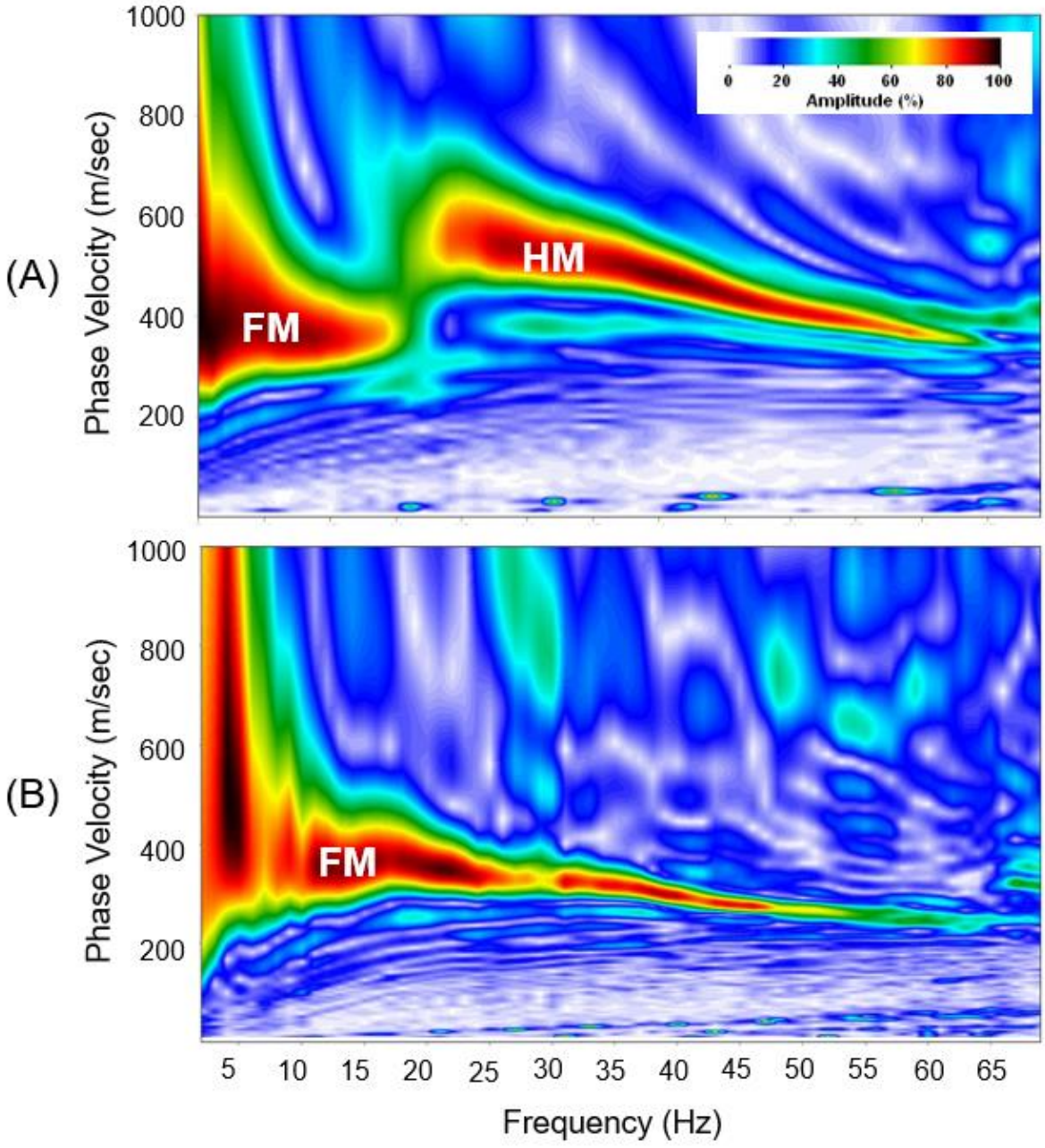

Figure 17. Vertical data set dispersion curves (a) before filtering and (b) after filtering to unmask fundamental mode (FM) at higher frequencies by reducing interference from higher mode (HM).

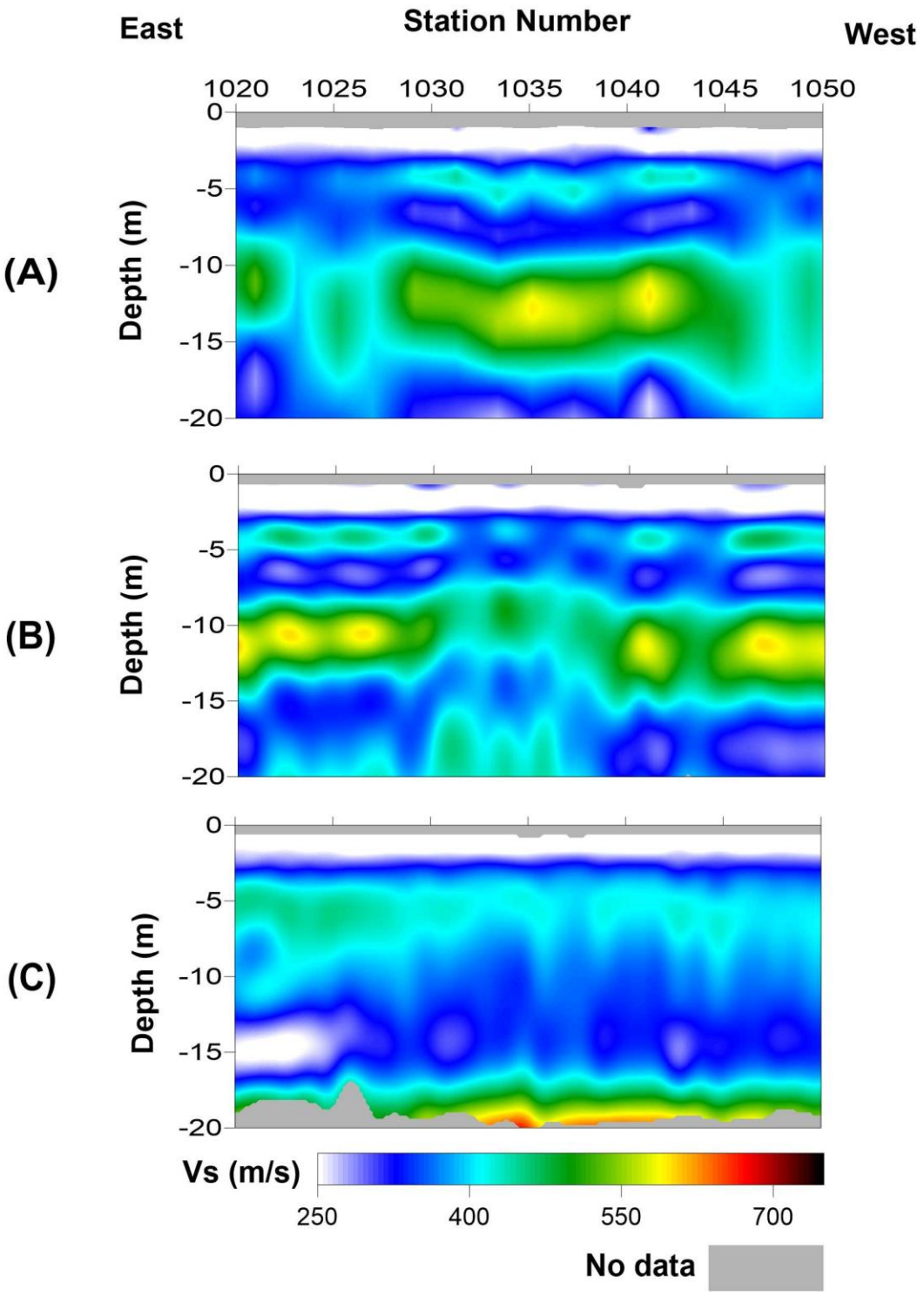

Figure 18. Final MASW Vs sections using a 65 m spread corresponding to the (a) vertical, (b) H1, and (c) H2 data sets; modified from Morton et al. (2017).

3.1.2. Optimal spread-size testing

To prepare a data set with spread geometry such that the tunnel depth and its dimensions are within the detectable limits of the recorded surface wave information, receiver spread lengths shorter than 65 m were extracted from the fixed array. It is critical that spread geometry maximizes lateral resolution of the final MASW Vs section, while preserving the coherency of the fundamental mode across an adequate frequency range (Park et al., 2001; Ivanov et al., 2008). Varying receiver spread lengths were extracted from the vertical data set ranging from 15 m to 40 m. In general, the fundamental mode became less susceptible to higher-mode interference as spread length decreased from 40 m to 15 m (**Figure 19**). This dominant higher mode was also observed in the 65 m data set where fundamental-mode frequencies higher than ~25 Hz were attenuated by a dominant higher mode (**Figure 14 and Figure 16**). With the 40 m spread, the uninterrupted fundamental mode was observed from approximately 5-26 Hz (**Figure 19**); this yielded sampling limits (**Table 3**) from approximately 5.8 m (z_{min}= 313/27 = 11.6/2 = 5.8 m) and 40.4 m (z_{max} = 400/4.95 = 80.8/2 = 40.4 m). For a 10-layer inversion model and an assumed equal layer thickness, the thickness of each layer is approximately 3.46 m (40.4-5.8 = 34.6/10 = 3.46 m) which still exceeds the dimensions of the tunnel. A high-amplitude fundamental-mode was observed from 10-37 Hz for a 30 m spread.

Shorter receiver spreads accompanied by longer source offsets are also an effective way to minimize near-field effects that reduce fundamental mode coherency (Heisey et al., 1982; Ivanov et al., 2008; Foti et al., 2018). As a result, an optimal 20 m spread with 6 m source offset (**Figure 20**), as opposed to the 1 m source offset, provided coherent dispersion curves within an adequate frequency range and sufficient separation between the fundamental and first higher

mode. The segregated spreads were transformed to phase velocity-frequency domain where dispersion curves were picked and inverted to produce a Vs depth trace.

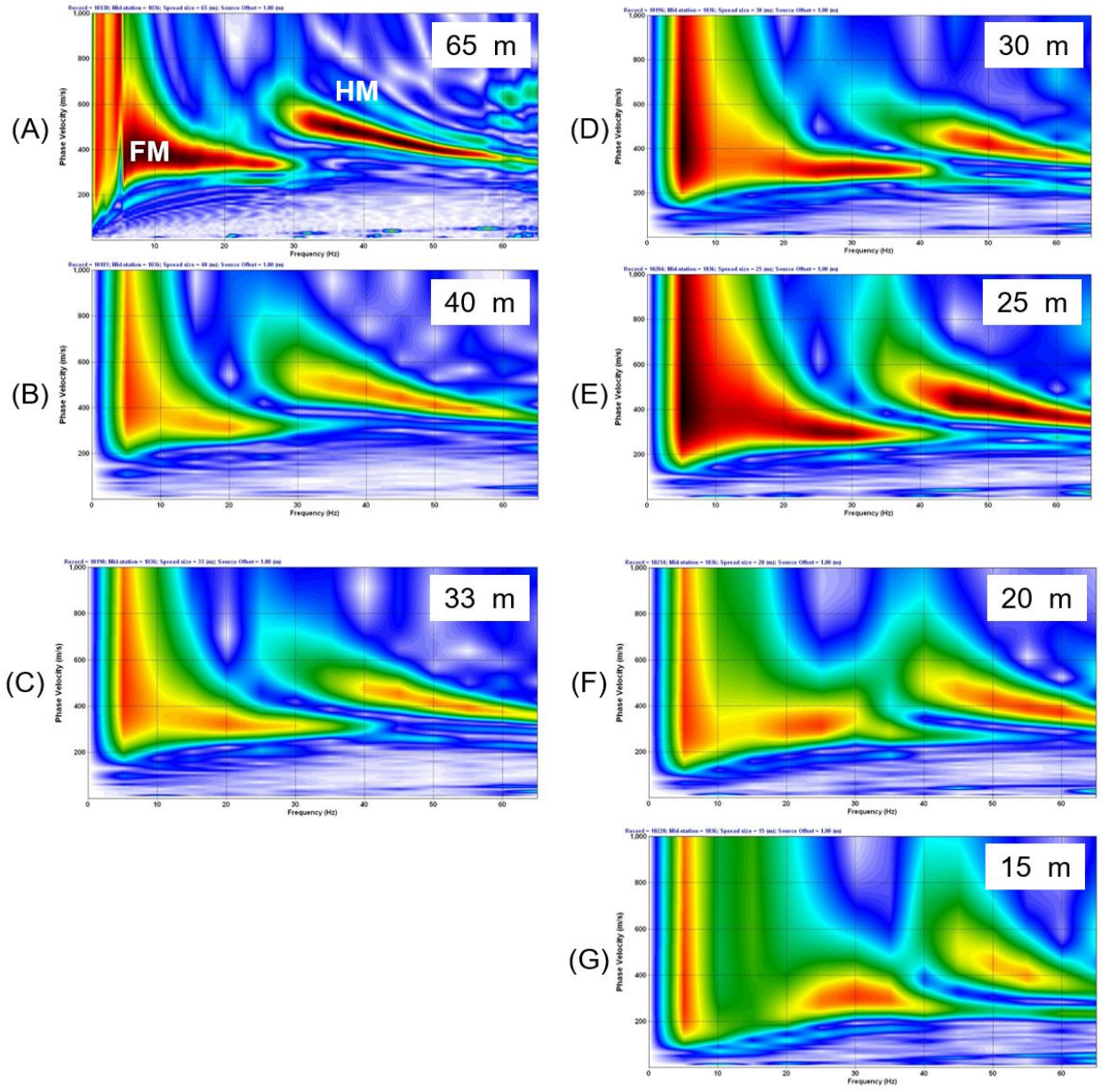

Figure 19. Raw dispersion curves extracted from (a) 15 m, (b) 20 m, (c) 25 m, (d) 30 m, (e) 33 m, and (f) 40 m spread lengths with 1 m source offsets.

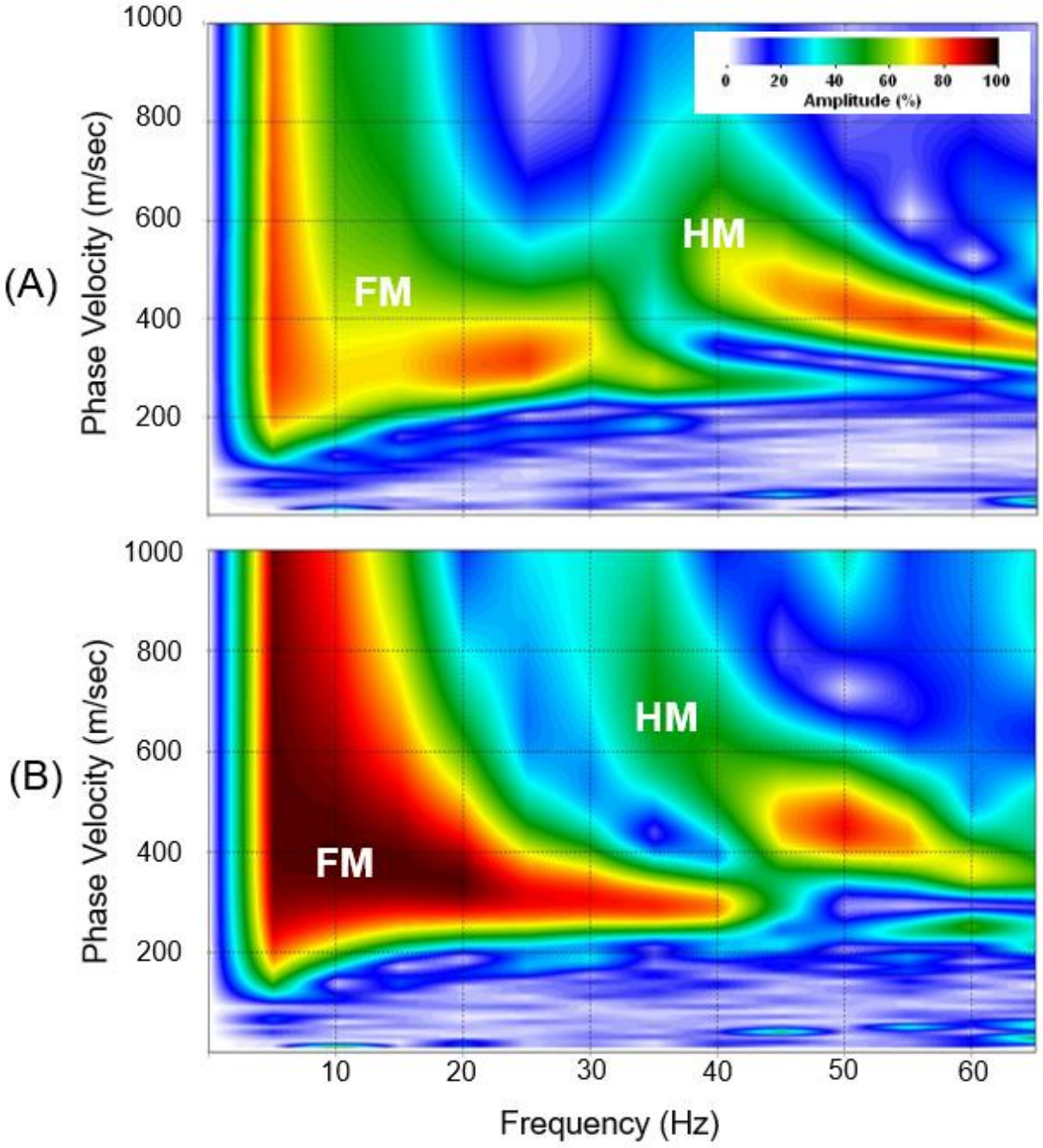

Figure 20. Dispersion-curve images using a 20 m spread with (a) 1 m source offset and (b) 6 m source offset.

Table 3. Estimated sampling limits of spread tests.

Spread length (m)	Source offset (m)	λ_{min} (m)	λ_{max} (m)	z_{min} (m)	z_{max} (m)	z_i (m)
65	1	3.9	77.7	1.95	38.85	3.7
40	1	11.6	80.8	5.8	40.4	3.5
33	1	8.1	93.6	4.05	46.8	4.3
30	1	4	74.3	2	37.15	3.52
25	1	3.4	62.6	1.7	31.3	2.96
20	1	3.7	35.3	1.85	17.65	1.58
20	6	2.95	33.4	1.48	16.7	1.52
15	1	3.6	17.6	1.8	8.8	0.74

3.2. Backscatter analysis of surface waves (BASW)

A surface wave propagation path can be perturbed after encountering a velocity heterogeneity (Campman et al., 2003; Riyanti et al., 2005). These heterogeneities/discontinuities cause scattering of portions of the seismic wavefield (Herman et al., 2000; Luke and Calderon-Macias, 2008). This scattering can be demonstrated using a simple, two-layer model (**Figure 21**). Backscatter is observed in raw seismic data as seismic waves approache and passe the lateral location of the heterogeneity (**Figure 22**). The horizontal location of the discontinuity that caused the scattering can be estimated using the BASW method (Ivanov et al., 2003; Sloan et al., 2010; Schwenk et al., 2014; Sloan et al., 2015). It is important to note that the BASW imaging method assumes a linear projection of scattered surface waves across a horizontal distance (Schwenk et al., 2016).

The BASW method includes several steps (**Figure 23**). First, data are vertically stacked (e.g., individual traces from each record are summed) to increase the signal-to-noise ratio and *f-k* filtered to attenuate the amplitude of forward-propagating waves. Then a (frequency-variant, FV) linear move out (LMO) correction (**Equation 5**) is applied to shot gathers in one of two ways: (1) a constant velocity model or (2) a dispersion-curve velocity model extracted from one representative dispersion curve.

$$P_{FV-LMO}(x,\omega) = \varphi\_(x,\omega)P(x,\omega) \qquad \textbf{Equation 5}$$

In **Equation 5**, $P_{FV\text{-}LMO}$ is the phase-shifted 1D Fourier transform, P(x,ω), where x is the distance from the seismic source and ω is angular frequency (Park et al., 2002; Schwenk et al., 2016). Phase shift, ϕ_(x,ω), is a factor of the phase velocity, Cω, and frequency, ω, pair defined using a picked dispersion curve (**Equation 6**). Intrinsic positive moveout is removed using the negative phase shift defined as ϕ_.

$$\varphi_{-(x,\omega)} = e^{-ix\omega/C_\omega} \qquad \textbf{Equation 6}$$

Direct backscatter energy is shifted to time zero by the LMO correction if the velocity model accurately represents the characteristics of the backscatter; the apex will be delayed in time if an inaccurate velocity model is used for the LMO correction. The station number where the apex of the backscatter (e.g., dipping event) crosses time zero indicates its lateral location. Common receiver stacking results in constructive stacking of surface-wave backscatter, forming a 2D backscatter cross-section (i.e., BASW section).

This process, using one of the two LMO corrections mentioned earlier, is repeated for each surface-wave data set. Although the 20 m spread, 6 m offset survey geometry yielded optimal dispersion-curve information for MASW processing, the 65 m spread allowed wavelength information from both short and long offsets to contribute to this analysis. Short and long offset surface-wave information (**Figure 22**) should be considered during BASW processing to account for all forward-propagating surface waves in recorded data.

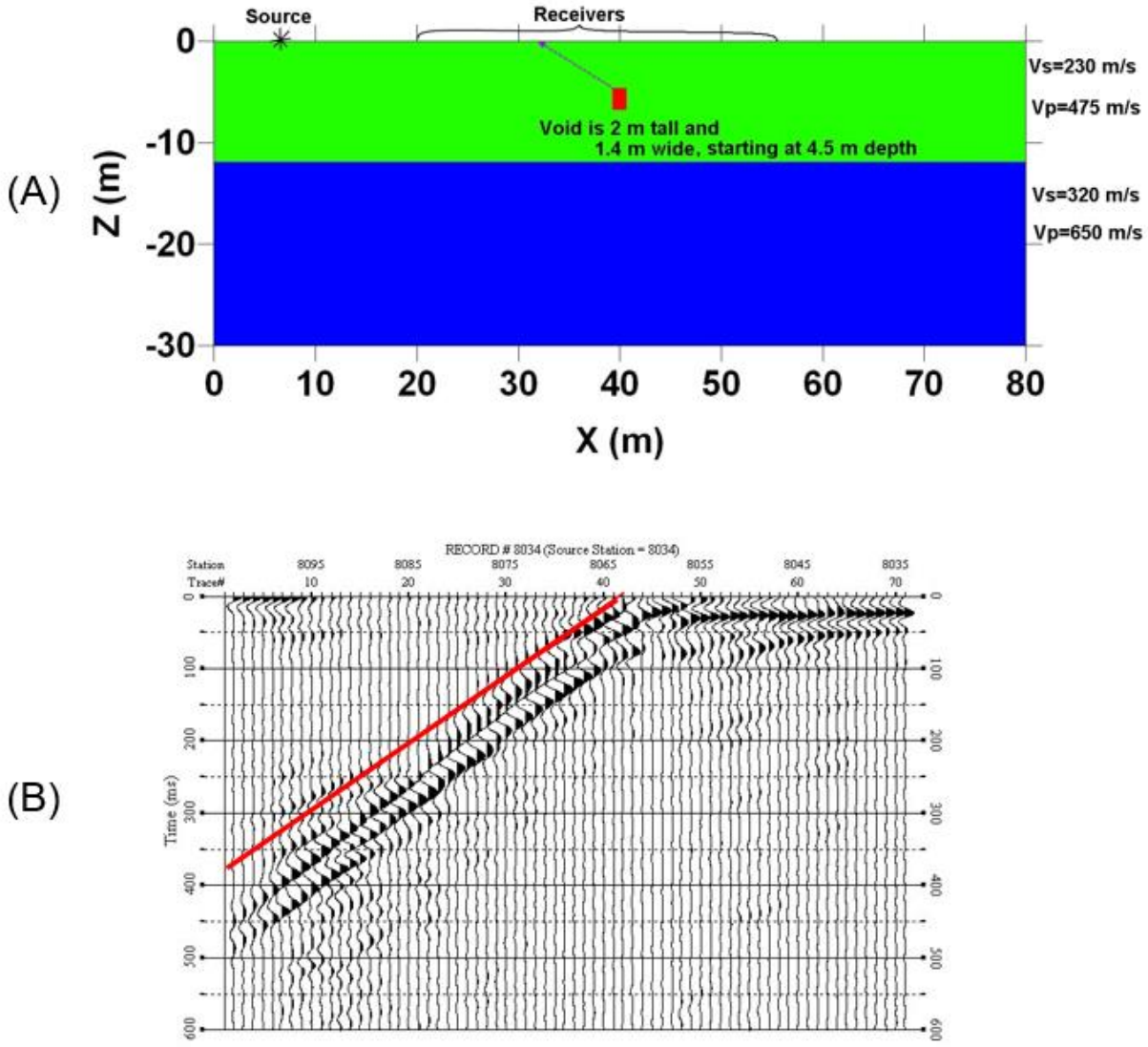

Figure 21. (a) Simple two-layer model with a velocity heterogeneity in the upper layer (red box in center). (b) As the seismic energy source approaches and passes the lateral location of the heterogeneity, a backscatter is be observed on processed data. Figures courtesy of Kansas Geological Survey.

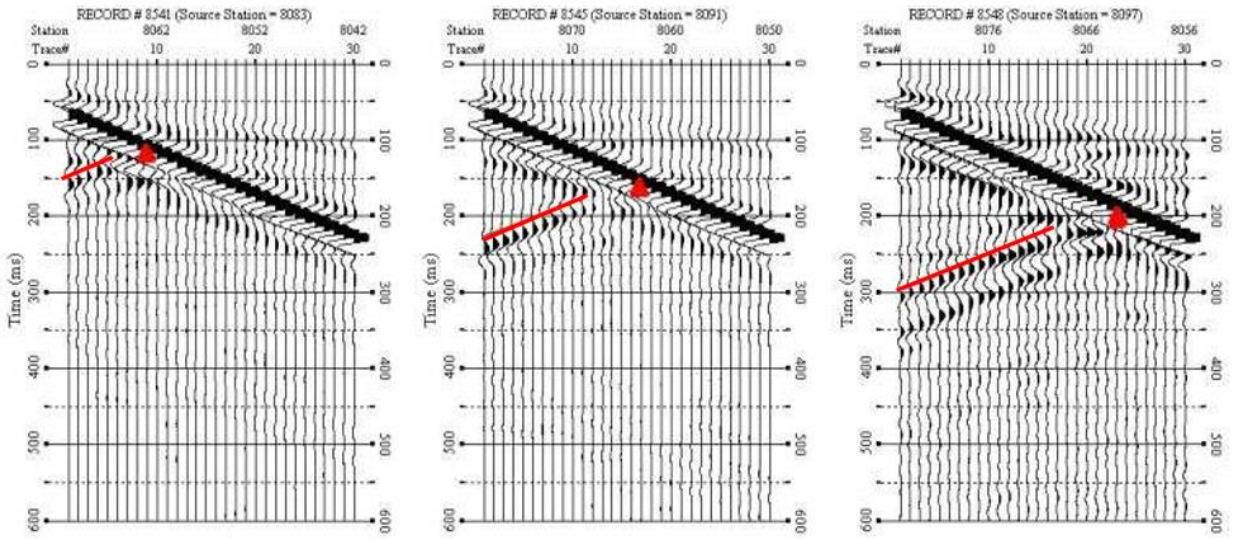

Figure 22. Synthetic seismic shot records illustrating surface-wave backscatter (red line) at increasing distances between the seismic source and void (red triangle). From Sloan et al., (2010).

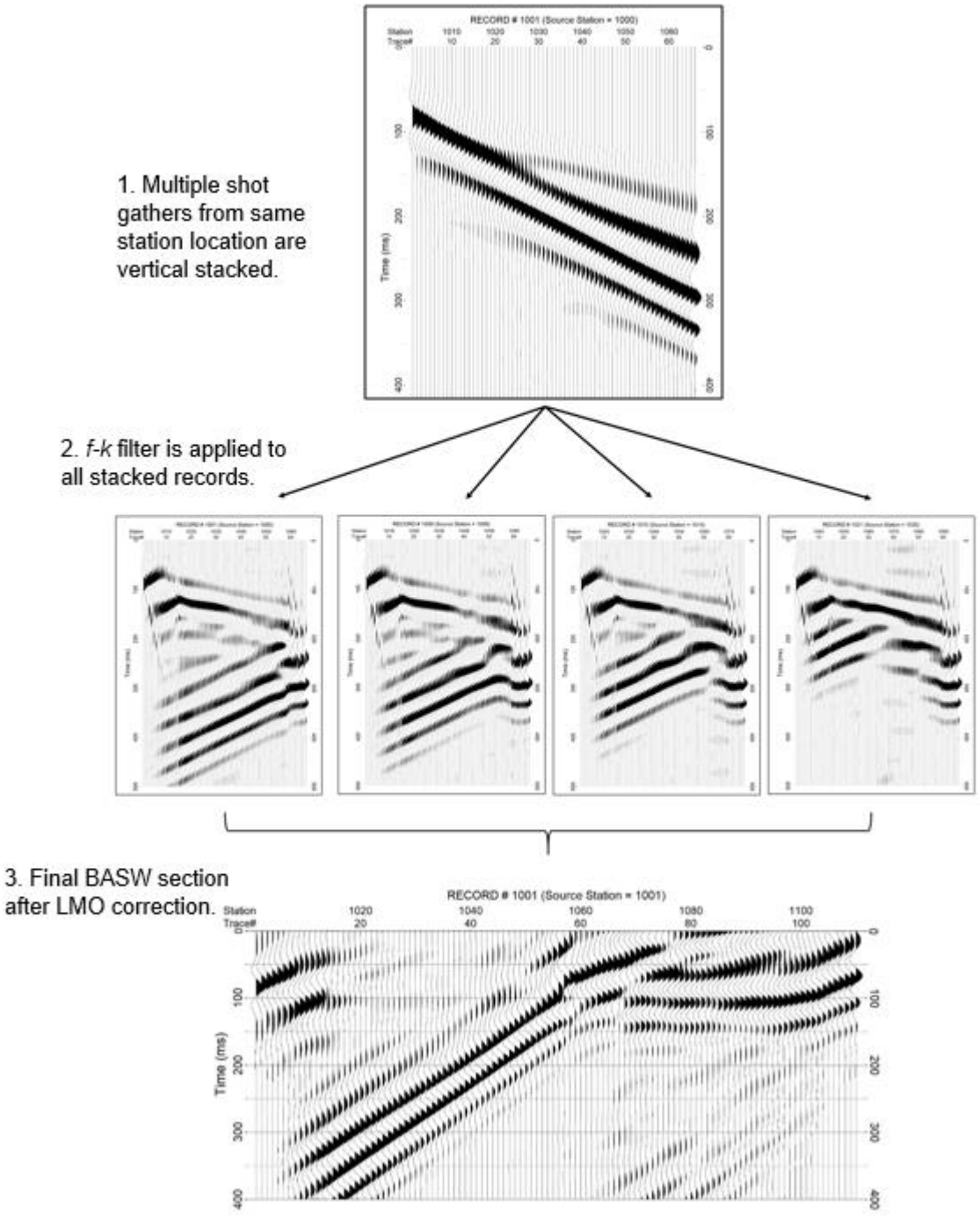

Figure 23. Simplified processing flow of BASW method using numerical data from this work.

Chapter 4: 3D Numerical Modeling

4.1. 3D model construction

Synthetic seismograms were generated to assess surface-wave behavior in a model setting as similar to the test site in Arizona as possible based on physical sampling and seismic measurements. A 3D, eight-layer model (**Table 4, Figure 24**) with a 1 x 1.5 m air-filled tunnel at approximately 10 m depth was produced using finite-difference elastic seismic modeling (**Table 5**); the 3D modeling code is an extension of the 2D work by Zeng et al. (2012). The laterally homogenous layered initial model was derived from previous field investigations (Schwenk, 2013). The source wavelet was the first derivative of the Gaussian function with a 15 Hz central frequency (**Table 6**), which provided high-amplitude surface wave information (3-62 Hz) with inverted depth exceeding 15 m. A fixed receiver spread crossed the tunnel located below station 1036 along a perpendicular orientation.

Table 4. Eight-layer numerical velocity model.

Layer	Depth (m)	Thickness (m)	Vs (m/s)	Vp (m/s)	Density (g/cm3)
1	3.5	3.5	325.0	645.20	1.4
2	5.0	1.5	375.0	744.46	1.5
3	6.0	1.0	480.0	952.92	1.6
4	10.5	4.5	460.0	913.21	1.7
5	21.0	10.5	575.0	1141.51	1.8
6	22.5	1.5	460.0	913.21	1.9
7	27.5	5.0	375.0	744.46	2.0
8	30.0	2.5	460.0	913.21	2.1

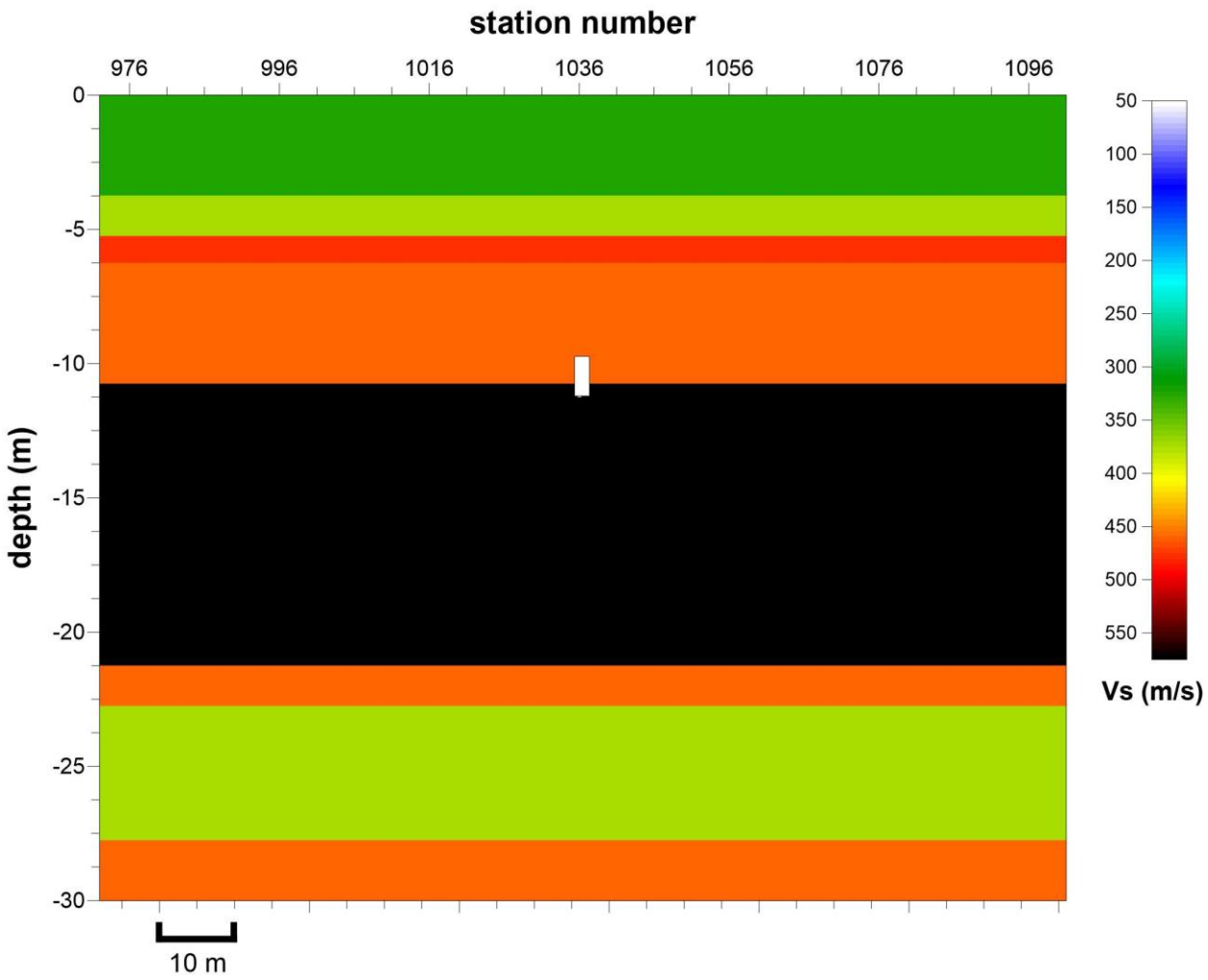

Figure 24. Numerically modeled velocity environment. The 10 m-deep tunnel location is indicated by the white box that is not drawn to scale.

Table 5. 3D Numerical model parameters.

Dimension (m) (x, y, z)	140, 30, 30
Grid spacing (m)	0.5
Number of receivers	66
Receiver spacing (m)	1
Source spacing (m)	1
Recording length (s)	2
Sampling interval (ms)	0.5

Table 6. Source wavelet parameters.

Source type	**Dip angle**	**Azimuth angle**
Vertical	90°	0°
Inline (H1)	90°	90°
Crossline (H2)	0°	90°

4.2. MASW Vs sections

Synthetic seismic data sets for vertical, longitudinal (H1), and transverse (H2) surface-wave motion were processed using the optimal 20 m rolling receiver spread with 6 m source offset determined from field testing. Each MASW Vs section (**Figure 25**) produced using the MASW method exhibited laterally heterogeneous velocities with a high-velocity layer below 5 m depth. An elevated velocity anomaly was also observed at station 1036 between 7-9 m depth in the vertical and H2 Vs sections and between 7-11 m depth in the H1 Vs section. This elevated velocity anomaly in the H1 Vs section extended from stations 1033-1038 (i.e., 5 m wide), compared to the 1 m wide anomaly in the vertical and H2 Vs sections. Inverted velocities obtained from each data set were within 10% of the true value for three of the five layers (**Figure 26**). The vertical data set under-estimated layers 2 and 3 by 13.8% and 17.7%, respectively. Layer 5, or the half space, was under-estimated by approximately 17.5% in the H1 and H2 numerical Vs sections (**Figure 25**). The H2 data set also under-estimated layer 3 by 15.7%. Overall, each Vs section was in good agreement where inverted velocities were within 20% of the true model (Xia et al., 1999b).

A sensitivity test was performed on each synthetic data set to analyze the relationship between the fundamental mode and depth with varying shear-wave velocity (**Figure 27**). Similar analyses by Xia et al. (1999a) and de Lucena and Taioli (2014) confirmed shear-wave velocity as the primary influence on Rayleigh-wave phase velocity when compared to density, layer thickness, and p-wave velocity. Therefore, the shear-wave velocity of each layer was increased by 25% within a 10-layer model derived from each data set; layer 9 contains the tunnel.

As expected, lower frequencies are sensitive to changes in deeper layers and higher frequencies are sensitive to changes in more shallow layers (**Figure 27**). Below 20 Hz in the

vertical data set (**Figure 27a**), fundamental-mode phase velocities changed by at least 12% in the deepest (10^{th}) layer, or half-space layer. Phase velocities also varied by approximately 6% in layer 9, the same layer as the tunnel, between 18-24 Hz and by 8% in layer 6 between 30-45 Hz. All other layers exhibited at least 1-5% change in phase velocity. In the H1 data set (**Figure 27b**), phase velocity estimates below 25 Hz also varied by at least 12% in the deepest layer. Below 55 Hz (**Figure 27b**), phase velocities varied up to 8% in layers 4-7. Lastly, phase velocity estimates below 11 Hz (**Figure 27c**) exhibited the greatest sensitivity to changes in Vs in the deepest layer while all remaining layers yielded less than a 5% change. Most notably, phase velocity estimates in layer 9 of the H2 data (**Figure 27c**) were the least affected (<2%) by the 25% change in Vs across the tested frequency range (5-70 Hz), even less than the first layer. Given this synthetically derived velocity structure, the vertical and H1 data sets (i.e., Rayleigh-wave data sets) were more sensitive to changes in Vs at frequencies below 55 Hz while the H2 data set (i.e., Love-wave data set) appeared more sensitive to frequencies higher than 55 Hz. This difference in layer sensitivity may be attributed to differing depth conversions used during Rayleigh-wave and Love-wave dispersion curve inversion. Rayleigh waves typically use a one-half wavelength inversion depth whereas Love waves use one-third the wavelength.

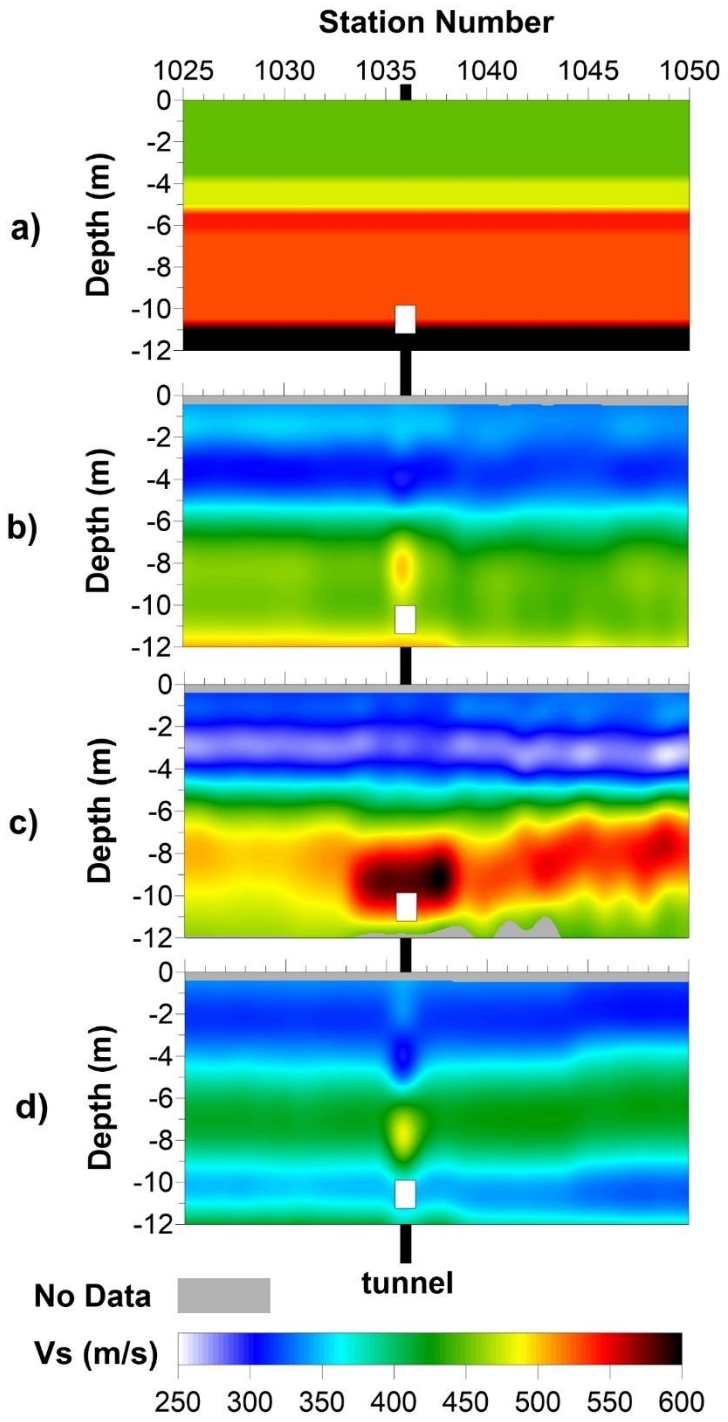

Figure 25. (a) Numerically modeled velocity environment and corresponding Vs MASW sections obtained using MASW processing from (b) vertical, (c) H1, and (d) H2 data sets. The tunnel is located below station 1036, indicated by the vertical black line and white box at approximately 10 m depth.

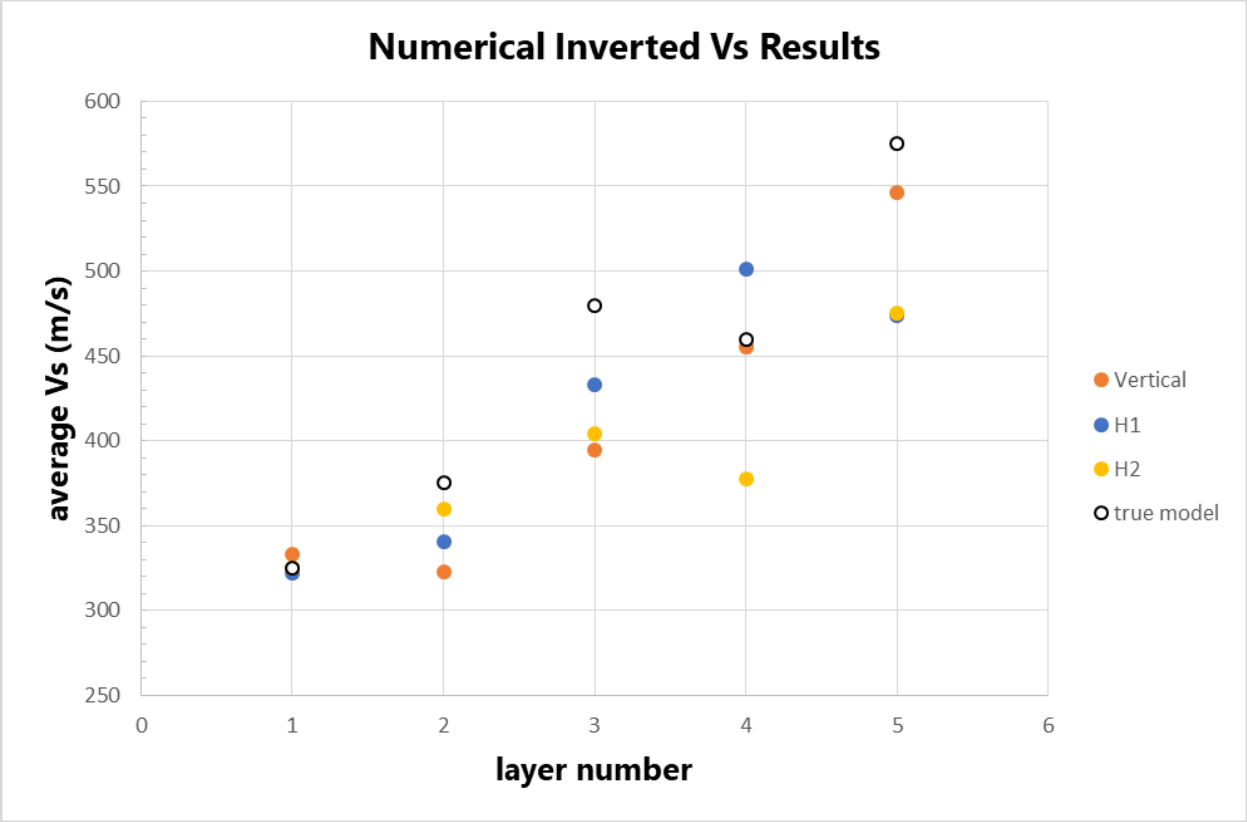

Figure 26. Inverted layer velocities of upper 12 m from numerical MASW Vs sections obtained using MASW processing compared to true layer model velocities (Table 4).

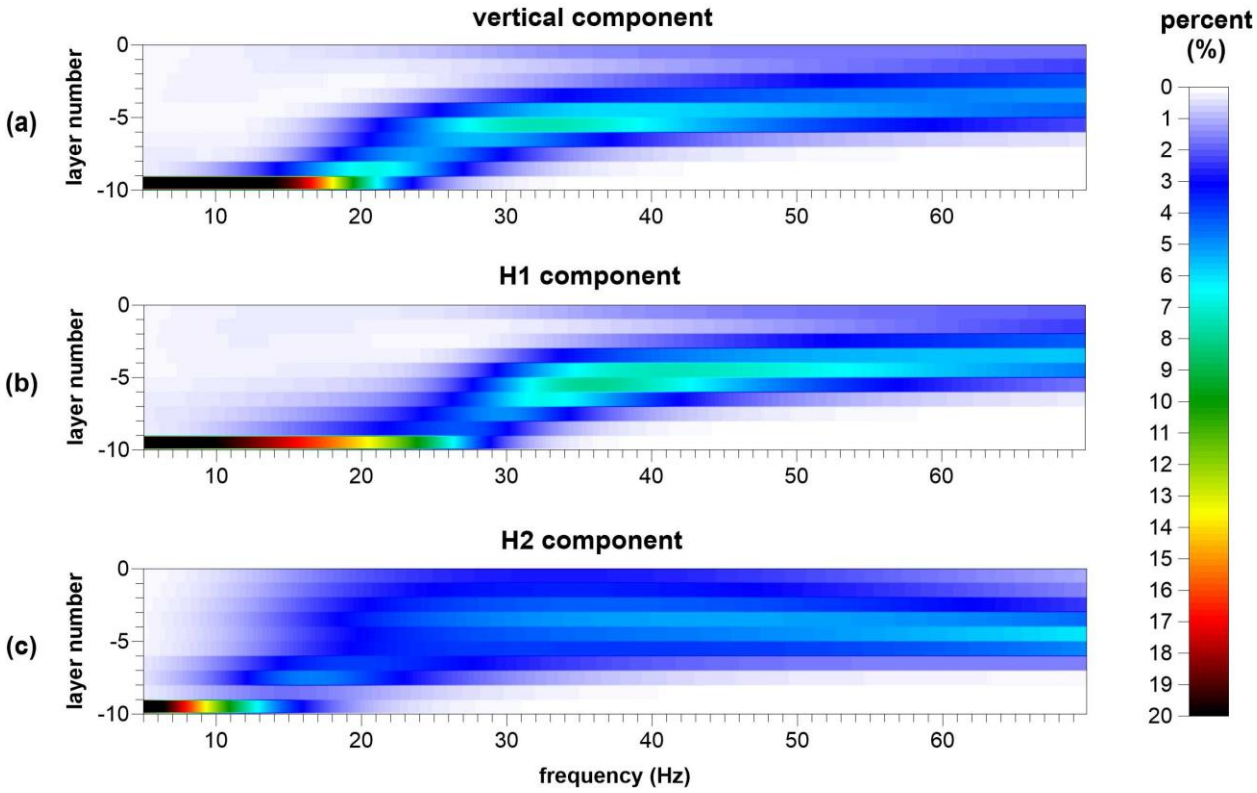

Figure 27. Sensitivity analysis of the numerical fundamental mode with 25% Vs variations in the (a) vertical, (b) H1, and (c) H2 data sets. The 10 m deep tunnel is in layer 9.

4.3. Backscatter Analysis

Backscatter analysis was performed on the three synthetic data sets to investigate back-propagating surface-wave behavior using a 65 m spread (66 receivers) to incorporate both short and long offset dispersion information. An *f-k* filter velocity was applied from 50-600 m/s to raw shot gathers to attenuate forward propagating surface waves and enhance the S/N of backscattered surface waves. LMO correction was attempted using different velocities (**Figure 28**) to determine the best-suited constant (i.e., single) velocity model that would accurately time-correct the backscatter apex to time-zero at the known station location of the tunnel (1036). Constant velocity models varied from 195 m/s to 315 m/s. Velocities 195 m/s, 215 m/s, and 250 m/s appear over time-corrected BASW sections such that the interpreted backscatter event shifted upwards and above time-zero (**Figure 28a-c**). When a 315 m/s constant velocity was applied, the interpreted backscatter event appeared under corrected with the backscatter apex observed below time-zero (**Figure 28e**). As a result, the 295 m/s constant velocity model more accurately shifted the backscatter apex to time-zero at the correct station location of the tunnel. The selected constant velocity model also represents the estimated velocity of the incident wave that backscattered off the tunnel at approximately station 1036.

BASW sections using a constant velocity model of 295 m/s (**Figure 29**) from each synthetic data set revealed a high-amplitude, backscatter originating within one receiver of station 1036 and extended more than 30 stations (i.e., 30 m). The high-amplitude backscatter in the vertical and H1 BASW sections possessed a 24 Hz signal, whereas the H2 BASW scatter exhibited a slightly lower frequency, 18 Hz. The constant velocity model used appeared to be more appropriate for the vertical and H1 data sets compared to the H2 data set. This is likely due to difference in propagation velocity for Rayleigh waves (vertical, H1) and Love waves (H2),

therefore the H2 data set may require a slightly different constant velocity model to more accurately apply the linear moveout correction. Overall, S/N ratio was highest in the vertical BASW section (**Figure 29a**) compared to the other sections, likely due to the difference in seismic energy generated by the weight drop source (vertical data) compared to the sledgehammer source (horizontal data sets). The time-corrected apex was also more easily discernable in the vertical and H1 BASW sections. In the H2 BASW section (**Figure 29c**), a high amplitude, but slightly lower frequency (~16 Hz) scatter event is observed left of stations 998 (between 25-175 ms). This 16 Hz scatter extends across higher stations (station 1033 or trace 55) where it overlaps with the scatter originating from approximately station 1036. A similar scatter is present below lower stations (stations 979-998) in the vertical and H1 BASW sections but appears less dominant in the section with an approximate 18 Hz frequency.

BASW sections from different component data sets were then combined to reduce background noise and enhance the backscatter event originating from the station above the tunnel. Trace amplitudes from two sections (i.e., data files) were combined using "record arithmetic" to add, subtract, multiply, or divide traces to improve S/N and enhance dominating backscatter features; only trace amplitudes having matching trace numbers are combined in this manner. For example, the amplitude of trace 2 in file 1 is added only to the amplitude of trace 2 in file 2. Using record arithmetic, high-amplitude scatters originating from stations left or right of tunnel station 1036 are still present after adding the vertical BASW section to the H1 BASW section (**Figure 30a**) due to constructively interfering signals. Minimal change to scatters was observed after subtracting the vertical and H1 BASW sections (**Figure 30b**). This implies that trace signal amplitudes are either higher in the vertical BASW section than the H1 BASW section or occur at slightly different times. Interestingly, amplitudes of scatters originating from

stations left and right of the tunnel station are greatly reduced after the vertical and H1 BASW sections are multiplied (**Figure 30c**) with a dominant scatter event remaining. This dominant scatter originates from approximately station 1036.

Dividing the vertical BASW section by the H1 BASW section (**Figure 30d)** proved to be the least successful record arithmetic operator. Signal amplitudes were significantly reduced across all traces in the resulting BASW section (**Figure 30d**). An additional high-cut filter from 0-70 Hz was applied to divided BASW sections to enhance possible scatter events. Without normalizing traces, the additional high cut filter did not appear to alter trace signals in neither the V/H1 BASW section (**Figure 31a**) or the H1/V BASW sections (**Figure 31c**). When traces were normalized, signal amplitudes presented in the V/H1 BASW section with a faint linear trend originating from station 1036 and extending left through lower stations (**Figure 31b**). No coherent backscatter trend was observed in the normalized H1/V BASW section (**Figure 31d**). Overall, dividing the Rayleigh wave components (i.e., the vertical and H1 components) did not prove to be an effective means for enhancing a backscatter event associated with the tunnel at station 1036.

The same record arithmetic was performed to combine the H1 and H2 BASW sections (**Figure 32** and **Figure 33**). Subtracting the H1 and H2 BASW sections (**Figure 32b**) resulted in a combined BASW section with higher-amplitude and a more coherent, continuous backscatter signature compared to the other arithmetic operators; note traces in **Figure 32** are not normalized, with all sections have a 4 dB trace amplitude applied. A high-cut filter (0-70 Hz) was applied to the divided horizontal BASW sections to retrieve backscatter signals, but such a signature was not observed unless traces were normalized (**Figure 33**). This effect and result are consistent with dividing the vertical and H1 sections (**Figure 31**). In the H1/H2 BASW section

with trace normalization, a relatively continuous linear backscatter event was observed originating from approximately station 1036 in **Figure 33b**. This trend was not observed in the H2/H1 BASW section (**Figure 33d**) implying greater backscattering energy contribution from the H1 component compared to the H2 component.

Background noise was successfully minimized and attenuated by multiplying the vertical and H1 BASW sections (**Figure 34a** and **Figure 34c**) as well as both horizontal (H1 and H2) BASW sections (**Figure 34b**). As a result, the backscatter event originating from approximately station 1036 was enhanced despite the phase change observed in the H1-H2 section (**Figure 34b** and **Figure 34d**). This phase change is likely the result of the H1 data set (Rayleigh wave) and H2 data set (Love waves) having different frequency content due to the different propagation characteristics for Rayleigh waves and Love waves. The vertical-H1 BASW section exhibited a more subtle phase change since the multiplied data sets both contain Rayleigh wave phase information. This phase information is shown in Figure 34 where the frequency content of the dominant backscatter event possesses a 24 Hz peak frequency in both the H1 and H2 BASW sections (**Figure 35a-b**). It is important to note that multiplying BASW sections multiplies the traces in time domain and results in a combined section with a higher dominant frequency (**Figure 35c**). Sloan et al., (2016) has demonstrated that the frequency of backscattered events may be used to estimate the depth of the scattering feature. Although multiplying sections appears to enhance the backscatter signature, this record arithmetic also affects the frequency content of corresponding signals, and therefore that dominant frequency should not be used to estimate target depth.

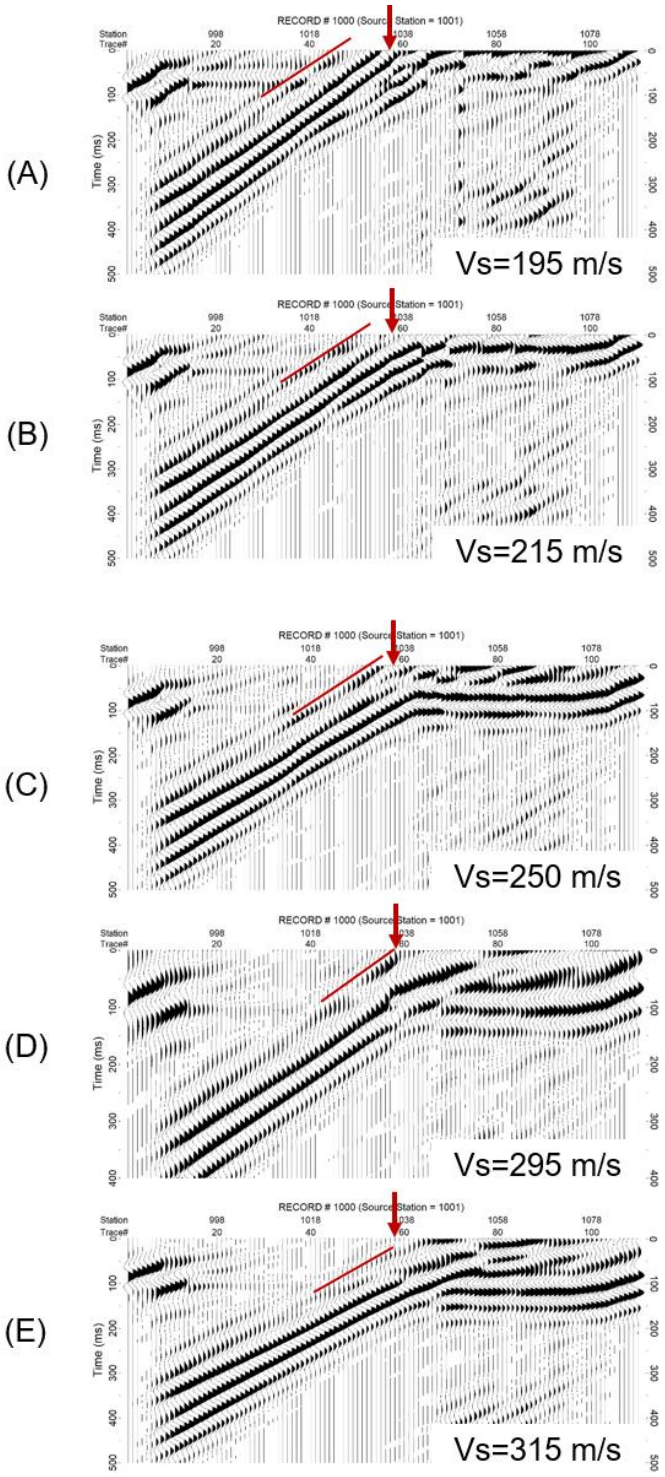

Figure 28. BASW sections from vertical synthetic data set after applying LMO correction velocities (a) 195 m/s, (b) 215 m/s, (c) 250 m/s, (d) 295 m/s, and (e) 315 m/s. The red arrow indicates the station location of the tunnel at 1036, the red oblique line is the interpreted backscatter.

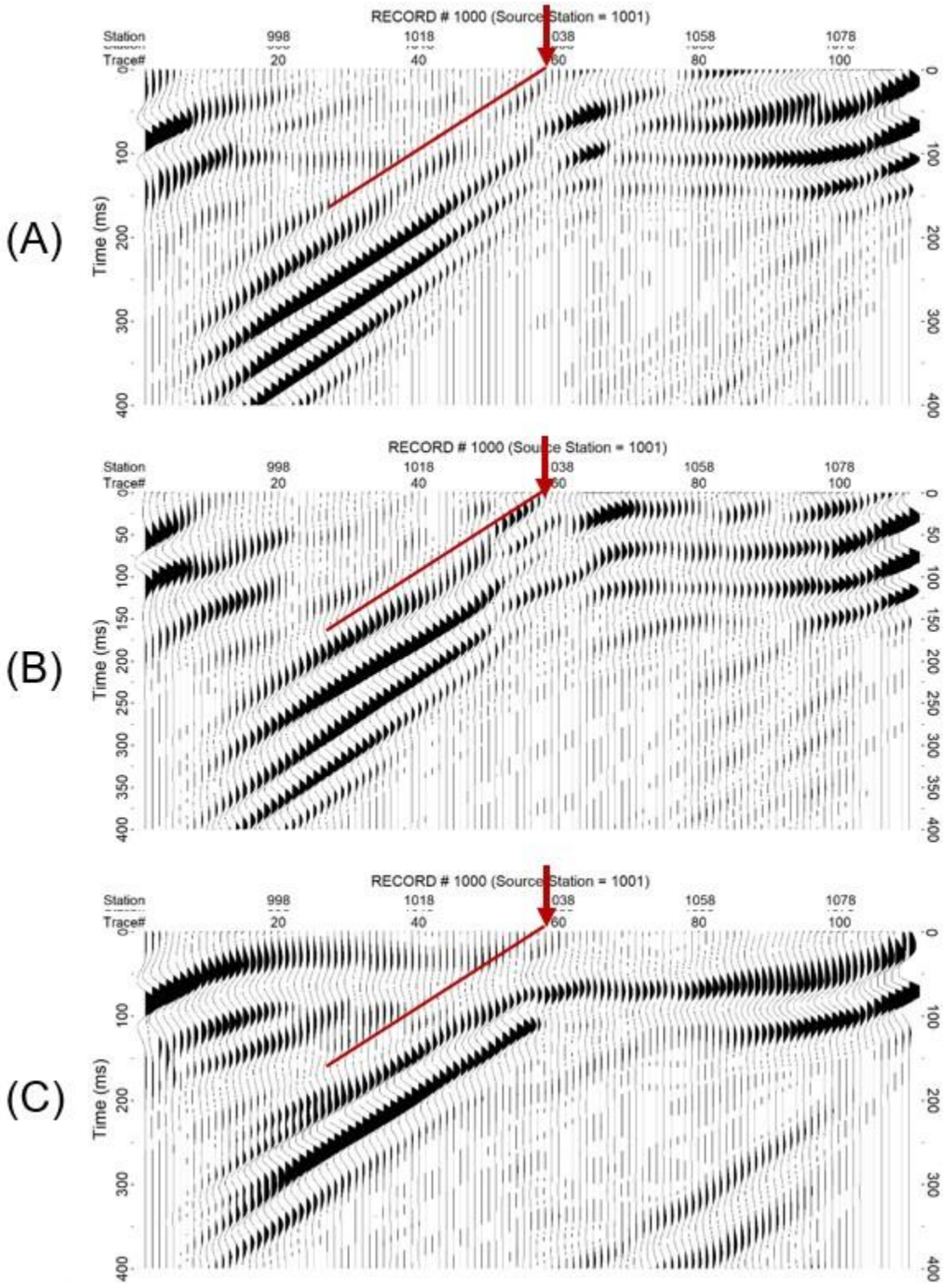

Figure 29. BASW sections from (a) vertical, (b) H1, and (c) H2 data sets; tunnel is located below station 1036 (red arrow) and the red oblique line is the interpreted backscatter.

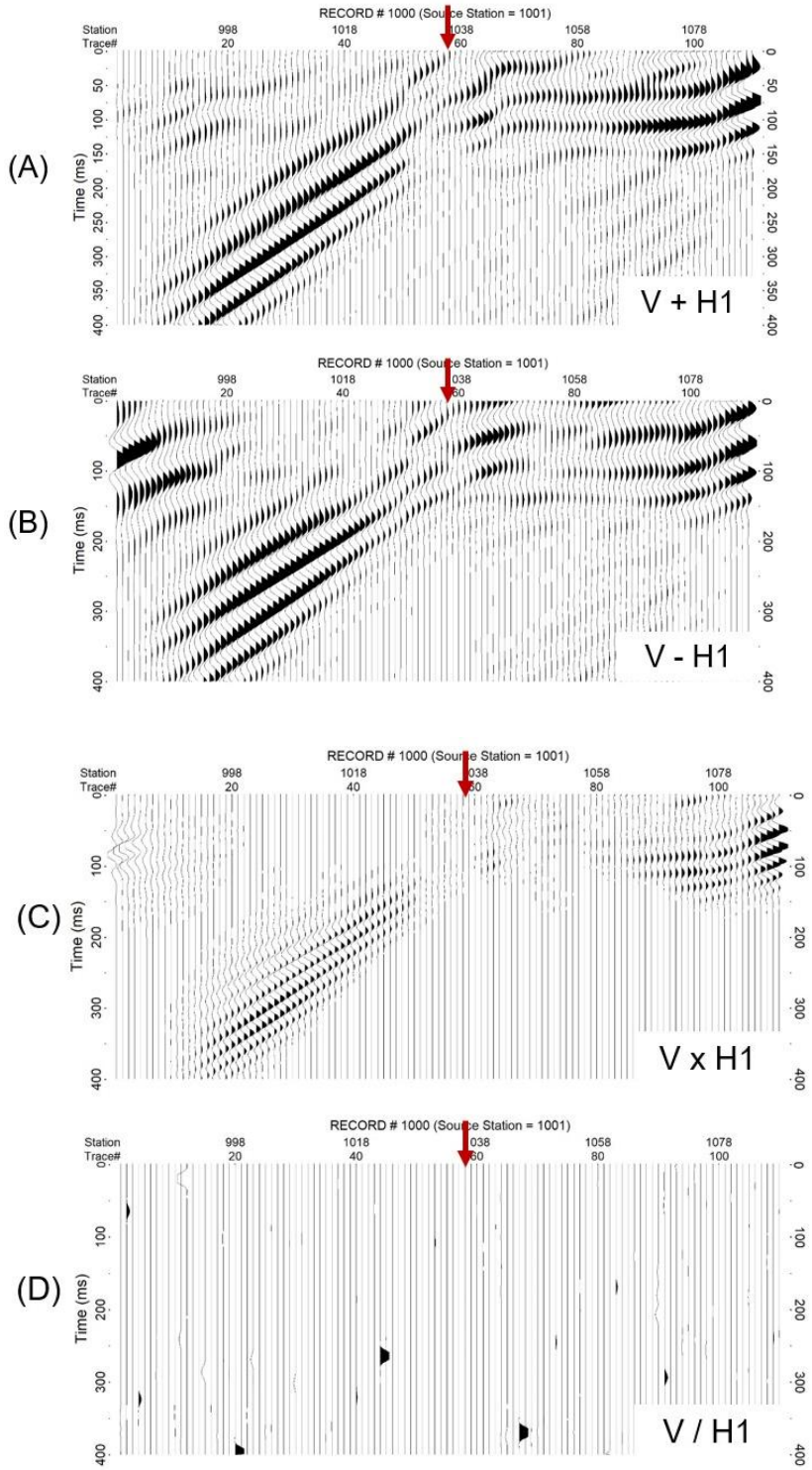

Figure 30. Combined vertical and H1 BASW sections using record arithmetic without trace normalization. (a) V plus H1, (b) V minus H1, (c) V multiplied by H1, and (d) V divided by H1.

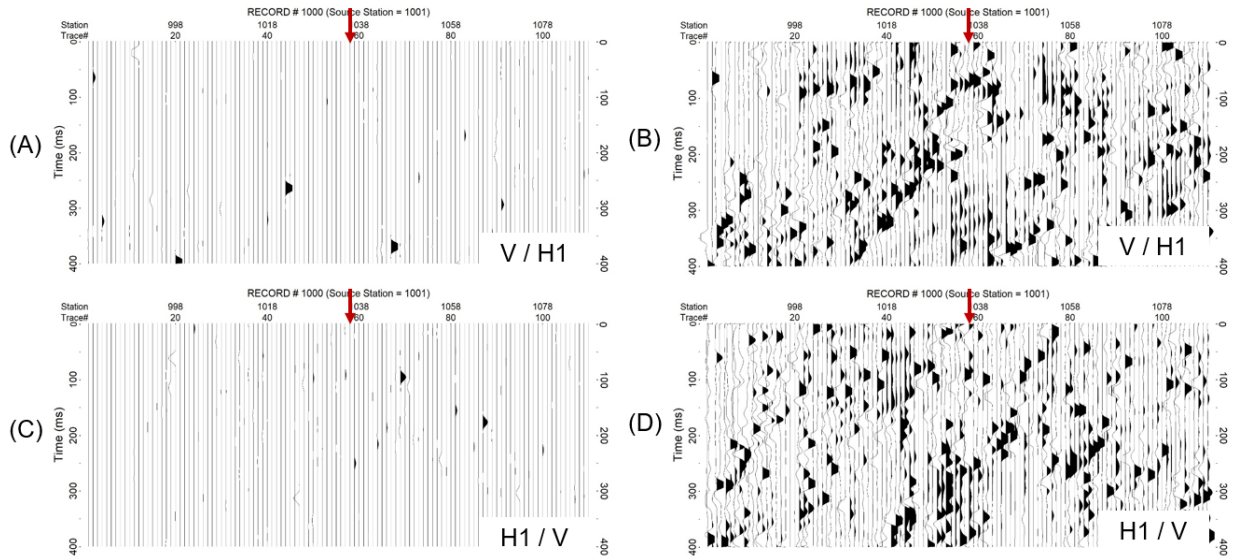

Figure 31. Vertical divided by H1 BASW section after high cut filter applied from 0-70 Hz (a) without and (b) with trace normalization. (c) H1 divided by vertical BASW section after high cut filter applied from 0-70 Hz (c) without and (d) with trace normalization. Red arrow indicates station location of tunnel, 1036.

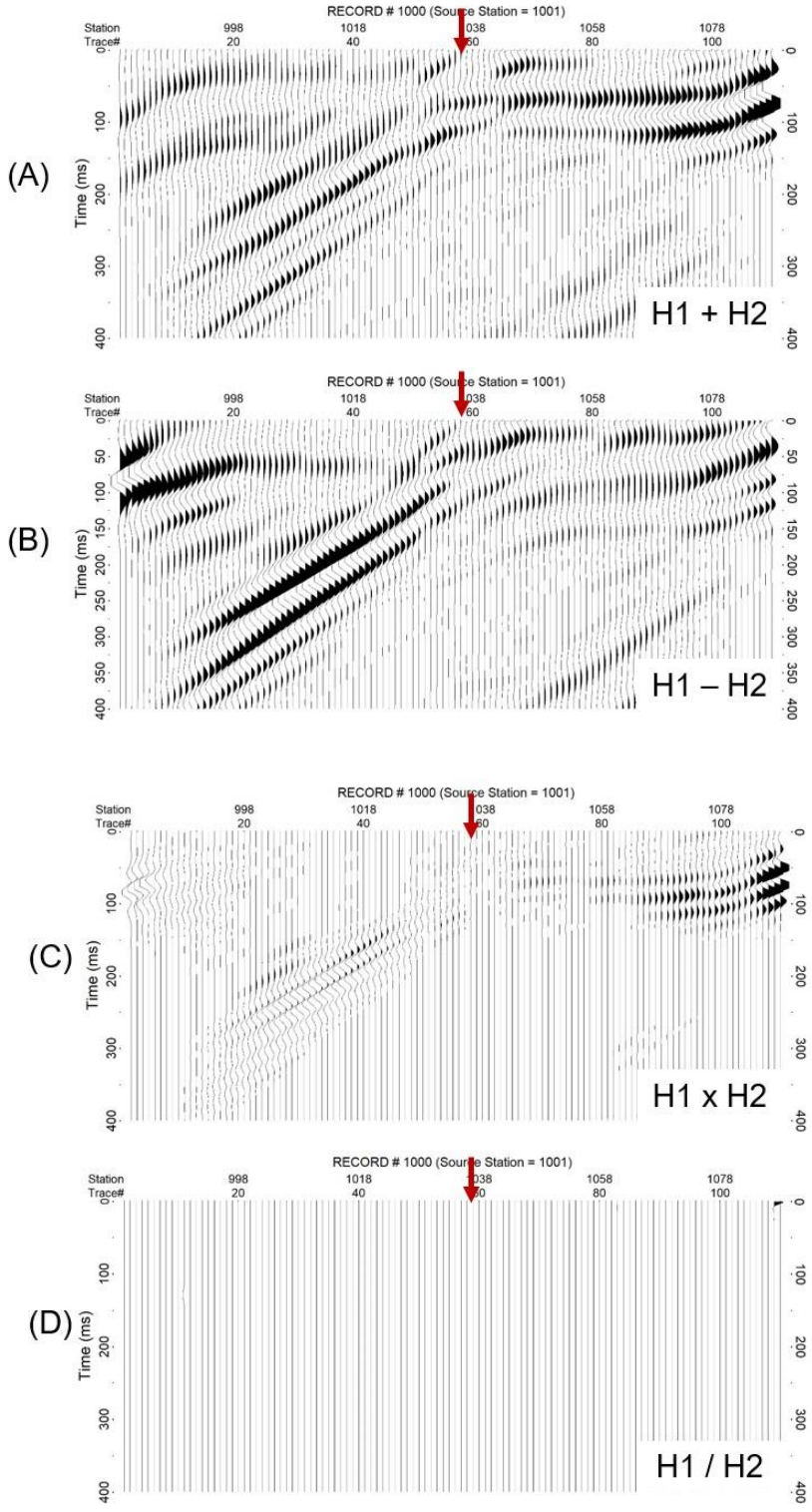

Figure 32. Combined H1 and H2 BASW sections using record arithmetic without trace normalization. (a) H1 plus H2, (b) H1 minus H2, (c) H1 multiplied by H2, and (d) H1 divided by H2.

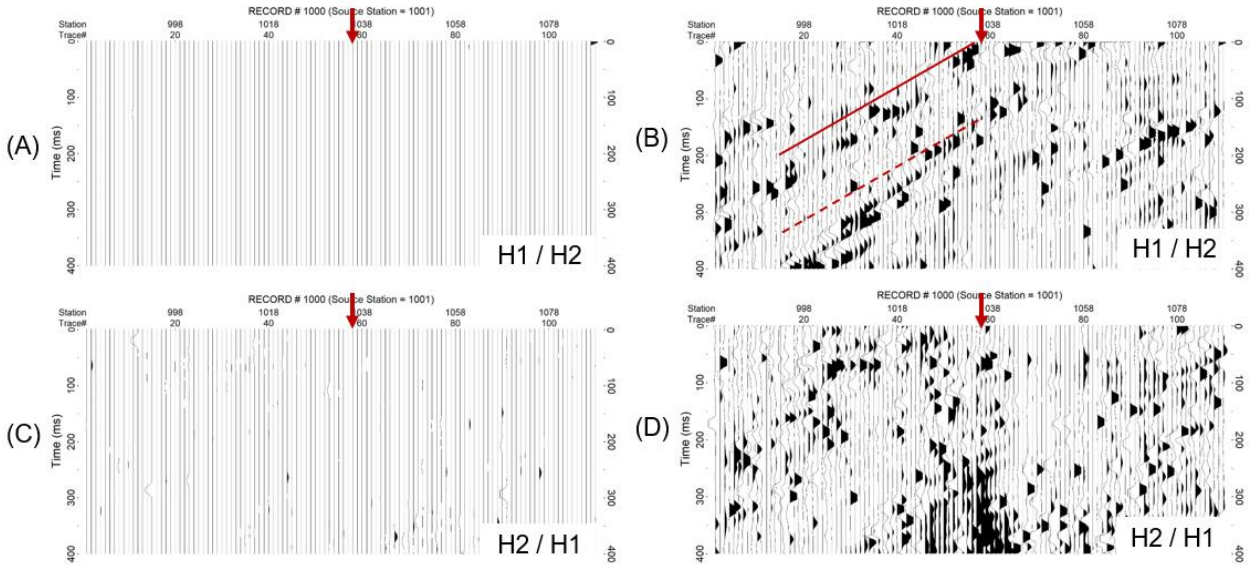

Figure 33. H1 divided by H2 BASW section after high cut filter applied from 0-70 Hz (a) without and (b) with trace normalization. (c) H2 divided by H1 BASW section after high-cut filter applied from 0-70 Hz (c) without and (d) with trace normalization. Red arrow indicates station location of tunnel, 1036. Solid red line traces the interpreted backscatter event with the dashed red line tracing the same backscatter event, but later in time.

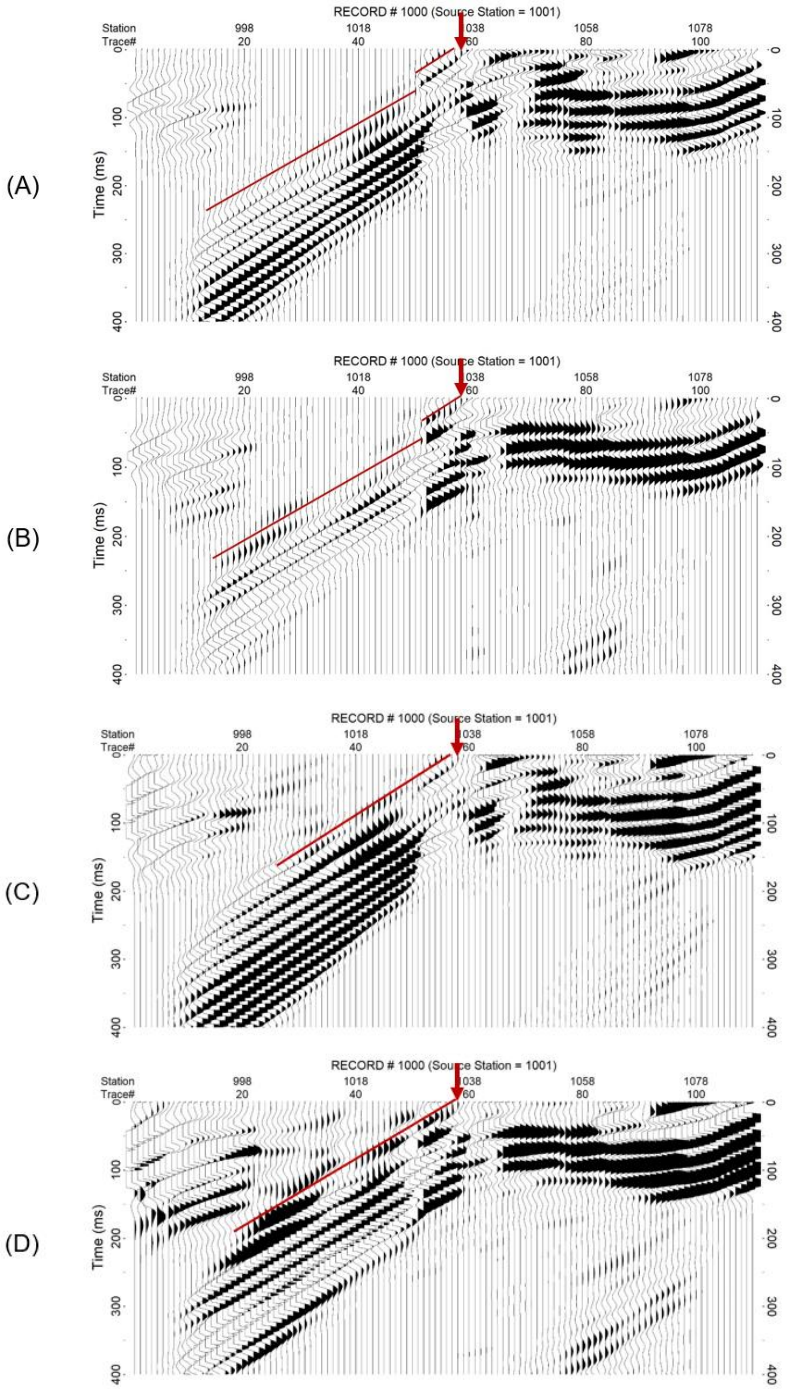

Figure 34. Multiplied BASW sections from (a) the vertical and H1 normalized data sets and (b) H1 and H2 normalized numerical data sets, (c) un-normalized vertical and H1 data sets (28 dB), and (d) un-normalized H1 and H2 data sets (33 dB). The enhanced the backscatter feature originates from approximately station 1036 (red arrow) and is traced with a red line in each section.

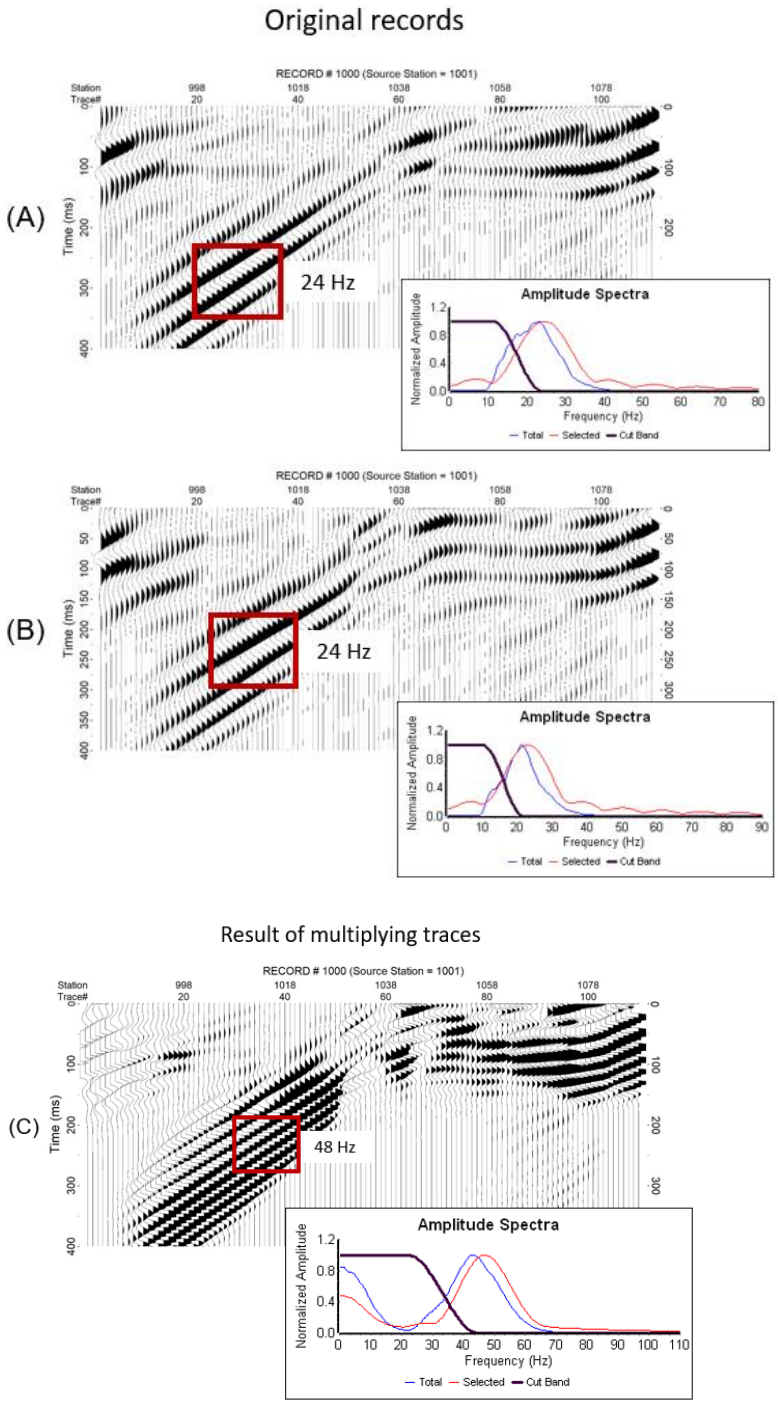

Figure 35. Individual (a) V and (b) H1 BASW sections exhibited scatter events with a 24 Hz center frequency. (c) When the V and H1 BASW sections were multiplied, the scatter event exhibited a 48 Hz center frequency.

Chapter 5: Field Data Results

5.1. MASW Vs sections

5.1.1. Full length 65 m spread

MASW Vs sections were produced using vertical, H1, and H2 data sets collected at the tunnel test site. The conventional (i.e., vertical component source and receivers) MASW method using the full 65 m long spread and 1 m source offset (**Figure 36a**) yielded a MASW Vs section with velocity conditions that supported the known geologic conditions at this site; known velocity conditions (**Figure 37**) include a high velocity (500-600 m/s) layer at a depth of 10-15 m, overlying lower velocity (200-400 m/s) materials (Schwenk, 2013) which were previously discussed in Chapter 3. However, no evidence of the tunnel was observed below station 1036 at 10 m depth, the known tunnel location. The MASW Vs section shown in **Figure 36b** using horizontal (inline/longitudinal) geophones and a longitudinal-oriented source (H1) demonstrates a velocity structure similar to **Figure 36a**, but the high-velocity layer observed at 10 m on the MASW Vs section obtained from the vertical data set is approximately 5 m deeper than expected.

Remarkably, the H1 data set revealed a disturbance in the high-velocity layer between 10-15 m displayed as a stress arching between stations 1030-1040 (**Figure 36b**). The shape of this velocity anomaly is similar to elevated stress features seen in salt-dissolution studies (Ivanov et al., 2013; Sloan et al., 2009) or the halo effect noted in other void studies (James, 2013; Llopis et al., 2005; Schwenk et al., 2016). However, these cases only discuss the use of the vertical component of the Rayleigh wave, not the horizontal Rayleigh wave component. The H2 MASW

Vs section in **Figure 36c** surprisingly did not produce a result that was indicative of the known conditions, nor was a tunnel signature observed.

Surface-wave data recorded in 2016 produced Vs profiles from MASW processing generally consistent with the expected geologic conditions of this environment. Compared to 2011 shear-wave downhole surveys conducted in two boreholes, however, inverted shear-wave velocities from the 2016 ground surveys were 30-50% higher in the upper 5 m (**Figure 38**). Velocities from depths 0-9 m in borehole FT7 were not recorded. It is also important to note that boreholes FT13 and FT7 are not within the immediate vicinity of the seismic surveys and the exact location of these boreholes was not disclosed to the student processing the seismic data. The potentially large distance between the location of the ground seismic surveys and downhole seismic surveys likely contributes to the variation in recorded velocities.

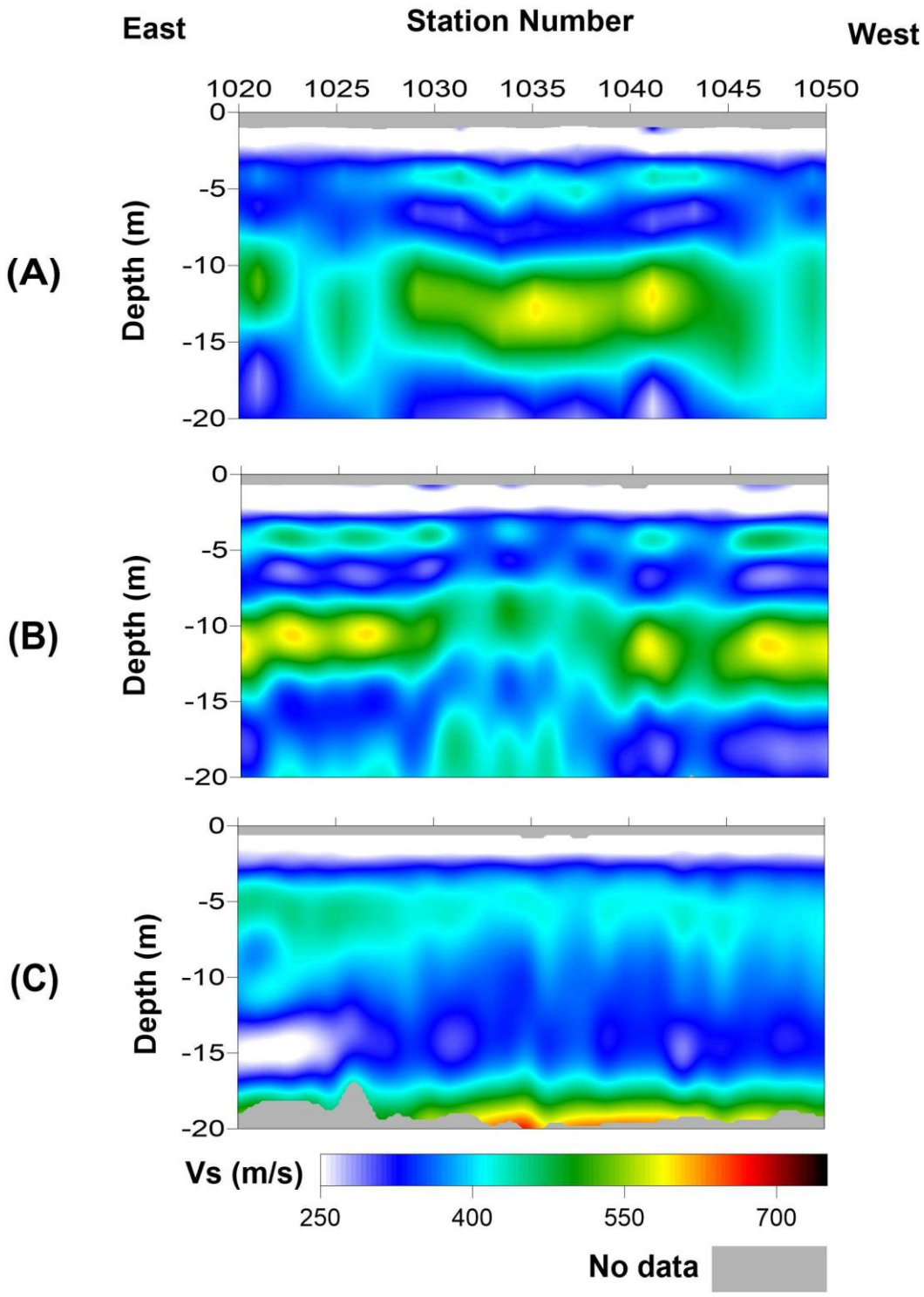

Figure 36. MASW Vs profiles from (a) vertical, (b) H1, and (c) H2 data sets using a 65 m spread length. The location of the tunnel is below station and 10 m depth.

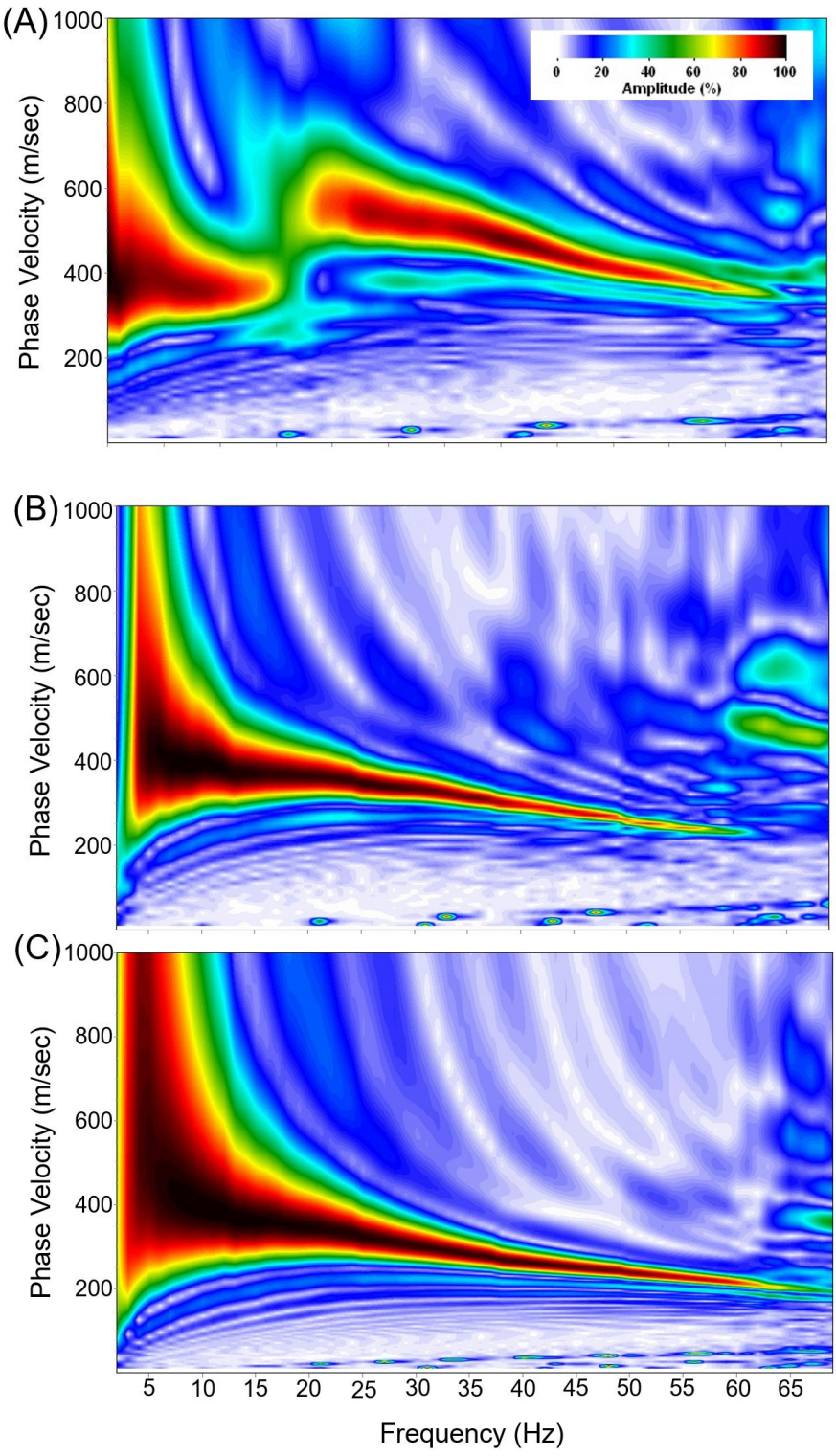

Figure 37. Raw dispersion images from the 65 m spread corresponding to the (a) vertical, (b) H1, and (c) H2 data sets; modified from Morton et al. (2017).

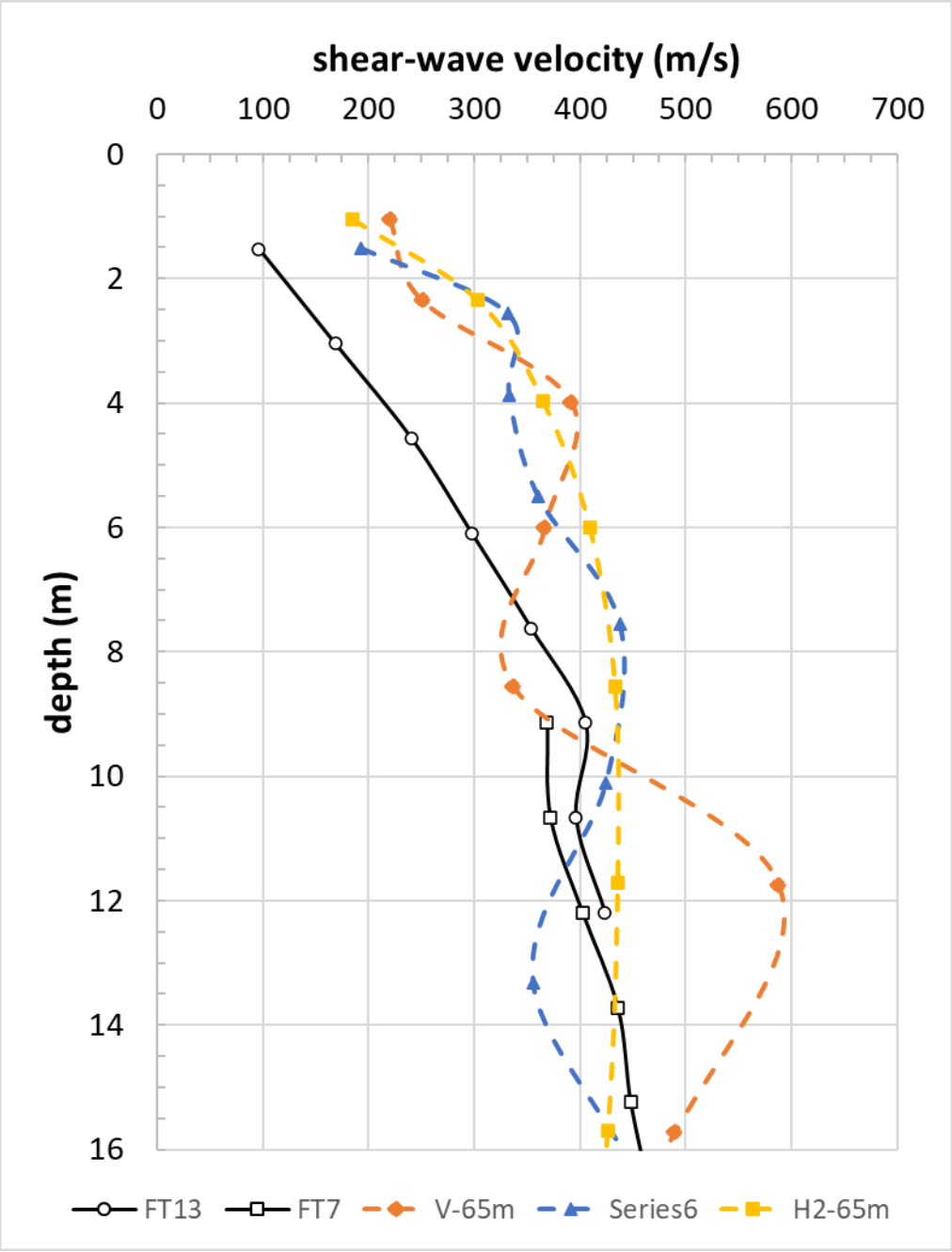

Figure 38. The 1D Vs profiles from MASW processing of each data set from mid-station 1036 using a 65 m spread size with respect to downhole shear-wave velocity estimations in well FT13 and well FT7 from Rickards (2011).

5.1.2. Optimal 20 m spread

As discussed in Chapter 3, a 20 m spread length was chosen as the optimal spread size for imaging a known 10 m-deep tunnel within the upper 12 m of the subsurface and optimizing vertical resolution of the final image. The broad frequency range of the fundamental mode (i.e., 11-65 Hz) provided adequate wavelengths for sampling the upper 12 m (**Figure 39**). This outcome was obtained using the three data sets despite dominant higher modes observed in the dispersion-curve images from the vertical data set.

A sensitivity test was performed on each data set to analyze the relationship between the fundamental mode and depth with varying shear-wave velocity (**Figure 40**). Similar analyses by Xia et al. (1999a) and de Lucena and Taioli (2014) confirmed shear-wave velocity as the primary influence on Rayleigh-wave phase velocity when compared to density, layer thickness, and p-wave velocity. Therefore, the shear-wave velocity of each layer was increased by 25% within a 10-layer model derived from each data set; layer 9 contains the tunnel. As expected, lower frequencies are sensitive to changes in deeper layers and higher frequencies are sensitive to changes in more shallow layers (**Figure 40**). Below 17 Hz in the vertical data set (**Figure 40a**), fundamental-mode phase velocities changed by at least 12% in the deepest layer. Phase velocities also varied by 9% in layer 4 between 30-40 Hz with at least 4-5% for all other layers. The fundamental-mode phase velocities in the H1 data set (**Figure 40b**) exhibited a similar 12% change with a 25% change in Vs in the deepest layer. Above 45 Hz, phase velocity varied by more than 10% the third and fourth layers. Finally, phase velocities in the H2 data set showed greater sensitivity to Vs variations in first four layers (**Figure 39c**).

Given this velocity structure, the vertical and H1 data sets (i.e., Rayleigh wave data sets) were more sensitive to changes in Vs at greater depth while the H2 data set (i.e., Love wave data

set) was more sensitive to the shallow layers. This difference in layer sensitivity may be attributed to differing depth conversions used during Rayleigh-wave and Love-wave dispersion curve inversion. Rayleigh waves typically use a one-half wavelength inversion depth whereas Love waves use one-third the wavelength.

The relative shear-wave velocities displayed in the MASW Vs section derived from inverted vertical-component Rayleigh waves (**Figure 41a**) were consistent with the geologic conditions expected for this environment. A higher Vs layer (400-450 m/s) consistent with gravel materials in logs was observed (**Figure 41a**) between 5-10 m depth. Dispersion-curve picks in the frequency domain were limited throughout portions of the seismic line to frequencies between 12-35 Hz (**Figure 39a**) due to a dominant higher mode that obscured the fundamental mode. To better enhance the fundamental mode, the higher mode trend was suppressed by defining a filter with a bow-slice shaped reject zone in the *f-k* domain (Park et al., 2002; Morton et al., 2015). As a result, the higher mode was adequately suppressed, but the higher frequency range of the fundamental mode was not completely recovered. Instead, the filtered dataset was used as reference for picking the fundamental mode using the original data set. Fundamental mode dispersion curves were picked with high confidence from approximately 11 to 65 Hz despite the discontinuous, high-frequency trend observed in data from some stations.

A subtle increase in velocity was observed in the MASW Vs section above the tunnel at 7-9 m depth (**Figure 41a**) that extended laterally from stations 1036-1039. Dispersion curves corresponding to this station range also exhibited a phase-velocity inversion between 21-25 Hz (**Figure 39a**). Outside this station range, dispersion curves were picked consistently throughout the seismic line with a downward, high-amplitude trend between 11-30 Hz (400-300 m/s). This downward trend was followed by a linear high-frequency trend to 65 Hz with phase velocities

from 300-250 m/s. After reviewing each 1D Vs result, it was determined that this elevated velocity anomaly below 7 m depth is likely related to the tunnel rather than an inversion instability or a poorly picked dispersion curve.

The Rayleigh-wave dispersion curves produced using the H1 data set possess a sharp and coherent fundamental-mode trend for each shot gather (**Figure 39b**). Higher modes had no adverse effect on the high-amplitude fundamental mode below 60 Hz. Therefore, dispersion curves were picked from 11.5-65 Hz with a gentle, downward trend from 11.5 to 20 Hz (375-330 m/s) becoming horizontal or asymptotic across 20-30 Hz (330-300 m/s) and downward again through higher frequencies (**Figure 39b**). The resulting MASW Vs section yielded laterally homogenous velocities with a high-velocity layer at approximately 5 m depth. However, no anomaly could be interpreted within the velocity field at the tunnel location below receiver station 1036 at approximately 10 m depth (**Figure 41b**).

High-resolution Love-wave dispersion curves (**Figure 39c**) were produced using the H2 data set with a coherent fundamental mode evident across a wide frequency range (i.e., 11.5-65 Hz). These well-defined fundamental modes with a continuous downward pattern from 370-200 m/s had no visible interference effects from higher modes below 70 Hz (**Figure 39c**). The resulting MASW Vs section (**Figure 41c**) exhibited a high-velocity layer (400 m/s) from 4-8 m depth, with an arch-shaped velocity anomaly from station 1034-1041 (i.e., 7 m wide). This velocity anomaly is seven times wider than the width of the tunnel and would normally be overlooked without additional information that could be incorporated to provide a more precise horizontal location for the tunnel.

In general, data recorded with each surface-wave component produced Vs profiles from MASW processing generally consistent with the expected geologic conditions of this

environment and previous downhole surveys in boreholes FT13 and FT7 (**Figure 42**). Vertical and H1 1D Vs profiles started at 2.5 m depth to be consistent with the sensitivity analysis. The varied velocities reported in the upper 7 m are likely the result of surface processes (e.g., wind and precipitation) known to affect the density of these unlithified materials. Below 7 m, shear-wave velocities from the vertical Vs profile were within 3% of values from the downhole survey whereas Vs from the H1 and H2 Vs profiles yielded a greater difference of 20%. Xia et al. (2002) identified MASW velocities to be reliable when values are within 15% of borehole velocity estimations. The vertical data set yielded velocities more accurate than the H1 and H2 data sets based on this classification. Boaga et al. (2013) observed that vertical and horizontal surface-wave components at lower frequencies are influenced by higher modes differently in environments with a high-velocity contrast such as this surveyed area. It is possible a higher mode may overlap and mask the fundamental mode below 20 Hz since the vertical data set included an interfering higher mode at higher frequencies (**Figure 39a**). The fundamental mode remained uninterrupted in the H1 (**Figure 39b**) and H2 (**Figure 39c**) data sets with high S/N ratio throughout a broad frequency range.

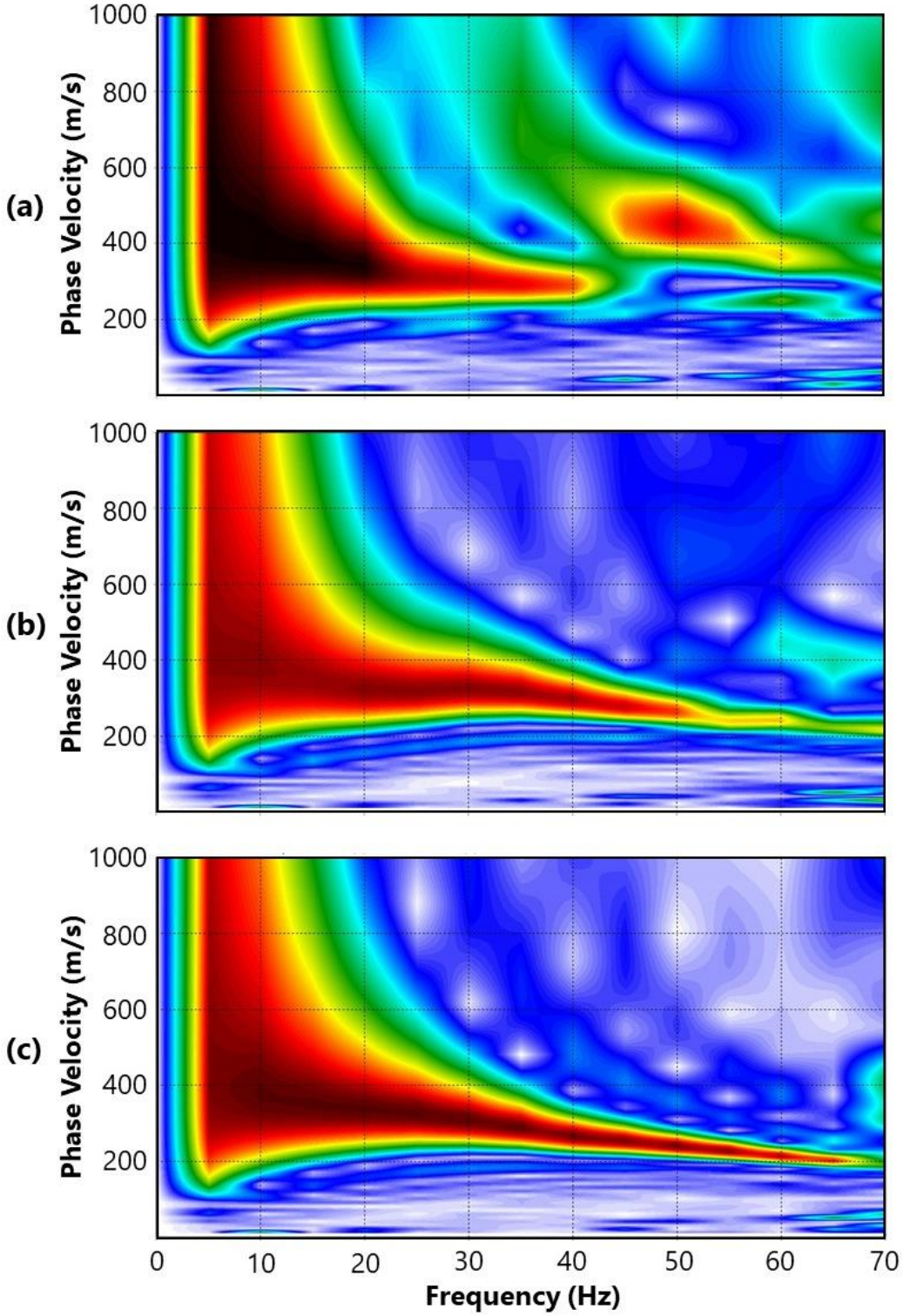

Figure 39. Raw dispersion-curve images from mid-station 1036 with respect to the (a) vertical, (b) H1, and (c) H2 data sets.

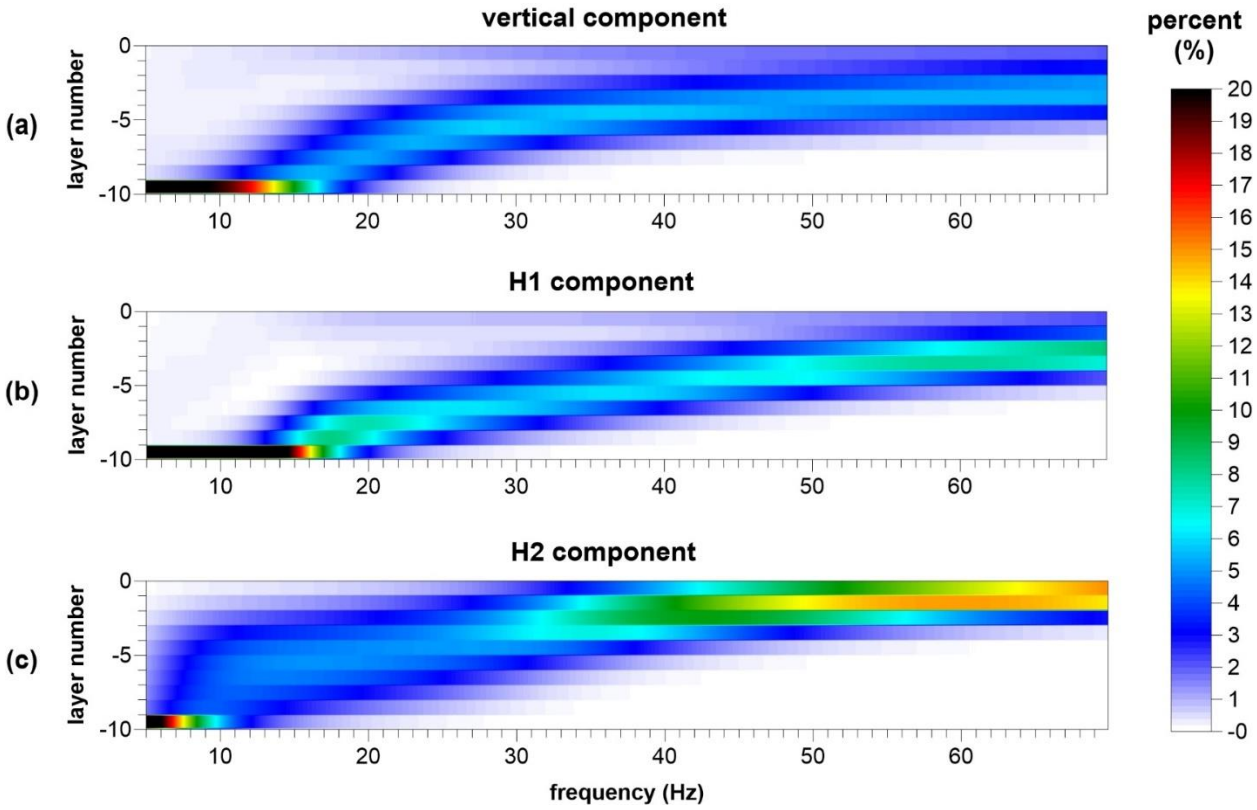

Figure 40. Sensitivity analysis of the fundamental mode with 25% Vs variations in the (a) vertical, (b) H1, and (c) H2 data sets. The 10 m deep tunnel is located in layer 9.

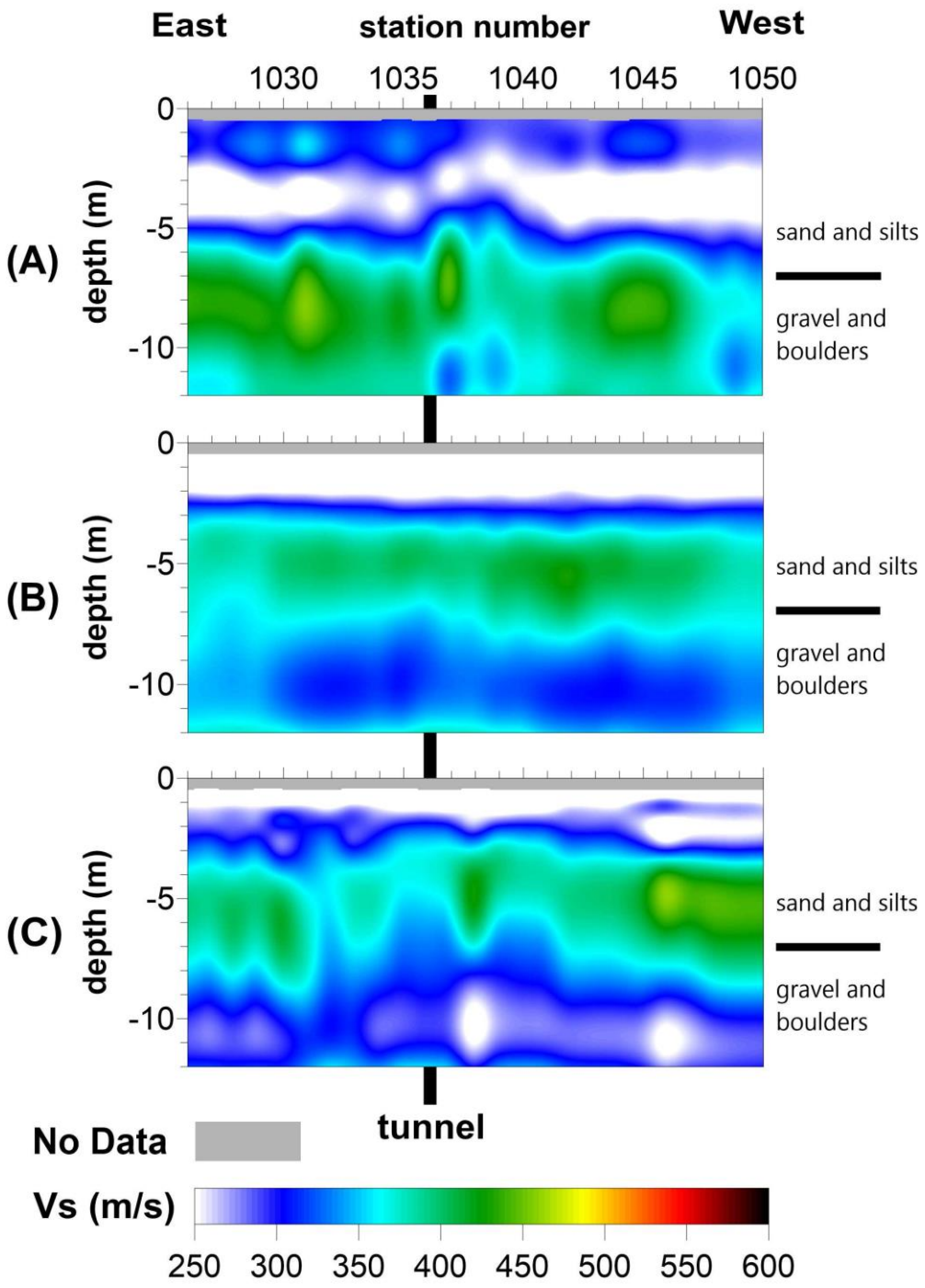

Figure 41. MASW Vs profiles from (a) vertical, (b) H1, and (c) H2 data sets using a 20 m spread length. The location of the tunnel is indicated by the vertical black line at station 1036.

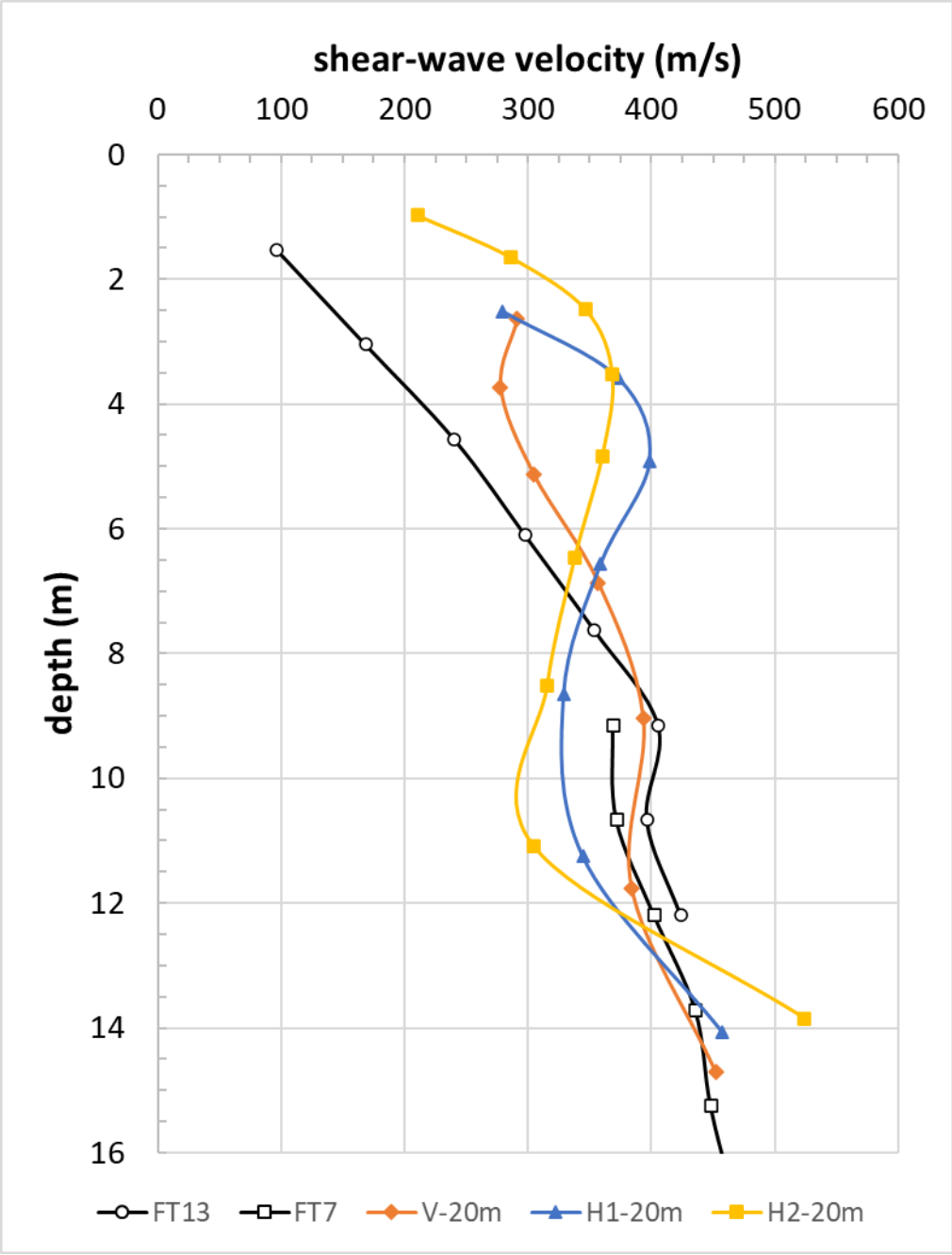

Figure 42. The 1D Vs profiles from MASW processing of each data set and mid-station 1036 using a 20 m spread size with respect to downhole shear-wave velocity estimations in wells FT13 and FT7 from Rickards (2011).

5.2. Backscatter analysis

BASW processing was performed using shot records with a 65 m spread to include wavelength information from both short and long offsets (i.e., short surface-wave wavelengths and long surface-wave wavelengths). An *f-k* filter was applied to attenuate forward-propagating surface waves and then an LMO correction with a constant velocity model (**Table 7**). The selected LMO correction velocities were determined using trial and error where velocities ranged from 275 m/s to 350 m/s; this was demonstrated with the numerical testing in Chapter 4. The LMO correction velocities listed in **Table 7** represent those that accurately shifted the backscatter event associated with the tunnel to time-zero. Constant velocity models (LMO correction velocities) that were too slow under corrected the backscatter apex (i.e., shifted apex later in time) and velocities too fast over corrected the backscatter apex (i.e., shifted apex earlier in time and above time-zero).

Table 7. BASW processing parameters.

Surface-wave data set	*f-k* filter (Hz)	LMO correction (m/s)
Vertical	30-365	300
H1	50-325	300
H2	50-325	290

On the vertical BASW section (**Figure 43a**), surface-wave backscatter originated from receiver station 1037, within 1 m of the horizontal tunnel location and extends more than 25 traces. The overall signal-to-noise is somewhat low and may be due to factors such as wind during acquisition (e.g., 10-15 mph gusts listed in the observer's notes) or destructive stacking due to uncertainty in the velocity function and errant moveout corrections. These data were reprocessed (**Figure 43b**) using a dispersion-curve velocity model from each MASW data set to

reduce the number of scatters in the final vertical BASW section. The slope of the backscatter is slightly steeper in **Figure 43b** because velocities in the dispersion-curve velocity model are higher than the constant velocity model used to generate the section in **Figure 43a**. Even though the number of backscatter events in **Figure 43b** decreased by at least half, too many remain to confidently select the one associated with the tunnel without bias.

The H1 BASW section (**Figure 44a**) possessed a high-amplitude linear trend originating from station 1036; backscatter apex is plus or minus one station. This dominant, continuous feature was interpreted with high confidence as backscatter off the west side of the tunnel and consistent with a subsurface object disturbing the native material. At least two other backscatters were observed starting from stations 1012 and 1060, but these trends were less coherent and became discontinuous after a few traces. The presence of multiple scatters is not surprising given the documented heterogeneity (e.g., gravel vs. boulders) in this geologic setting. Nonetheless, backscatter originating from approximately 1036 exhibits a continuous trend and higher amplitude than other events.

In the H2 BASW section (**Figure 44b**), a backscatter was observed from below stations 1035-1060. This back-propagating trend represents the longest continuous feature evident in the section that possessed similar spatial characteristics as the tunnel (i.e., the apex of the scatter is within one station of the tunnel). Both the H1 and H2 results included a high-amplitude, linear trend across the same station range and minimal interference to the dominant trend.

Overall, a backscatter was observed in each of the three BASW sections originating from station 1036 at time-zero. Low S/N ratio in the vertical BASW section (**Figure 43**) led to reduced confidence when selecting a single backscatter related to the tunnel. To improve S/N ratio, the vertical and H1 BASW sections were multiplied resulting in an enhanced Rayleigh-

wave BASW section (**Figure 45a**). Although not immediately obvious, the longest linear feature in this combined section was observed below 1036 and extended beyond station 1060. This feature was traced to time-zero, but signal amplitudes decreased greatly after the first four traces. The H1 and H2 BASW sections were also combined to attenuate all other scatters and a high-amplitude, continuous trend was revealed from stations 1037-1061 (**Figure 45b**). Signal deteriorated on two traces between stations 1037-1040 but did not detract from the ease of interpreting the overall trend that originated within one station of the true location of the tunnel (i.e., station 1036). A high level of accuracy is required for tunnel detection and combining the H1 and H2 sections provided greater certainty in selecting station 1036 as a candidate for the tunnel location (**Figure 45b**). Numerical analysis discussed in Chapter 4 supports this interpretation where this observed backscatter event is expected for a tunnel of this size and depth in this geologic setting.

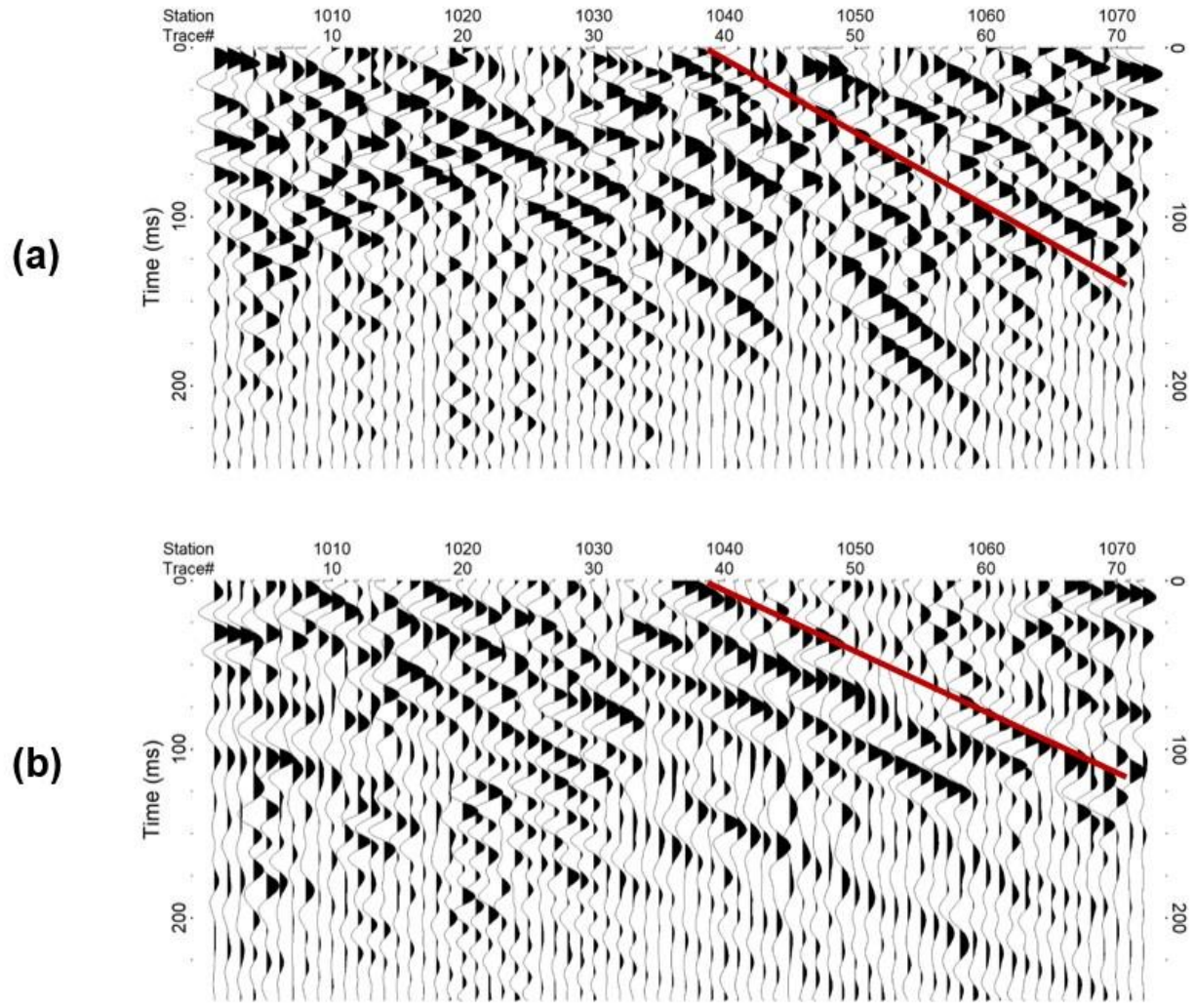

Figure 43. BASW sections from the vertical data set using (a) a 300 m/s constant velocity model and (b) a dispersion-curve velocity model. The backscatter is traced with a red line in each section.

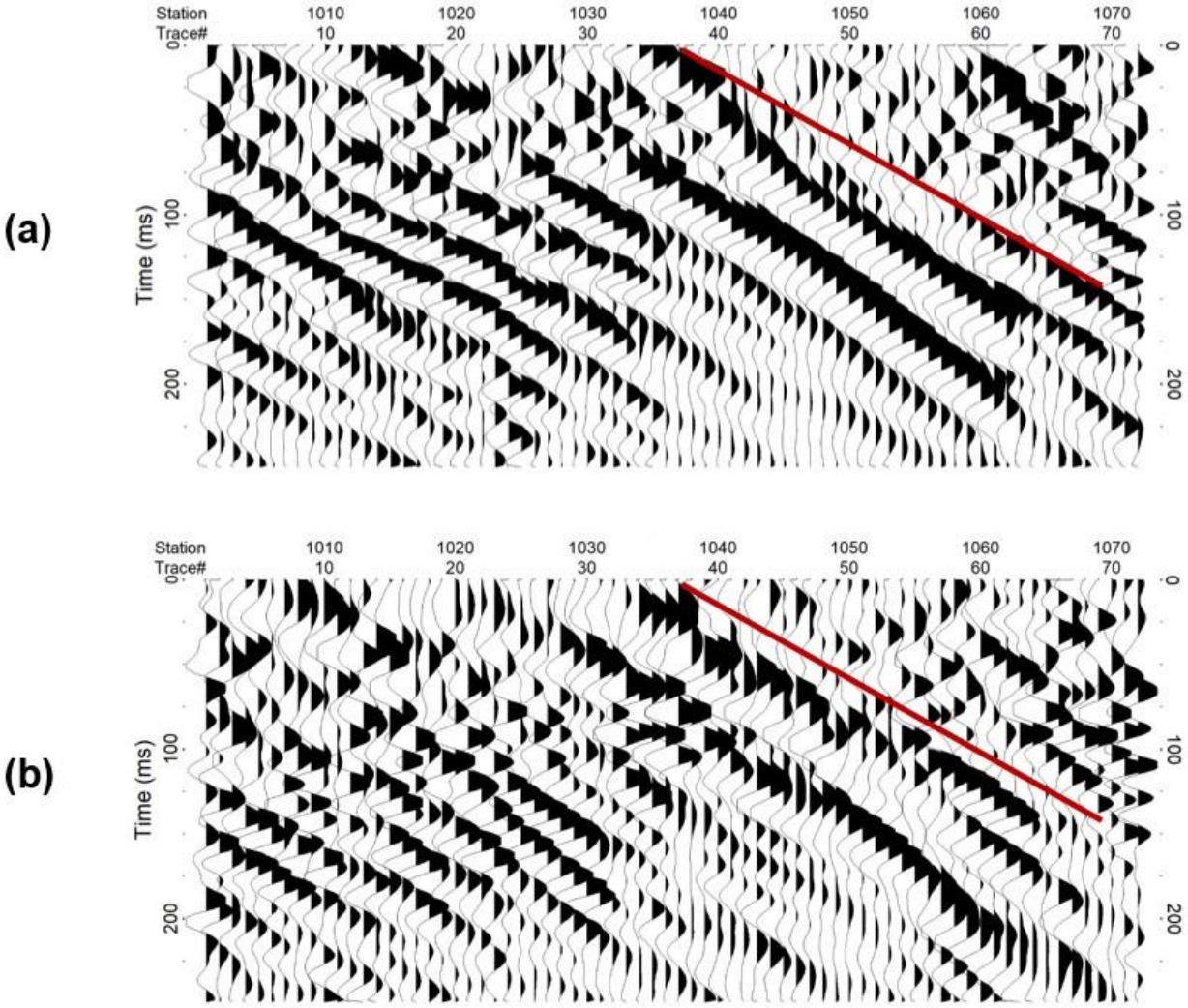

Figure 44. BASW sections from the (a) H1 and (b) H2 data sets. The backscatter is traced with a red line in each section.

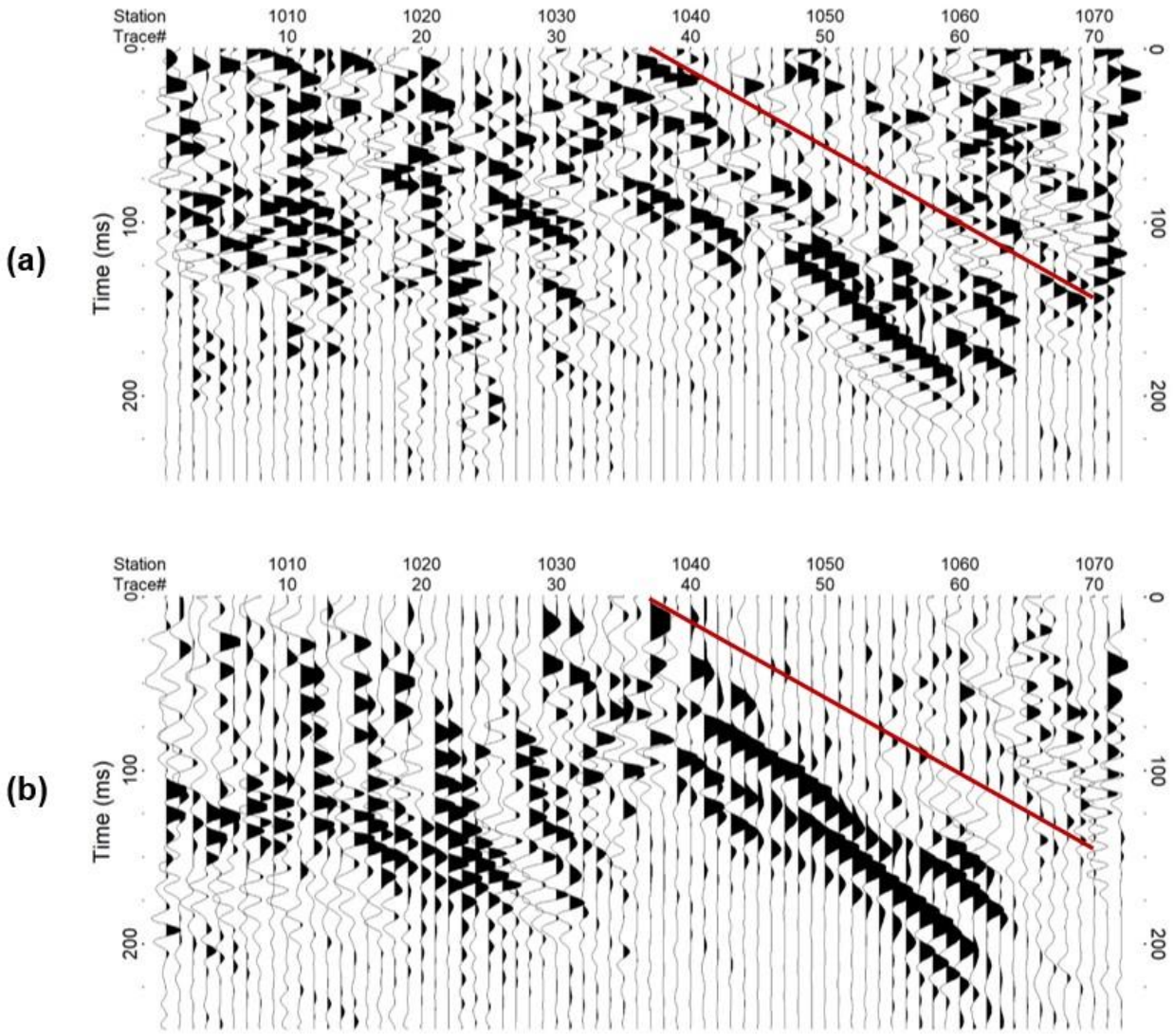

Figure 45. BASW sections from the (a) combined vertical and H1 data sets and (b) the combined H1 and H2 data sets. The backscatter is traced with a red line in each section.

Chapter 6: Discussion

Surface-wave analysis is inherently controlled by the shortest and longest available wavelengths in each data set. Successful recording of desired wavelengths is influenced by the acquisition parameters as well as mechanical and geometric properties of the surveyed environment (Socco and Strobbia, 2003; Socco et al., 2010). An early study of these 2016 data sets from the Yuma Proving Ground (Morton et al., 2017) used a 65 m spread to retrieve surface-wave information for reaching a 25 m depth of investigation. However, MASW Vs sections using the longer spread did not display a clear disturbance from the tunnel in the surface-wave wavefield. Given the small size of the tunnel relative to the longer spread size, and therefore longer wavelengths, any indication of the tunnel was likely smeared due to the large sampling volume (Zhang et al., 2004; Xia et al., 2004; Ivanov et al., 2006; Mi et al., 2017).

For data analysis in this research project, the 20 m optimal receiver spread and 6 m source offset was selected to improve vertical and lateral resolution of the Vs inverted result. For this analysis workflow a velocity anomaly consistent with station location of the tunnel was successfully resolved in the vertical and H2 MASW Vs sections. The lack of a tunnel anomaly in the H1 Vs section may be attributed to vertical and horizontal components of Rayleigh waves having different wave energy amplitudes (Dal Moro and Ferigo, 2011; Ikeda et al., 2015). Theoretically, the vertical and H1 data sets should yield similar phase velocities, but this is not the case for data sets acquired in this geologic setting. Another factor for the difference in vertical and H1 velocities may be that the H1 component, while assumed to be Rayleigh wave energy, could have some contributions from Love wave motion that have affected the velocity estimations. Instead, phase velocities in the vertical data set are 5% higher than phase velocities

in H1 and H2 data sets below 20 Hz (**Figure 46**). From 25-40 Hz, the vertical data set phase velocities are approximately 10% lower than the H1 data set and 5% lower than the H2 data set (**Figure 46**). According to the literature, the H2 data set or Love-wave data set, should yield velocities approximately 10% higher than Rayleigh-wave components, but that does not appear to be the case in this research study. These decreased H2 velocities may be the result of anisotropy in this depositional environment, although that cannot be more confidently assessed without data from a line oriented perpendicular to the current survey. The vertical data set was also the only data set that contained multiple coherent modes. Based on these observations, it is possible that vertical phase velocities are being affected by higher-mode interference at lower frequencies where the fundamental mode energy peak is broad (**Figure 39a**) compared to the H1 and H2 data sets (**Figure 39b** and **Figure 39c**). Boaga et al. (2013) observed that phase velocity energy can shift from the fundamental mode to first higher mode with a smooth, continuous transition in environments with a strong velocity contrast. This mode misidentification often leads to an overestimation of the corresponding layers.

Interestingly, the vertical and H2 MASW Vs sections display a disturbance in the surface-wave wavefield (**Figure 41a, Figure 41c**) not observed in an earlier study of these data sets (Morton et al., 2017). The lack of a tunnel anomaly in the H1 MASW Vs section may be attributed to vertical and horizontal particle motions of Rayleigh waves having different amplitudes (Dal Moro and Ferigo, 2011).

Even with the velocity anomaly observed in both the vertical and H2 MASW Vs sections, additional information is required to accurately locate the tunnel. Before this 3C study, backscatter analysis had only been performed using vertical component surface-wave data. As a result, a backscatter event was observed in each of the three BASW sections that extended from

stations 1036 to 1060, an approximately 24 m wide feature (**Figure 43** and **Figure 44**). Numerical analysis suggests that this backscatter event is consistent with a tunnel of this size and depth in this modeled geologic setting. To improve signal-to-noise ratio, the H1 and H2 sections were multiplied and therefore combined to produce a significantly enhanced backscatter signature corresponding to the tunnel (**Figure 45b**). All other scatters were attenuated and a high-amplitude, continuous trend was revealed from stations 1037-1061 (i.e., 24 m) in the combined section. Signal deteriorated on two traces within station range 1037 to 1040 but did not detract from the ease of interpreting the overall trend that originated within one station of the true location of the tunnel (i.e., station 1036). A high level of accuracy is required for tunnel detection and the use of not only multi-component backscatter sections (**Figure 44**) and combining multiple sections (**Figure 45**) significantly reduced uncertainty associated with non-tunnel scatters observed on the individual BASW sections.

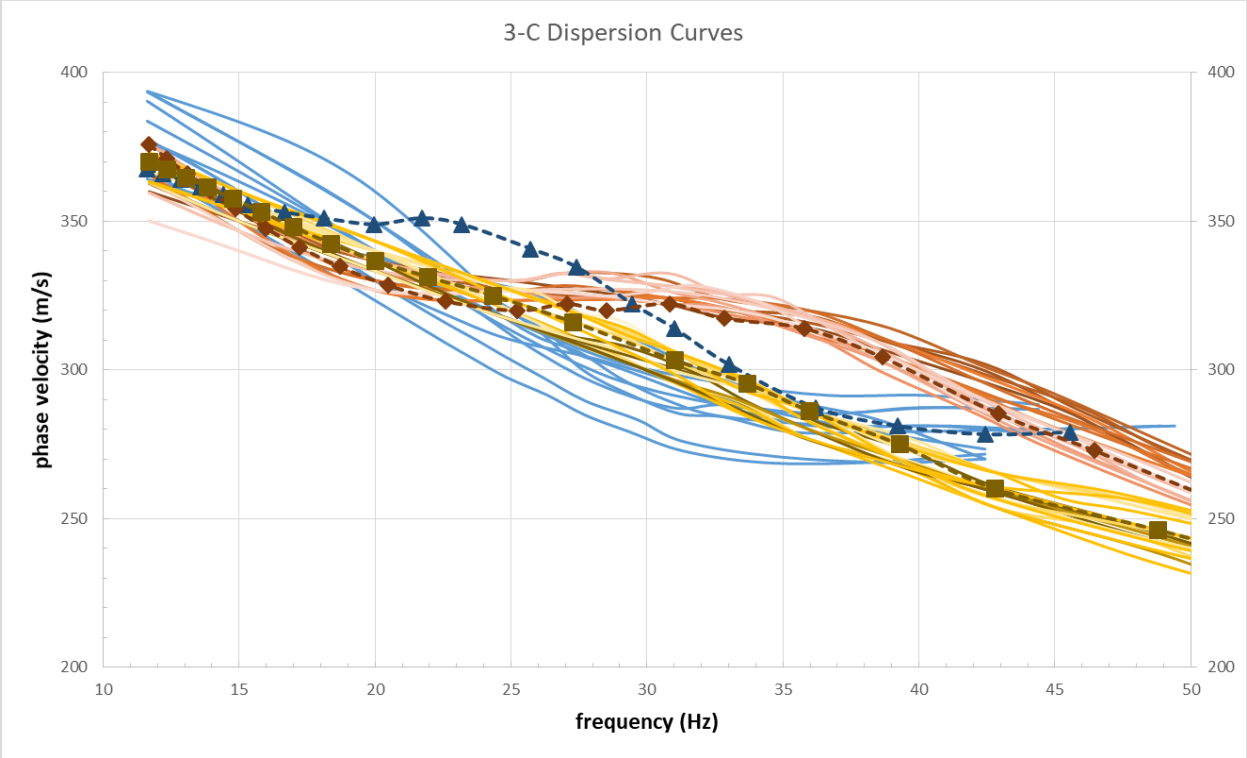

Figure 46. All dispersion curves from the vertical (blue triangle), H1 (orange diamond), and H2 (yellow square) data sets using the 20 m optimal spread size. The dashed-line dispersion curve represents the station 1036, which corresponds to the tunnel location.

Chapter 7: Conclusions

This investigation extensively evaluated the interaction of the active surface-wave wavefield with a test tunnel using conventional and unconventional seismic approaches. A distinctive perturbation in the seismic wavefield was observed on the multiplied H1-H2 BASW sections within the vicinity of the tunnel. Broader disturbances were evident on the vertical and H2 MASW Vs sections, but the MASW sections alone could not be used to isolate the tunnel location without a priori information. BASW sections from all three data sets also revealed a wavefield disturbance outside the tunnel wall that was enhanced significantly by combining the V-H1 and H1-H2 BASW sections. All other scatters were reduced in this combined BASW section and only the backscatter off the tunnel remained. This novel, multi-component backscatter analysis proved to be a valuable tool in this geologic setting where local heterogeneities such as boulders can cause surface-wave scatters. Although the backscatter signature was significantly enhanced by combining multiple sections, the frequency content of the backscatter signatures also multiplies and effectively causes an incorrect depth-to-scattering feature estimation. Therefore, this approach should only be used for signal enhancement purposes, and not depth estimation. Nonetheless, this approach greatly reduced the level of uncertainty associated with identifying the accurate location of the tunnel using surface waves. Tunnel signatures observed on the two MASW Vs sections and BASW sections were verified by similar anomalies observed with numerical modeling.

While backscattered surface waves have been used more commonly and reliably for void detection than MASW, the vertical and H2 MASW Vs section exhibited a tunnel signature that has not been observed before with conventional dispersion-curve analysis in this geologic

setting. These signatures, which may have otherwise been attributed to heterogeneity, were verified by the backscatter analyses. Individual horizontal BASW sections and more notably the multiplied H1-H2 BASW section demonstrated an accurate tunnel signature with high confidence. Surface-wave results presented exemplify the effectiveness of the H1 and H2 components for detecting tunnels that have a small (e.g., 1-2 m) cross-sectional area and emphasize that future investigations should consider using the horizontal components of surface waves both individually and in a combined analysis to attenuate undesired signals and enhance the dominant backscatter signature.

References

Aki, K. and P. G. Richards, 1980, Qualitative Seismology: theory and methods. San Francisco: W. H. Freeman.

Al-Shayea, N., R. Woods, and P. Gilmore, 1994, SASW & GPR to detect buried objects: Symposium on the Application of Geophysics to Engineering and Environmental Problems, EEGS, Expanded Abstracts, 543-560. https://doi.org/10.4133/1.2922086.

Almuhaidib, A. M., and M. N. Toksöz, 2014, Numerical modeling of elastic-wave scattering by near-surface heterogeneities: Geophysics, **79**, no. 4, T199–T217, doi: 10.1190/GEO2013-0208.1.

Anderson, D. L., and C. B. Archameau, 1964, The anelasticity of the Earth: Journal of Geophysical Research, **69**, no. 10, 2071-2084.

Anderson, D. L., A. Ben-Menahem, and C. B. Archameau, 1965, Attenuation of seismic energy in the upper mantle: Journal of Geophysical Research, **70**, no. 6, 1441-1448.

Belesky, R. M., and H. R. Hardy Jr., 1986, Seismic and microseismic methods for cavity detection and stability monitoring of near-surface voids: 27th U.S. Symposium on Rock Mechanics, ARMA, 248-258.

Belfer, I., I. Bruner, S. Keydar, A. Kravtsov, and E. Landa, 1998, Detection of shallow objects using refracted and diffracted seismic waves: Journal of Applied Geophysics, **38**, 155-168.

Bergamo, P., L. Bodet, L. V. Socco, R. Mourgues, and V. Tournat, 2014, Physical modelling of a surface-wave survey over a laterally varying granular medium with property contrasts and velocity gradients: Geophysical Journal International, **197**, no. 1, 233-247. doi: 10.1093/gji/ggt521.

Bergamo, P., and L. V. Socco, 2014, Detection of sharp lateral discontinuities through the analysis of surface-wave propagation: GEOPHYSICS, **79**, no. 4, EN77-EN90.

Billington, E. D., R. J. Palm, and A. T. Grosser, 2006, MASW imaging of an abandoned Minnesota mine: Symposium on the Application of Geophysics to Engineering and Environmental Problems, EEGS, Expanded Abstracts, 482-491.

Boaga, J., G. Cassiani, C. Strobbia, and G. Vignoli, 2013, Mode misidentification in Rayleigh waves: Ellipticity as a cause and a cure: GEOPHYSICS, **78**, no. 4, EN17-EN28.

Boettcher, S. S., S. Mosher, and R. M. Tosdal, 2002, Structural and tectonic evolution of Mesozoic basement-involved fold nappes and thrust faults in the Dome Rock Mountains, Arizona: SPECIAL PAPERS-GEOLOGICAL SOCIETY OF AMERICA, 73-98.

Boiero, D. and L. V. Socco, 2011, The meaning of surface wave dispersion curves in weakly laterally varying structures: Near Surface Geophysics, **9**, no. 6, 561-570. https://doi.org/10.3997/1873-0604.2011042

Buckley, S. F. and J. W. Lane, 2012, Near-surface void detection using a seismic landstreamer and horizontal velocity and attenuation tomography: Symposium on the Application of Geophysics to Engineering and Environmental Problems, EEGS, Expanded Abstracts. https://doi.org/10.4133/1.4721875

Campman, X. H., K. van Wijk, J. A. Scales, and G. C. Herman, 2003, Measuring, imaging and suppressing scattered surface waves. 73rd International Annual Meeting, SEG, Expanded Abstracts, 1897-1900. https://doi.org/10.1190/1.1817689.

Chen, D. H., and T. Scullion, 2008, Detecting subsurface voids using ground-coupled penetrating radar: Geotechnical Testing Journal, **31**, no. 3, 1-8.

Constantopoulos, I. V., 1980, Seismic analysis of buried tunnels: Earthquake Engineering, 7th World Conference, 8, 194-200.

Constantopoulos, I. V., J. T. Motherwell, and J. R. Hall, 1979, Dynamic analysis of tunnels: Numerical Methods in Geomechanics, **3**, 841-848.

Dal Moro, G., and F. Ferigo, 2011, Joint analysis of Rayleigh- and Love-wave dispersion: Issues, criteria and improvements: Journal of Applied Geophysics, **75**, no. 3, 573-589. doi: 10.1016/j.jappgeo.2011.09.008.

de Lucena, R. F. and F. Taioli, 2014, Rayleigh wave modeling: A study of dispersion curve sensitivity and methodology for calculating an initial model to be included in an inversion algorithm: Journal of Applied Geophysics, **108**, 140-151. https://doi.org/10.1016/j.jappgeo.2014.07.007

Eslick, R., G. Tsoflias, D. Steeples, 2008, Field investigation of Love waves in near-surface seismology: GEOPHYSICS, **73**, no. 3, G1-G6. https://doi.org/10.1190/1.2901215

Feigenbaum, D. Z., J. Ivanov, R. D. Miller, S. L. Peterie, and S. L. C. Morton, 2016, Near-surface Qs estimations using multi-channel analysis of surface waves (MASW) and the effect of non-fundamental mode energy on Q-estimation: An example from Yuma Proving Ground, Arizona. 86th International Annual Meeting, SEG, Expanded Abstracts, 4971-4976.

Ferguson, C. A., S. J. Skotnicki, and J. E. Spencer, 1994, Bedrock geology of the eastern and central Tank Mountains, Yuma County, Arizona. Arizona Geological Survey.

Foti, S., F. Hollender, F. Garofalo, D. Albarello, M. Asten, P.-Y. Bard, C. Comina, C. Cornou, B. Cox, G. Di Giulio, T. Forbriger, K. Hayashi, E. Lunedei, A. Martin, D. Mercerat, M. Ohrnberger, V. Poggi, F. Renalier, D. Sicilia, and V. Socco, 2017, Guidelines for the

good practice of surface wave analysis: a product of the InterPACIFIC project: Bulletin of Earthquake Engineering, **16**, 2367–2420. https://doi.org/10.1007/s10518-017-0206-7

Gardner, G. H. F., L. W. Gardner, and A. R. Gregory, 1974, Formation velocity and density - the diagnostic basics for stratigraphic traps: GEOPHYSICS, **39**, no. 6, 770-780.

Gelis, C., D. Leproux, J. Virieux, A. Bitri, S. Operto, and G. Grandjean, 2005, Numerical modeling of surface waves over shallow cavities: Journal and Environmental and Engineering Geophysics, **10**, no. 2, 111-121.

Grandjean, G., and D. Leparoux, 2004, The potential of seismic methods for detecting cavities and buried objects: experimentation at a test site: Journal of Applied Geophysics, **56**, no. 2, 93-106. doi: 10.1016/j.jappgeo.2004.04.004.

Greenfield, R. J., P. M. Lavin, and R. R. Parizek, 1976, Geophysical Methods for Location of Voids and Caves: 121st International Association of Hydrological Sciences Proceedings of the Anaheim Symposium, 465-484.

Häusler, M., C. Schmelzbach, and D. Sollberger, 2018, The Galperin source: A novel efficient multicomponent seismic source: GEOPHYSICS, **83**, no. 6, 19-27. https://library.seg.org/doi/10.1190/geo2018-0020.1

Herman, G. C., P. A. Milligan, R. J. Huggins, and J. W. Rector, 2000, Imaging shallow objects and heterogeneities with scattered guided waves: GEOPHYSICS, **65**, no. 1, 247-252.

Heisey, J. S., K. H. Stokoe II, W. R. Hudson, and A. H. Meyer, 1982, Determination of in situ shear-wave velocity from spectral analysis of surface waves: Research report No. 256-2, Center for Transportation Research, The University of Texas at Austin, December, 277 p.

Ikeda, T., T. Matsuoka, T. Tsuji, and T. Nakayama, 2015, Characteristics of the horizontal component of Rayleigh waves in multimode analysis of surface waves: GEOPHYSICS, **80**, no. 1, EN1-EN11.

Inazaki, T., S. Kawamura, O. Tazawa, Y. Tamanaka, and N. Kano, 2005, Near-surface cavity detection by high-resolution seismic reflection methods using short-spacing type land streamer: Symposium on the Application of Geophysics to Engineering and Environmental Problems, EEGS, Expanded Abstracts, 959-970. https://doi.org/10.4133/1.2923554

Ivanov, J., B. Leitner, W. Shefchik, J. T. Schwenk, and S. Peterie, 2013, Evaluating hazards at salt cavern sites using multichannel analysis of surface waves: The Leading Edge, **32**, no. 3, 298-305.

Ivanov, J., R. D. Miller, D. Z. Feigenbaum, and S. L. Peterie, 2017, Detecting subsurface objects and identifying voids possibilities using the backscatter analysis of surface waves (MASW) method: 4th International Conference on Engineering Geophysics, Expanded Abstracts, 116-119.

Ivanov, J., R. D. Miller, C. B. Park, and N. Ryden, 2003, Seismic search for underground anomalies: 73rd Annual International Meeting, SEG, Expanded Abstracts, 1223-1226. https://doi.org/10.1190/1.1817502.

Ivanov, J., R. D. Miller, and S. L. Peterie, 2016, Detecting and delineating voids and mines using surface wave methods in Galena, KS. 86th International Annual Meeting, SEG, Expanded Abstracts, 2344-2350.

Ivanov, J., R. Miller, and G. Tsoflias, 2008, Some practical aspects of MASW analysis and processing: Symposium on the Application of Geophysics to Engineering and Environmental Problems, EEGS, Expanded Abstracts, 1186-1198.

Ivanov, J., J. Xia, and R. D. Miller, 2006, Optimizing horizontal-resolution improvement of the MASW method: Symposium on the Application of Geophysics to Engineering and Environmental Problems, EEGS, Expanded Abstracts, 1128-1134.

Johnston, D. H., and M. N. Toksoz, 1981, Definitions and terminology, *in* M. N. Toksoz and D. H. Johnston, eds., Seismic Wave Attenuation: Society of Exploration Geophysicists. 1-5.

Kudo, K., and E. Shima, 1970, Attenuation of shear wave in soil: Bulletin of the Earthquake Research Institute, **48**, 145-158.

Lay, T. and T. C. Wallace, 1995, Modern Global Seismology: Academic Press Inc.

Lellouch, A., and M. Reshef, 2017, Shallow diffraction imaging in an SH-wave crosshole configuration: GEOPHYSICS, **82**, no. 1., S9-S18. https://doi.org/10.1190/geo2016-0154.1

Livers, A. J. 2016, Parallel-line beamsteering for anomaly detection: M.S. thesis, University of Kansas.

Livers, A. J., S. L. Peterie, J. Ivanov, and R. D. Miller, 2015, Feasibility of parallel line beamsteering for enhancing tunnel detection: 75th International Annual Meeting, SEG, Expanded Abstracts, 2292-2297.

Llopis, J. L., J. B. Dunbar, L. D. Wakeley, M. K. Corcoran, and D. K. Butler, 2005, Tunnel detection along the Southwest U.S. Border: Symposium on the Application of Geophysics to Engineering and Environmental Problems, EEGS, Expanded Abstracts, 430-443.

Luke, B., and C. Calderon-Macias, 2008, Scattering of surface waves due to shallow heterogeneities: 72nd International Annual Meeting, SEG, Expanded Abstracts, 1283-1287.

Maraschini, M., F. Ernst, S. Foti, and L. V. Socco, 2010, A new misfit function for multimodal inversion of surface waves: GEOPHYSICS, **75**, no. 4, G31-G43. https://doi.org/10.1190/1.3436539

McDonald, E. V., G. K. Dalldorf, and S. N. Bacon, 2009, Landforms and surface cover of U. S. Army Yuma Proving Ground, U.S., Army, YPG Environmental Report. Reno, NV: Desert Research Institute, Division of Earth and Ecosystems Sciences.

Mi, B., J. Xia, C. Shen, L. Wang, and F. Cheng, 2017, Horizontal resolution of multichannel analysis of surface waves: Geophysics, **82**, no. 3, EN51-EN66.

Miller, R. D., K. Park, J. Ivanov, C. Park, D. Laflen, and R. Ballard, 2003, A 2-C towed geophone spread for variable surface conditions: 16th EEGS Symposium on the Application of Geophysics to Engineering and Environmental Problems, Expanded Abstracts. https://doi.org/10.3997/2214-4609-pdb.190.seis06

Miller, R. D., J. Xia, C. Park, and J. Ivanov, 1999, Multichannel analysis of surface waves to map bedrock: The Leading Edge, **18**, no. 12, 1392-1396.

Miller, R. D., O. M. Metheny, J. M. Anderson, and A. R. Wedel, 2010, Study of unconsolidated sediments at Joint Tunnel Test Range (JTTR) on Yuma Proving Grounds, Arizona: The University of Kansas.

Millet, J. A., and H. F. Barnett, 1970, Surface materials and terrain features of Yuma Proving Ground (Laguna, Ariz-Calif, Quadrangle). Technical Report 71-14-ES, 60.

Moran, M. L., and R. J. Greenfield, 1993, Radar signature of a 2.5-D tunnel: GEOPHYSICS, **58**, 1573-1587.

Morton, S. L. C. 2014, Comparison of geophysically-derived and surficial sediment-based estimates of seismic risk in Hartford County, Connecticut: M.S. thesis, University of Connecticut.

Morton, S. L. C., J. Ivanov, and R. D. Miller, 2015, A modified *f-k* filter for removing the effects of higher-mode dispersion patterns from surface wave data: Symposium on the Application of Geophysics to Engineering and Environmental Problems, EEGS, Expanded Abstracts, 445-451.

Morton, S. L., R. D. Miller, J. Ivanov, S. L. Peterie, and R. L. Parsons, 2020, Time-lapse monitoring of stress-field variations within the Lower Permian shales in Kansas: The Leading Edge, **39**, no. 5,318-323. doi: 10.1190/tle39050318.1.

Morton, S. L. C., S. L. Peterie, J. Ivanov, R. D. Miller, D. Z. Feigenbaum, S. D. Sloan, M. L. Moran, and H. H. Cudney, 2016, Feasibility study using surface wave attenuation and seismic quality factor for tunnel detection at the Yuma Proving Ground, AZ: 86th International Annual Meeting, SEG, Expanded Abstracts, 2351-2356.

Morton, S. L. C., S. L. Peterie, J. Ivanov, R. D. Miller, and S. D. Sloan, 2017, Joint interpretation of multi-component surface wave data for tunnel detection: 87th International Annual Meeting, SEG, Expanded Abstracts, 5458-5464.

Nasseri-Moghaddam, A., G. Cascante, and J. Hutchinson, 2005, A new qualitative procedure to determine the location and embedment depth of a void using surface waves: Journal and Environmental and Engineering Geophysics, **10**, no. 1, 51-64.

Nasseri-Moghaddam, A., G. Cascante, C. Phillips, and D. J. Hutchinson, 2007, Effects of underground cavities on Rayleigh waves—Field and numerical experiments: Soil Dynamics and Earthquake Engineering, **27**, no. 4, 300-313. doi: 10.1016/j.soildyn.2006.09.002.

Navarro, C., 1992, Seismic analysis of underground structures: Earthquake Engineering, 10th World Conference, 1939-1944.

O'Neill, A., and T. Matsuoka, 2005, Dominant higher surface-wave modes and possible inversion pitfalls: Journal and Environmental and Engineering Geophysics, **10**, no. 2, 185-201.

Park, C. B., R. D. Miller, and J. Xia, 2001, Offset and resolution of dispersion curve in multichannel analysis of surface waves (MASW): Symposium on the Application of Geophysics to Engineering and Environmental Problem, EEGS, Expanded Abstracts. https://doi.org/10.4133/1.2922953

Park, C. B., R. D. Miller, and J. Ivanov, 2002, Filtering surface waves: Symposium on the Application of Geophysics to Engineering and Environmental Problem, EEGS, Expanded Abstracts, SEI9-SEI9.

Park, C. B., R. D. Miller, and J. Xia, 1998, Imaging dispersion curves of surface waves on multi-channel record: 68th International Annual Meeting, SEG, Expanded Abstracts, 1377-1380. https://doi.org/10.1190/1.1820161.

Pei, D. 2007. Modeling and inversion of dispersion curves of surface waves in shallow site investigations: Ph.D. Dissertation, University of Nevada, Reno.

Peterie, S. L., and R. D. Miller, 2015, Near-surface scattering phenomena and implications for tunnel detection: Interpretation, **3**, no. 1, SF43-SF54. doi: 10.1190/int-2014-0088.1.

Peterie, S. L., R. D. Miller, J. Ivanov, and S. D. Sloan, 2020, Shallow tunnel detection using SH-wave diffraction imaging: GEOPHYSICS, **85**, no. 2, EN29-EN37.

Phillips, C., G. Cascante, and J. Hutchinson, 2000, Detection of Underground Voids with Surface Waves: Symposium on the Application of Geophysics to Engineering and Environmental Problems, EEGS, Expanded Abstracts, 29-37.

Putnam, N. H., A. Nasseri-Moghaddam, O. Kovin, and N. L. Anderson, 2008, preliminary analysis using surface waves methods to detect shallow manmade tunnels: Symposium on the Application of Geophysics to Engineering and Environmental Problems, EEGS, Expanded Abstracts, 679-688.

Rickards, B. T. 2011, Near-surface shear-wave velocity measurements in unlithified sediment: M.S. thesis, University of Kansas.

Rickards, B. T., D. W. Steeples, R. D. Miller, J. Ivanov, S. Peterie, S. D. Sloan, and J. McKenna, 2011, Near-surface shear-wave velocity measurements in unlithified sediment: 81st Annual International Meeting, SEG, Expanded Abstracts, 1416-1420.

Riyanti, C. D., X. H. Campman, and G. C. Herman, 2005, Inversion of Scattered Surface Waves for Characterizing Shallow Heterogeneities: 75th International Annual Meeting, SEG, Expanded Abstracts, 1053-1056.

Sastry, R. G., 2014, Geoelectric imaging scores over MASW in geotechnical site characterization: Symposium on the Application of Geophysics to Engineering and Environmental Problems, EEGS, Expanded Abstracts, 521-531.

Schwab, F., and L. Knopoff, 1972, Fast surface wave and free mode computations, *in* Bolt, B. A., Ed., Methods in in Computational Physics: Academic Press, 87-180.

Schwenk, J. T., 2013, Constrained parameterization of the multichannel analysis of surface waves approach with application at Yuma Proving Ground, Arizona: M.S. thesis, University of Kansas.

Schwenk, J. T., S. D. Sloan, J. Ivanov, and R. D. Miller, 2016, Surface-wave methods for anomaly detection: GEOPHYSICS, **81**, no. 4, EN29-EN42.

Schwenk, J. T., S. D. Sloan, R. D. Miller, and J. Ivanov, 2014, Correlation of the backscatter analysis of surface waves method (BASW) for anomaly detection: 84th International Annual Meeting, SEG, Expanded Abstracts, 2029-2035. doi: 10.1190/segam2014-1684.1.

Shao, G.-z., G. P. Tsoflias, and C-j. Li, 2016, Detection of near-surface cavities by generalized S-transform of Rayleigh waves: Journal of Applied Geophysics, **129**, 53-65. https://doi.org/10.1016/j.jappgeo.2016.03.041

Sheriff, R. E., 1988, Geophysical methods: Prentice Hall Inc.

Sherman, C., J. Rector, D. Dreger, and S. Glaser, 2014, Seismic tunnel detection at Black Diamond Mines Regional Preserve: 84th International Annual Meeting, SEG, Expanded Abstracts, 2078-2082.

Sherman, C., J. Rector, D. Dreger, and S. Glaser, 2018, A numerical study of surface-wave-based tunnel detection at the Black Diamond Mines Regional Preserve, California: GEOPHYSICS **83**, no. 4, EN13-EN22. https://doi.org/10.1190/geo2017-0467.1

Sherrod, D. R., and R. M. Tosdal, 1991, Geologic setting and Tertiary structural evolution of southwestern Arizona and southeastern California: Journal of Geophysical Research: Solid Earth (1978-2012), **96**, 12407-12423.

Schustak, M., N Wechsler, A. Yurman, and M. Reshef, 2015, Comparison of surface vs. cross-hole seismic methods for void detection in the shallow sub-surface: 85th International Annual Meeting, SEG, Expanded Abstracts, 2286-2291.

Sloan, S., 2015, A current look at geophysical detection of illicit tunnels: The Leading Edge, **34**, 154-158.

Sloan, S., J. R. McKenna, S. W. Broadfoot, O. M. Metheny, R. D. Miller, S. Peterie, J. Ivanov, and L. D. Wakeley, 2011, active seismic imaging at San Luis, Arizona, in support of tunnel detection: Army Corps of Engineering Engineer Research and Development Center Report.

Sloan, S. D., O. M. Metheny, S. L. Peterie, R. D. Miller, T. L. Snow, and J. R. McKenna, 2013a, In-theater seismic acquisition: operational examples from a tunnel detection team: 83rd International Annual Meeting, SEG, Expanded Abstracts, 1801-1805.

Sloan, S. D., R. D. Miller, J. Ivanov, and S. Walters, 2009, Shear-wave velocity as an indicator of increased stress and failure potential associated with dissolution mining voids: Symposium on the Application of Geophysics to Engineering and Environmental Problem, EEGS, Expanded Abstracts, 363-372.

Sloan, S. D., J. J. Nolan, S. W. Broadfoot, J. R. McKenna, and O. M. Metheny, 2013b, Using near-surface seismic refraction tomography and multichannel analysis of surface waves to detect shallow tunnels: A feasibility study: Journal of Applied Geophysics, **99**, 60-65. doi: 10.1016/j.jappgeo.2013.10.004.

Sloan, S. D., S. L. Peterie, J. Ivanov, R. D. Miller, and J. R. McKenna, 2010, Void detection using near-surface seismic methods, *in* R. D. Miller, J. D. Bradford, and K. Holliger, eds.,

Advances in near-surface seismology and ground-penetrating radar: Society of Exploration Geophysicists, 201-218

Sloan, S. D., S. L. Peterie, R. D. Miller, J. Ivanov, J. R. McKenna, S. W. Broadfoot, and O. M. Metheny, 2012, Tunnel detection using near-surface seismic methods: 82nd International Annual Meeting, SEG, Expanded Abstracts, 1-5. doi: 10.1190/segam2012-1442.1.

Sloan, S. D., S. Peterie, R. D. Miller, J. Ivanov, J. T. Schwenk, and J. McKenna, 2015, Detecting clandestine tunnels using near-surface seismic techniques: GEOPHYSICS, **80**, no. 5, EN127-EN135.

Smith, J. A., D. Borisov, H. Cudney, R. D. Miller, R. Modrak, M. Moran, S. L. Peterie, S. D. Sloan, J. Tromp, and Y. Wang, 2019, Tunnel detection at Yuma Proving Ground, Arizona, USA – Part 2: 3D full-waveform inversion experiment: GEOPHYSICS, **84**, no. 1, B107-B120.

Steeples, D. W., 2001, Engineering and environmental geophysics at the millennium: GEOPHYSICS, **66**, no. 1, 31-35. https://doi.org/10.1190/1.1444910

Socco, L. V., S. Foti, and D. Boiero, 2010, Surface-wave analysis for building near-surface velocity models - Established approaches and new perspectives: GEOPHYSICS, **75**, no. 5, 75A83-75A102.

Socco, L. V., and C. Strobbia, 2003, Extensive modeling to study surface wave resolution: Symposium on the Application of Geophysics to Engineering and Environmental Problem, EEGS, Expanded Abstracts, 1312-1319.

Song, Y.-Y., J. P. Castagna, R. A. Black, and R. W. Knapp, 1989, Sensitivity of near-surface shear-wave velocity determination from Rayleigh and Love waves: 59th International Annual Meeting, SEG, Expanded Abstracts, 509-512.

Song, X., H. Gu, J. Liu, and X. Zhang, 2007, Estimation of shallow subsurface shear-wave velocity by inverting fundamental and higher-mode Rayleigh waves: Soil Dynamics and Earthquake Engineering, **27**, no. 7, 599-607.

Steeples, D. W. 2001, Engineering and environmental geophysics at the millennium: GEOPHYSICS, **66**, 31-35.

Suarez, G. M. and R. R. Stewart, 2008, A field comparison of 3-C land streamer versus planted geophone data: 78th International Annual Meeting, SEG, Expanded Abstracts, 16-21. https://doi.org/10.1190/1.3054781

Tosdal, R. M., and D. R. Sherrod, 1985, Geometry of Miocene extensional deformation, lower Colorado River Region, Southeastern California and Southwestern Arizona: Evidence for the presence of a regional low-angle normal fault: The Internet Archive, NASA, online.

Turpening, R. M., 1976, Cavity detection by means of seismic shear and compressional wave refraction techniques: Report 116400-1-F, Environmental Research Institute of Michigan.

Wang, Y., R. D. Miller, S. L. Peterie, S. D. Sloan, M. L. Moran, H. H. Cudney, J. A. Smith, D. Borisov, R. Modrak, and J. Tromp, 2019, Tunnel detection at Yuma Proving Ground, Arizona, USA – Part 1: 2D full-waveform inversion experiment: GEOPHYSICS, **84**, no. 1, B95-B105.

Wright, C., E. J., Walls, and D. de J. Carneiro, 2000, The seismic velocity distribution in the vicinity of a mine tunnel at Thabazimbi, South Africa: Journal of Applied Geophysics, **44**, 369-382.

Xia, J., R. D. Miller, C. Chen, and J. Ivanov, 2004, Increasing horizontal resolution of geophysical models by generalized inversion: 74th Annual International Meeting, SEG, Expanded Abstracts, 1437-1440.

Xia, J., R. D. Miller, and C. Park, 1999, Estimation of near-surface shear-wave velocity by inversion of Rayleigh waves: GEOPHYSICS, **64**, no. 3, 691-700.

Xia, J., R. D. Miller, C. B. Park, J. A. Hunter, and J. B. Harris, 2000, Comparing shear-wave velocity profiles from MASW with borehole measurements in unconsolidated sediments, Fraser River Delta, B.C., Canada: Journal of Environmental and Engineering Geophysics, **5**, no. 3, 1-13.

Xia, J., R. D. Miller, C. B. Park, J. A. Hunter, J. B. Harris, and J. Ivanov, 2002a, Comparing shear-wave velocity profiles from multichannel analysis of surface wave with borehole measurements: Soil Dynamics and Earthquake Engineering, **22**, no. 1, 181-190.

Xia, J., R. D. Miller, C. Park, and G. Tian, 2002b, Determining Q of near-surface materials from Rayleigh waves: Journal of Applied Geophysics, **51**, 121-129.

Xia, J., J. E. Nyquist, Y. Xu, Y., M. J. S. Roth, and R. D. Miller, 2007, Feasibility of detecting near-surface feature with Rayleigh-wave diffraction: Journal of Applied Geophysics, **62**, no. 3, 244-253. doi: 10.1016/j.jappgeo.2006.12.002.

Xia, J., Y. Xu, Y. Luo, R. D. Miller, R. Cakir, and C. Zeng, 2012a, Advantages of using multichannel analysis of Love Waves (MALW) to estimate near-surface shear-wave velocity: Surveys in Geophysics, **33**, no. 5, 841-860. doi: 10.1007/s10712-012-9174-2.

Xia, J., Y. Xu, R. D. Miller, and J. Ivanov, 2012b, Estimation of near-surface quality factors by constrained inversion of Rayleigh-wave attenuation coefficients: Journal of Applied Geophysics, **82**, 137-144. doi: 10.1016/j.jappgeo.2012.03.003.

Xu, Y., J. Xia, and R. D. Miller, 2006, Quantitative estimation of minimum offset for multichannel surface-wave survey with actively exciting source: Journal of Applied Geophysics, **59**, no. 2, 117-125. https://doi.org/10.1016/j.jappgeo.2005.08.002

Yu, H., Y. Yuan, Z. Qiao, Y. Gu, Z. Yang, and X. Li, 2013, Seismic analysis of a long tunnel based on multi-scale method: Engineering Structures, **49**, 572-587. doi: 10.1016/j.engstruct.2012.12.021.

Zeng, C., J. Xia, R. D. Miller, G. P. Tsoflias, 2009, Modeling results on detectability of shallow tunnels using Rayleigh-wave diffraction: 79th International Annual Meeting, SEG, Expanded Abstracts, 1425-1429.

Zeng, C., J. Xia, R. Miller, and G. Tsoflias, 2012, An improved vacuum formulation for 2D finite-difference modeling of Rayleigh waves including surface topography and internal discontinuities: Geophysics, **77**, no. 1, T1-T9.

Zhang, S. X., and L. S. Chan, 2003, Possible effects of misidentified mode number on Rayleigh wave inversion: Journal of Applied Geophysics, **53**, no. 1, 17-29. doi: 10.1016/s0926-9851(03)00014-4.

Zhang, S. X., L. S. Chan, and J. Xia, 2004, The selection of field acquisition parameters for dispersion images from multichannel surface wave data: Pure and Applied Geophysics, **161**, 185-201.